



**SAPIENZA**  
UNIVERSITÀ DI ROMA

**Facoltà di Ingegneria dell'Informazione, Informatica e Statistica**

**Dipartimento di Ingegneria dell'Informazione, Elettronica e  
Telecomunicazioni**

**Thesis for the Ph.D. degree in Remote Sensing**

**XXVIII cycle**

***Advanced signal processing techniques for  
WiFi-based Passive Radar for short-range  
surveillance***

**Tatiana Martelli**

Supervisor

Prof. Fabiola Colone



## INDEX

|                                                                                            |    |
|--------------------------------------------------------------------------------------------|----|
| List of abbreviations and definitions .....                                                | iv |
| 1. Introduction .....                                                                      | 1  |
| 2. Passive Radar based on WiFi transmissions .....                                         | 6  |
| 3. Advanced disturbance cancellation technique for target detection .....                  | 13 |
| 3.1. The ECA and ECA-Batches approaches .....                                              | 13 |
| 3.1.1. Disturbance cancellation capability .....                                           | 13 |
| 3.1.2. Limitations of the ECA-B .....                                                      | 15 |
| 3.2. The ECA-Sliding technique .....                                                       | 21 |
| 3.3. Performance analysis.....                                                             | 24 |
| 4. Enhanced WiFi-based passive ISAR for vehicular targets.....                             | 27 |
| 4.1. Effect of the disturbance cancellation stage on ISAR products.....                    | 27 |
| 4.2. Enhanced ISAR profiling technique.....                                                | 28 |
| 4.2.1. Iterative Target Preserving (ITP) cancellation algorithm .....                      | 28 |
| 4.2.2. Results against synthetic target echoes injected in real stationary background..... | 31 |
| 4.3. Experimental results against moving man-made targets .....                            | 35 |
| 4.3.1. Experimental set-up and acquisition scenario .....                                  | 35 |
| 4.3.2. ITP strategy compared with ECA.....                                                 | 36 |
| 5. Indoor radar surveillance against human targets .....                                   | 41 |
| 5.1. Target detection and localization: experimental results .....                         | 41 |
| 5.2. ISAR techniques for improved cross-range resolution.....                              | 46 |
| 6. Small private airports surveillance .....                                               | 51 |
| 6.1. Ultralight airfields monitoring application .....                                     | 51 |
| 6.2. Acquisition campaign and set-up .....                                                 | 53 |
| 6.3. Results against experimental data .....                                               | 54 |
| 6.3.1. Test against a landing aircraft.....                                                | 55 |
| 6.3.2. Test against small aircrafts maneuvering along the airfield .....                   | 56 |

|                                                                                                             |    |
|-------------------------------------------------------------------------------------------------------------|----|
| 6.3.3. Test against an utility vehicle .....                                                                | 59 |
| 6.3.4. Test against human targets .....                                                                     | 60 |
| 7. WiFi-based passive radar in forward scatter configuration .....                                          | 62 |
| 7.1. Motivations .....                                                                                      | 62 |
| 7.2. Acquisition campaign and data collection.....                                                          | 63 |
| 7.2.1. Analysis of the range compressed data.....                                                           | 65 |
| 7.2.2. Detection performance .....                                                                          | 67 |
| 7.3. Target classification results .....                                                                    | 69 |
| 7.3.1. Signature analysis and possible exploitation .....                                                   | 69 |
| 7.3.2. Results against experimental data .....                                                              | 70 |
| 8. Monostatic vs Forward geometry .....                                                                     | 74 |
| 8.1. Power budget analysis .....                                                                            | 74 |
| 8.2. Detection performance comparison.....                                                                  | 78 |
| 8.2.1. Methodology .....                                                                                    | 78 |
| 8.2.2. RCS enhancement analysis .....                                                                       | 79 |
| 8.2.3. Target detection capability analysis .....                                                           | 85 |
| 8.3. Considerations about the computational load saving and system complexity reduction in FW geometry..... | 86 |
| 8.3.1. Analysis on the region extension of the surveyed area.....                                           | 86 |
| 8.3.2. Analysis on the number of taps of the cancellation stage.....                                        | 88 |
| 9. Conclusions .....                                                                                        | 90 |
| Publications .....                                                                                          | 92 |
| International Journals .....                                                                                | 92 |
| Conference proceedings .....                                                                                | 92 |
| Technical reports .....                                                                                     | 93 |
| References.....                                                                                             | 94 |





## LIST OF ABBREVIATIONS AND DEFINITIONS

| <b>Abbreviation</b> | <b>Definition</b>                               |
|---------------------|-------------------------------------------------|
| WSN                 | Wireless Sensor Networks                        |
| RFID                | Radio Frequency Identification                  |
| UWB                 | Ultra-Wide Bandwidth                            |
| PBR                 | Passive Bistatic Radar                          |
| HF                  | High Frequency                                  |
| UHF                 | Ultra High Frequency                            |
| DAB                 | Digital Radio Broadcasting                      |
| DVB                 | Digital Video Broadcasting                      |
| GSM                 | Global System for Mobile Communications         |
| UMTS                | Universal Mobile Telecommunications System      |
| WiMAX               | Worldwide Interoperability for Microwave Access |
| LTE                 | Long Term Evolution                             |
| ISAR                | Inverse Synthetic Aperture Radar                |
| ECA                 | Extensive Cancellation Algorithm                |
| ECA-B               | ECA-Batch                                       |
| ECA-S               | ECA-Sliding                                     |
| FSR                 | Forward Scatter Radar                           |
| SNR                 | Signal-to-noise ratio                           |
| PFSR                | Passive Forward Scatter Radar                   |
| AP                  | Access Point                                    |
| TX                  | Transmitter                                     |
| AF                  | Ambiguity Function                              |
| DSSS                | Direct Sequence Spread Spectrum                 |
| OFDM                | Orthogonal Frequency-Division Multiplexing      |
| PSR                 | Peak Side Ratio                                 |
| ACF                 | Auto Correlation Function                       |
| CPI                 | Coherent Processing Interval                    |
| LS                  | Least Square                                    |
| 2D-CCF              | Two-dimensional cross-correlation function      |
| CSMA                | Carrier Sense Multiple Access                   |
| CFAR                | Constant False Alarm Rate                       |
| DOA                 | Direction of Arrival                            |

|       |                                         |
|-------|-----------------------------------------|
| CA    | Clutter Attenuation                     |
| PSF   | Point Spread Function                   |
| ITP   | Iterative Target Preserving             |
| RX    | Receiver                                |
| RCS   | Radar Cross-Section                     |
| ATC   | Automatic Target Classification         |
| SISAR | Shadow Inverse Synthetic Aperture Radar |
| FS    | Forward Scatter                         |
| NFS   | Near Forward Scatter                    |

## 1. INTRODUCTION

In recent years, there has been a growing interest in Wireless Sensor Networks (WSN) due to the security and public safety issues, as well as service matters [1]-[4]. Applications such as border surveillance and intrusion detection and classification in both outdoor and indoor environments have constituted a compelling application category for WSN. Real-world applications include, e.g., people location and navigation along building, automotive safety, vehicle navigation and classification, or asset tracking.

Various wireless technologies have been used among which infrared, IEEE 802.11 wireless LAN and ultrasonic. More recently, Radio Frequency Identification (RFID) has become a very attractive solution thanks to a number of desirable features, such as contactless communications, high data rate and security, non line-of-sight readability, compactness and low cost [5]. In particular, a very promising wireless technique for next generation RFID is the Ultra-Wide Bandwidth (UWB) technology because it is able to overcome most of the limitations of current narrow bandwidth RFID technology [6].

Despite the effectiveness of these techniques has been largely demonstrated, they have a major drawback. Basically, with the exception of the infrared, which however requires direct line-of-sight and is a short-range signal transmission, the above mentioned technologies require the target objects to be equipped with a cooperative device (e.g. a wireless LAN system, a RFID tag, etc.). As a consequence they are not suited for specific surveillance applications such as intruder location, detection, tracking and identification of unauthorized vehicles in a forbidden area, and so on.

Therefore, the above mentioned techniques could be nicely complemented by sensors able to operate against non-cooperative targets. To this purpose, a suitable low-cost solution is offered by the passive radar concept. Passive Bistatic Radar (PBR) exploits existing illuminators of opportunity to perform target detection and localization thus embracing the current trend of using standard, low-cost, and already deployed technologies.

Numerous transmitters for telecommunications, radio navigation, and remote sensing applications have been exploited as sources of opportunity [7]-[9]. Broadcast transmitters represent some of the most attractive choices for long range surveillance applications, owing to their excellent coverage. In particular, the most common signals for PBR in use today are non-cooperative FM commercial radio stations since they are especially attractive for the generally high level of transmitted power, for the wide coverage, and for the limited cost of the required receivers, [10]-[12]. A number of studies have looked at the use of different analogue signals such as High Frequency (HF) radio and Ultra High Frequency (UHF) television broadcasts, [13]-[16], as well as digital transmissions such as Digital Radio Broadcasting (DAB) and Digital Video Broadcasting (DVB), [17]-[20]. In particular, DAB and DVB represents a very attractive choice since they allow a reasonable coverage and are characterized by wider bandwidth (and thus better resolution) than FM radio signals [21]. Transmitters for mobile personal communication and network connection provide a largely populated and well-connected network of sources of opportunity for medium range PBR surveillance. These include the base stations of Global System for Mobile Communications (GSM), Universal Mobile Telecommunications System (UMTS), Worldwide Interoperability for Microwave Access (WiMAX), and forthcoming generation, such as Long Term Evolution (LTE), [22]-[30]. Moreover, Global Navigation Satellite System (like GPS, GLONASS, and the forthcoming Galileo) transmitters, in MEO orbits, provide signals with well controlled quality, constant level, and guarantee that at least four space-based sources of opportunity are visible in each position of the Earth at any time [31]-[32].

However, aiming at indoor surveillance or at monitoring small external areas, the IEEE 802.11 standards-based (WiFi) technology has been considered as potential source of opportunity since it offers reasonable bandwidth (range resolution), coverage and wide accessibility [33]-[34]. The possibility to exploit such a ubiquitous and easily accessible source has been shown by the research group of University of Rome “La Sapienza” to be an appropriate choice for the detection and localization of designated vehicles, human beings or man-made objects within short ranges using the passive radar principle [35]-[37]. Moreover, the possibility to obtain a high-resolution cross-range profile of vehicular targets by applying Inverse Synthetic Aperture Radar (ISAR) has been reported in [38]. In addition, other research groups investigated the feasibility of uncooperatively and covertly detecting people moving behind walls, [39]-[40].

Among the very nice features of the PBR approach is that no extra signal is transmitted; this limits the energy consumption, prevents possible interferences with pre-existing systems, and makes the sensor free from any issue related to human health. Moreover, this technique removes the requirements for cooperative targets and it is not subject to the blind spots and potentially intrusive equipment necessary for video surveillance. Therefore, it could be used in public areas (such as parking area, railways, airports) or private commercial premises such as office buildings or warehouses and malls.

The main drawback of PBR is that the transmitted waveform is not within the control of the radar designer. As a consequence, the target echoes may be masked by the disturbance contribution (i.e. direct signal and multipath): this can occur even in the presence of a large range-Doppler separation because of the high sidelobes level of the signal ambiguity function. To counteract these effects, proper processing techniques have been designed to enable effective target detection, localization and imaging [35]-[38], [41]-[43].

However the WiFi-based processing scheme in [35]-[38] has some specific problems that have to be faced. Therefore, in the first part of this work, alternative processing techniques to enhance the performances of the existing WiFi PBR system have been developed.

- A significant effort has been devoted at the disturbance cancellation that represents one of the key stage within a conventional PBR processing scheme because strong disturbance returns (such as the direct signal from the transmitter and multipath) might completely mask the target making it undetectable. First of all, in this work it is shown that the disturbance cancellation technique, known as Extensive cancellation Algorithm batch version (ECA-B) [44], might yields some limitations when employed against highly time disturbance scenarios in the presence of slowly moving targets (namely targets observed at low Doppler frequency). Obviously, in a WiFi-based PBR employed for short range application, it is quite typical to deal with this type of targets. It is shown that the ECA-B yields undesired effects on the target echo at the output of the cancellation stage; such effects are the responsible for the emergence of unwanted structures in the Doppler dimension that can be responsible of useful dynamic range reduction or masking effect over weak targets, thus limiting the detection capability. Aiming at counteracting these limitations, an enhanced version of the ECA-B has been developed. The proposed ECA-Sliding technique (ECA-S) can reach improved cancellation capability as verified with reference to live data set.
- In addition, in [38] it has been proved that the disturbance cancellation stage is a mandatory step not only for target detection but also for the ISAR profiling; nevertheless the background removal can have a non negligible effect on the target signal in input to the ISAR processing thus it might reduce the quality of the ISAR products. Obviously, when dealing with man-made targets (such as vehicles), enhanced quality products are essential to enable the automatic classification of designed targets. Although the cancellation technique has been optimized in this work as above mentioned, however all

ECA versions distort the target spectrum at very low Doppler frequency by inserting a cancellation notch. As a consequence, the processing techniques described in [38] might yield limited performance especially when accurate profiling is required. Therefore in this work, an enhanced ISAR profiling technique is proposed. In particular, an alternative cancellation approach is introduced to obtain an effective removal of such disturbance while preserving the target contribution and, consequently, the quality of the ISAR processing. Based on an iterative target preserving algorithm, the proposed processing strategy is shown to overcome the limitations of the other cancellation approaches. The effectiveness of the proposed technique has been preliminary verified against data sets obtained by injecting synthetic target returns into the real background; then it has been tested against real vehicular targets moving in a parking area. The reported results prove that reliable and stable profiles of moving man-made objects are obtained which might be fruitfully exploited by a classification scheme based on an appropriate signatures database.

The second main goal of this work is to extend the range of possible applications of the WiFi PBR system with new and advanced potentialities. Specifically, some of these opportunities have been investigated within the the EU project SOS (Sensors system for detection and tracking Of dangerous materials in order to increase the airport Security in the indoor landside area) where the WiFi-based PBR sensor is jointly employed with other active and passive radar sensors to enhance the security level in the airport terminal area, [45].

- In particular, the effectiveness of the proposed system has been mostly demonstrated in outdoor scenarios while few results are available for indoor localization. Therefore, in this work the surveillance capability of WiFi-based PBR in indoor environment has been demonstrated. To this purpose, the above techniques are tailored to face the specific challenges of the considered application and validated using real datasets. An experimental setup developed at the University of Rome “La Sapienza” is employed in order to perform different acquisitions against human targets. The reported results prove the actual possibility to detect and accurately track persons moving in realistic indoor environment. However, there are some limitation when moving people move very close each other. Obviously, this is due to the limited resolution offered by the WiFi PBR sensor (WiFi transmissions allow a range resolution typically limited to tenths meters, due to the limited frequency bandwidth occupied by the available signal). For these reasons, the possibility to apply ISAR techniques to improve the cross-range resolution has been investigated. The reported results clearly shows that, by extending the coherent processing interval up to a few seconds allows to effectively discriminate closely spaced targets moving in a hall, whereas they could not be resolved by a conventional processing. This could be an invaluable characteristic in indoor scenarios as it would yield an improved resolving capability to be exploited against the typically high concentration of targets moving in the surveyed scene.
- So far, the effectiveness of the conceived sensor has been typically shown in very specific case studies with the sole aim to provide a proof of concept. In this work, the potential exploitation of WiFi-based PBR systems is investigated with reference to a real-world civil application. In particular, the monitoring application of small private airstrips or airfields has been considered. This terminology refers to open areas designated for the taking-off and landing of small aircrafts, but which, unlike an airport, have generally short and possibly unpaved runways (e.g. grass, dirt, sand, or gravel surfaces) and do not necessarily have terminals. More important, such areas usually are devoid of conventional technologies, equipment, or procedures adopted to guarantee safety and security in large aerodromes. In such scenarios, it would be of great potential interest the possibility to employ low-cost, compact, non-intrusive, and non-transmitting sensors as a way to improve safety and security with limited impact on the airstrips users. To this purpose WiFi-based passive radar sensors appear as good candidates. The study has been conducted against the data sets collected during a dedicated

experimental campaign that has been performed in a small private airfield for light/ultralight airplanes. Both aircrafts, cars, and people have been employed as targets of opportunity to simulate different operative conditions of interest. The results obtained with the conceived sensor support the practical applicability of the WiFi-based passive radar concept for improving safety and security of small private airfields and demonstrate its suitability to be usefully employed in such scenarios in the near future.

- Finally, the feasibility of non-conventional geometries using WiFi transmissions has been investigated. In particular, the Forward scatter radar (FSR) configuration has been considered. As it is well known, FSR is an extreme bistatic radar configuration where the bistatic angle is near to  $180^\circ$  and according to the literature, it offers a number of promising features compared to traditional monostatic radar such as enhanced target radar cross-section, robustness to stealth technology, simple hardware and automatic target classification, [46]-[48]. Numerous works prove the effectiveness of a FSR using active systems, [49]-[57]. The transfer of the FSR concept to passive system provides a new emerging area of research. In fact, recently, there has been a growing attention in the use of FSR configuration in passive radar [58]. In particular, in [59]-[63] has been demonstrated the feasibility of such geometry using GSM, GNSS and DVB-T signals as illuminators of opportunity. In this work, aiming at short range surveillance of ground targets, the feasibility and the impact of the forward scatter geometry on WiFi-based PBR have been investigated for the first time.

To this purpose, a dedicate acquisition campaign has been performed in a wide parking area using different cars model as cooperative targets. First, the potentiality to exploit a passive forward scatter radar (PFSR) based on WiFi transmissions for vehicle classification has been investigated. In particular, a procedure to extract the vehicle signatures from the received signal is presented. The preliminary results obtained by means of an experimental setup developed and fielded at University of Rome “La Sapienza” show that different targets yield quite different signature shapes that can be fruitfully exploited by a classification stage according to a reasonable strategy. Then, the forward and the monostatic configurations are compared in terms of target detection capability. The results proves that the forward geometry yields effectively an enhancement in target SNR that allows a gain in target detection compared with the monostatic geometry.

Concluding, the results shown in this work support the practical applicability of the WiFi-based passive radar concept for improving internal and external security of private/public areas and premises and demonstrate its suitability to be usefully employed in an integrated multi-sensor surveillance.

This work is organized as follow. In Section 2, the WiFi-based PBR developed so far by the research group of University of Rome “La Sapienza” is briefly recalled together with the main processing stages. In the Section 3, the limitations of ECA-B are investigated by means of theoretical derivations and experimental results; moreover, the ECA-S approach is presented and its effectiveness is demonstrated against real data set compared to previous ECA versions. Section 4 introduces the innovative cancellation approach able to preserve the quality of the ISAR products and its effectiveness is analysed against synthetic targets echoes injected in real stationary background and against real vehicular targets. The results in terms of detection and localization against people walking in a hall are shown in Section 5; in addition, the ISAR processing results to improve the cross range resolution are reported. The potential exploitation of a WiFi-based PBR system in the monitoring application of small private airfields for light/ultralight airplanes is investigated in Section 6. Section 7 briefly describe the forward scatter radar concept and reports the experimental setup used to perform the tests and the acquisition campaign. In addition, it investigates the possibility to employ a passive radar in forward scatter configuration for vehicle classification and first experimental results are reported. Then, in Section 8, monostatic and

forward receiver are compared in target detection capability. Finally, in the Section 9 we draw our conclusions.



## 2. PASSIVE RADAR BASED ON WIFI TRANSMISSIONS

Despite their complexity and the wide variety of adopted standards, WiFi transmissions can be nicely exploited for PBR purposes. In particular, a WiFi Access Point (AP), used to provide coverage for an assigned area, potentially acts as an ideal illuminator of opportunity for short-range PBR surveillance if appropriate techniques are adopted to process the collected signals.

The basic WiFi-based PBR processing scheme for target detection designed by the research group of University of Rome “La Sapienza” has been fully described in [35]. Possible approaches to target localization have been investigated in [36] using different sets of measures whereas in [38] has been defined the required steps for obtaining a cross-range profile of the observed targets via the application of ISAR techniques. The resulting overall WiFi-based PBR processing scheme is shown in Figure 1 and its main blocks are briefly summarized in the following.

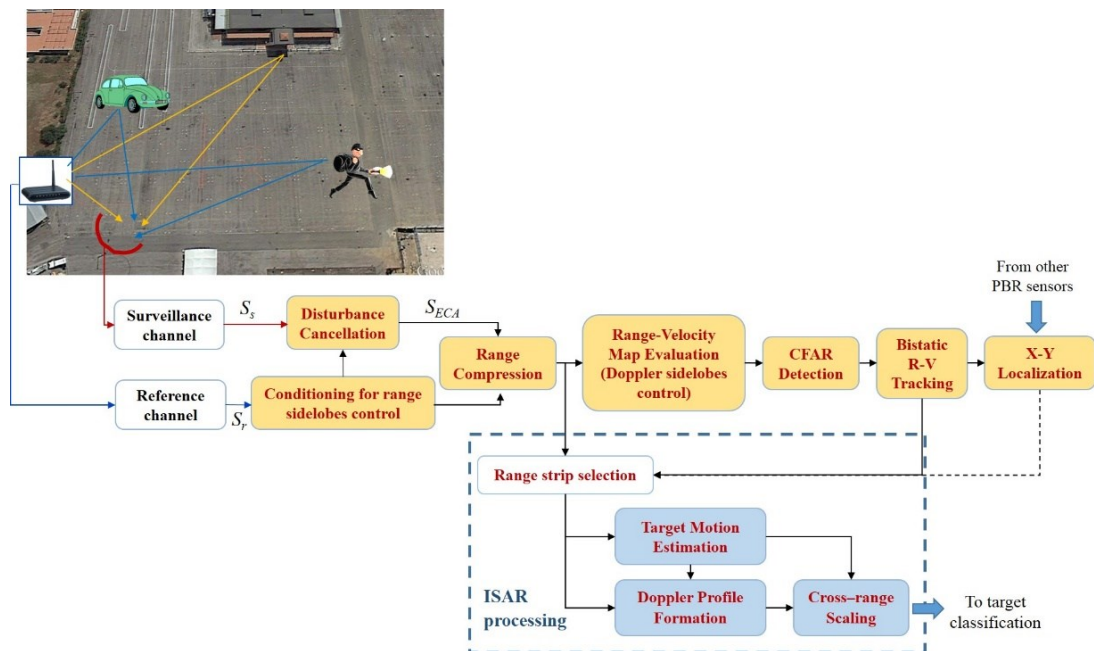


Figure 1. WiFi-based PBR processing scheme.

*Receiving channels.* The low power signal reflected from the target is collected by the main PBR receiver (typically known as the surveillance channel) using a directive antenna steered toward the surveillance area. An auxiliary receiver (typically known as the reference channel) is usually adopted to collect the transmitted signal that is not known at the receiver. To this purpose an additional directive antenna steered toward the transmitter might be exploited. Alternatively, for the considered local area application, assuming the transmitter (TX) to be partially cooperative, its signal can be accessible directly using a directional coupler. Moreover, based on the digital nature of the exploited signals of opportunity, the attractive possibility has been also investigated of avoiding the use of a dedicated receiving channel for the reference signal; this is instead synthesized it from the surveillance channel by de-modulating and then re-modulating the transmitted symbols sequence according to the standard specifications, [35].

Reference signal conditioning. PBR operation inherently implies that the transmitted waveform is not within the control of the radar designer. This contrasts to the usual case of conventional radar systems, where the transmitted waveform is carefully designed to provide an ambiguity function (AF) with appropriate properties (e.g., narrow peak in both range and Doppler and low sidelobes). In particular, digital waveforms are usually characterized by a number of undesired peaks or high sidelobes in the corresponding AF. Therefore, it might be necessary to perform some transmitter-specific conditioning of the reference signal to improve the resulting mismatched AF. In WiFi transmissions the sidelobe structures appearing in the range dimension highly depend on the adopted modulation scheme, i.e. direct sequence spread spectrum (DSSS) or orthogonal frequency-division multiplexing (OFDM), and might show a severe masking effect on small targets, [34]. Thus, proper techniques have been introduced to cope with this undesired effect in PBR systems based on WiFi transmissions exploiting DSSS and/or OFDM modulation, [41]-[42].

As an example, when exploiting DSSS transmission, a Peak Side Ratio (PSR) lower than 21 dB is obtained. In this case, according to the DSSS specifications, the baseband signal is chipped at 11 MHz with an 11-chip PN code so that each symbol duration  $T_{SYM}$  is exactly 11 chip long ( $T_{SYM} = 1\mu s$ ). Figure 2 reports in blue curve the temporal Auto Correlation Function (ACF) obtained for a simulated DSSS-based signal. It is dominated by the ACF of the 11-chip Barker code which yields five identical lobes on both sides of the main lobe with a temporal separation equal to  $2T_C$ , being  $T_C = T_{SYM}/11 \mu s$  the chip duration, and a PSR equal to  $20 \log(11) = 20.8 \text{ dB}$ . Moreover, additional strong sidelobes appear at delay multiple of  $T_{SYM}(k \cdot 150 \text{ m})$ ; these sidelobe structures are due to the cyclical repetition of the Barker code. Notice that both the range sidelobes related to the Barker code adopted by the DSSS modulation and those depending on the average cross-correlation among consecutive transmitted symbols cannot be counteracted by using standard networks. The result of the application of the technique developed in [35], [41]-[42] is reported in Figure 2 in red curve. In this case, notice that the application of the considered approach provides a significant improvement of the PSR with only a very limited loss in SNR.

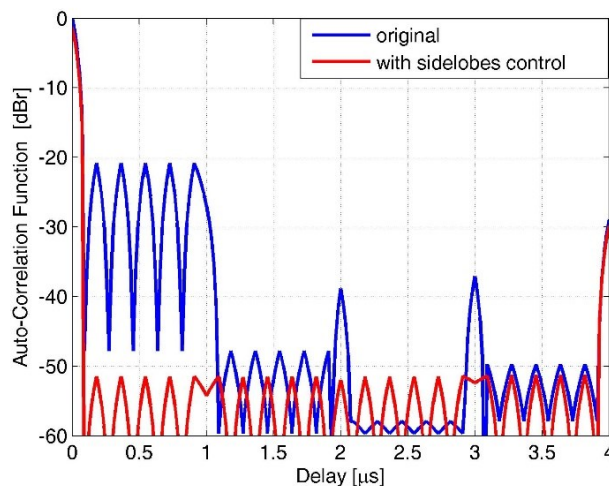


Figure 2. Auto-Correlation Function with sidelobes control for a DSSS signal.

Disturbance cancellation. The pre-conditioned reference signal is first used to remove undesired contributions that have been received, along with the moving target echo, on the surveillance channel due to the direct signal from the TX and its multipath rays (i.e., bounces on stationary obstacles). To this purpose we resort to the adaptive cancellation approach presented in [44], the Extensive Cancellation

Algorithm (ECA), which operates by subtracting from the surveillance signal  $s_s(t)$  proper scaled and delayed replicas of the reference signal  $s_r(t)$ .

Specifically, by sampling the received signals at  $f_s$  and assuming that the multipath echoes are backscattered from the first  $K$  range bins, the output of the ECA is evaluated as:

$$s_{ECA}[n] = s_s[n] - \sum_{k=0}^{K-1} \alpha_k s_r[n-k] \quad n = 0, \dots, N-1 \quad (1)$$

being  $N$  the number of samples within the coherent processing interval (CPI)  $T_{int}$ . The filter coefficients  $\boldsymbol{\alpha} = [\alpha_0 \ \alpha_1 \ \dots \ \alpha_{K-1}]^T$  are evaluated by resorting to a Least Square (LS) approach that minimizes the power of the signal at the output of the filter:

$$\boldsymbol{\alpha} = (\mathbf{S}_r^H \mathbf{S}_r)^{-1} \mathbf{S}_r^H \mathbf{s}_s \quad (2)$$

where  $\mathbf{s}_s$  is a  $N \times 1$  vector containing  $N$  samples of the surveillance signal and  $\mathbf{S}_r$  is a  $N \times K$  matrix whose columns are the delayed versions of the reference signal. As is apparent, in its original version, the ECA requires the filter weights to be estimated over the whole CPI.

For the considered application, the batch version of the ECA (ECA-B) is adopted, which requires the filter weights to be estimated over smaller portions of the integration time. Specifically, the ECA-B output at the  $l$ -th batch is written as

$$s_{ECA-B}[n] = s_s[n] - \sum_{k=0}^{K-1} \alpha_k^{(l)} s_r[n-k] \quad (3)$$

$$n = lN_B, \dots, (l+1)N_B - 1; \quad l = 0, \dots, B-1$$

where  $N_B$  is the dimension of each batch,  $B = \lfloor \frac{N}{N_B} \rfloor$  is the number of batches, and  $\boldsymbol{\alpha}^{(l)} = [\alpha_0^{(l)} \ \alpha_1^{(l)} \ \dots \ \alpha_{K-1}^{(l)}]^T$  is the filter coefficients estimate obtained at the  $l$ -th batch, namely by exploiting the  $l$ -th signal fragment of duration  $T_B = N_B/f_s$ . Basically we have

$$\boldsymbol{\alpha}^{(l)} = [\mathbf{S}_r^{(l)H} \mathbf{S}_r^{(l)}]^{-1} \mathbf{S}_r^{(l)H} \mathbf{s}_s^{(l)} \quad (4)$$

where  $\mathbf{s}_s^{(l)} = [s_s[lN_B], s_s[lN_B + 1], \dots, s_s[(l+1)N_B - 1]]^T$  is a  $(N_B \times 1)$  vector and  $\mathbf{S}_r^{(l)}$  is a  $N_B \times K$  matrix collecting the delayed copies of the corresponding reference signal fragment.

Reducing the temporal dimension of the single batch within certain limits does yield significant adaptivity loss when operating in a stationary environment. However, it was demonstrated in [44] to make the system more robust to the slowly varying characteristics of the environment; this appears to be an appreciable advantage in the considered application, especially in outdoor scenarios. However, reducing the batch duration widens the filter cancellation notch in the Doppler dimension, so that it should be traded with the minimum target detectable velocity to be guaranteed.

Range compression and 2D-CCF evaluation. After the cancellation stage, the detection process is based on the evaluation of the bistatic two-dimensional (range-velocity) cross-correlation function (2D-CCF) between the surveillance and the reference signal:

$$C[l, p] = \left| \sum_{n=0}^{N-1} s_s[n] \cdot s_r^*[n-l] \cdot e^{-j2\pi \frac{pn}{N}} \right|^2 \quad (5)$$

where

-  $l$  is the time bin representing the time delay  $\tau[l]=lf_s$ ; the time delay can be converted in a bistatic range difference by defining the corresponding range bin as  $\Delta R[l] = c \cdot \tau[l]$  being  $c$  the speed of light;

-  $p$  is the Doppler bin representing the Doppler frequency  $f_D[p]=pf_s/N$ ; the Doppler frequency can be converted in a bistatic velocity by defining the corresponding velocity bin as  $\Delta v[l] = \lambda f_D[p]$ , being  $\lambda$  the center wavelength of the exploited transmission.

Based on the pulsed nature of WiFi transmissions and observing that the pulse duration is significantly smaller than the CPI required to achieve the desired SNR and Doppler resolution for the considered applications, eq. (5) can be approximated as follows:

$$C[l, p] \approx \left| \sum_{m=0}^{M-1} e^{-j2\pi \frac{p i_m}{N_{int}}} \sum_{n=0}^{N_m-1} s_s[i_m+n] \cdot s_r^*[i_m+n-l] \right|^2 = \left| \sum_{m=0}^{M-1} e^{-j2\pi \frac{p i_m}{N_{int}}} \chi^{(m)}[l] \right|^2 \quad (6)$$

where  $M$  is the number of pulses transmitted during the CPI,  $N_m$  is the number of samples in the  $m$ -th pulse,  $i_m$  is the time index corresponding to the first sample of the  $m$ -th pulse, and  $\chi^{(m)}[l]$  is the  $l$ -th sample of the temporal CCF among the surveillance and the reference signal evaluated over the  $m$ -th pulse. As it is apparent, eq. (6) can be practically evaluated by cross-correlating the surveillance signal with the reference signal on a pulse basis (“Range compression” block in Figure 1) and coherently integrating the obtained results over consecutive pulses (“Range-Velocity Map Evaluation” block in Figure 1). At this latter stage, an ad hoc designed taper function can be exploited to control the sidelobes of the AF in the Doppler dimension, [43].

Notice that possible limitations to the WiFi-based PBR operation at this stage might be due to interference from other APs used in the same area. However, if the interfering AP operates on adjacent (partially overlapped) frequency channels, its transmission is expected to yield just a limited increase in the system noise floor. This can be explained by observing that (i) the received interfering signal does not correlate with the reference signal adopted for matched filtering, and (ii) the probability of collision between the same pair of APs is usually low so that only a small percentage of pulses in the CPI are affected by such interfering transmission. Different considerations apply when the interfering AP is operated in the same WLAN channel used by the AP of opportunity. In this case, the occurrences of collisions are substantially avoided thanks to the implementation of carrier sense multiple access (CSMA) protocols. Therefore, the effect of an interfering AP would be to inhibit a high rate transmission of pulses by the AP of opportunity. From a radar application point of view, this might upper limit the equivalent pulse repetition frequency and yields a highly variable temporal separation among consecutive pulses. In typical situations, this effect is responsible of high sidelobes to appear in the AF of the WiFi signal along the Doppler dimension. However, in [43] has been shown that it is possible to design effective taper functions to control such sidelobes at least in the Doppler range of interest. As an example, Figure 3(a) reports the temporal separations between consecutive pulses contained in the 0.5 s of the acquired data for a real WiFi signal [43]. As is apparent, the actual temporal separation measured over the train of consecutive pulses is highly variable and usually higher than 1 ms that is the nominal Beacon repetition interval. Figure 3(b) compare the original Doppler response and the one with weighting network; we observe as the weighting network proposed in [43] yields a PSR better than 25dB with limited SNR loss.

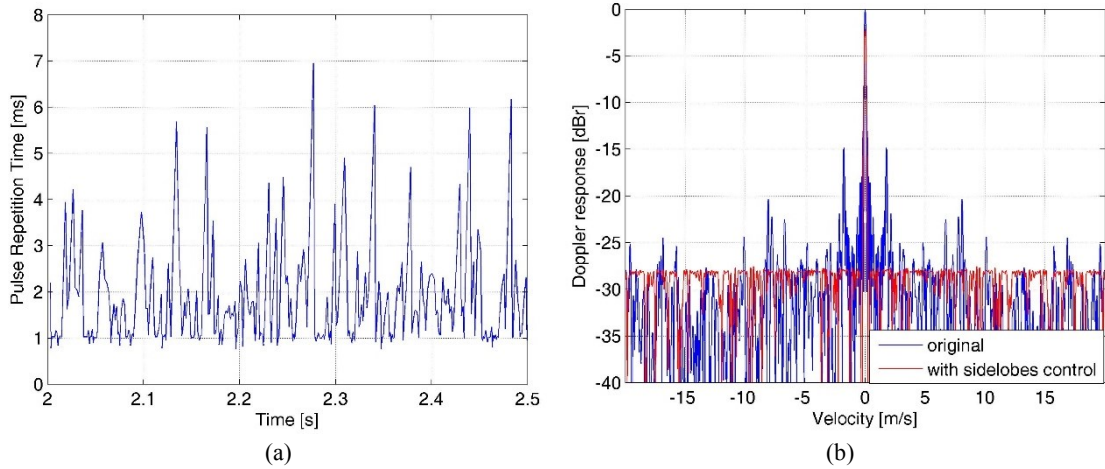
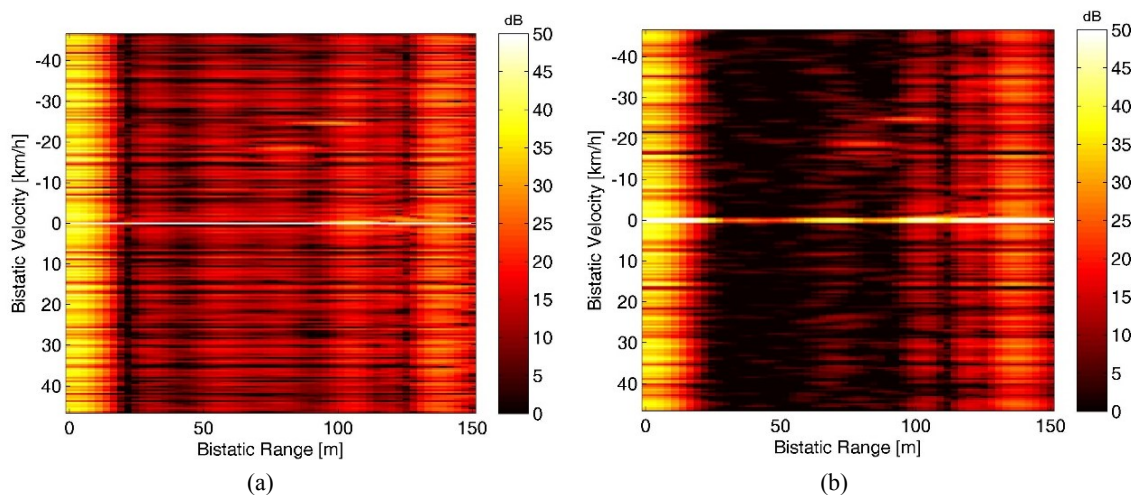


Figure 3. (a) Temporal separation between consecutive pulses in a real WiFi signal; (b) Doppler response with tapering.

As an example, to demonstrate the significant benefit deriving from the joint application of disturbance cancellation technique and sidelobes control, we report the 2D-CCF for an experimental test shown in [35]. In particular, two targets were present (a running man and a car) moving in a parking area. Figure 4(a) shows the 2D-CCF evaluated without disturbance cancellation and sidelobe control. As is apparent, in addition to the strong peak at zero range and zero velocity (corresponding to the direct signal), there are a large number of strong contributions at zero velocity that come with their severe sidelobe structure (spreading along the velocity axis) and clearly mask all target echoes. Figure 4(b) shows the 2D-CCF evaluated without disturbance cancellation but using the proposed sidelobe reduction. While the targets are detected, it is apparent that their detection is still limited by the small dynamic range available, since many returns, especially at zero Doppler are present in the map. This clearly shows that the disturbance cancellation can provide an additional advantage. Figure 4(c) reports the 2D-CCF evaluated after disturbance cancellation and sidelobe control. As is apparent the effective removal of the direct signal and all the disturbance contributions at zero Doppler significantly increases the useful dynamic range for target detection. Both the car (range 95 m and velocity -25 Km/h) and the human target (range 85 m and velocity -20 Km/h) now appear as strong peaks in the map, so they can be easily detected without ambiguities.





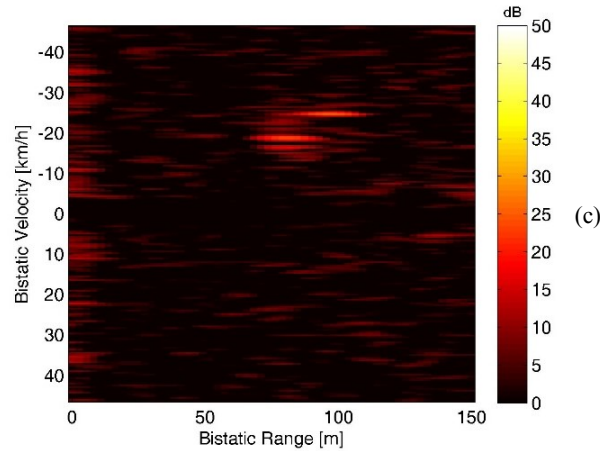


Figure 4. 2D-CCF between surveillance and reference signal for an experimental test. (a) Without disturbance cancellation and sidelobe control; (b) With sidelobe control; (c) With both disturbance cancellation and sidelobe control filters.

CFAR detection, Bistatic R-V tracking, and X-Y localization. A constant false alarm rate (CFAR) threshold can be then applied on the obtained map to automatically detect the potential targets according to a specific CFAR detection scheme. This provides a first target localization over the bistatic range/velocity plane. The measures collected at consecutive observations can be used to perform a line tracking over this plane. Using a conventional Kalman algorithm allows to reduce the false alarm rate while yielding more accurate range/velocity estimations. When target localization is required in an assigned area, it is in principle possible to estimate the target x-y coordinates. To this purpose, multiple passive radar sensors can be exploited which allow to collect a set of range/velocity measures for the same target which is observed at different bistatic geometries. Moreover, assuming that each sensor employs a couple of surveillance antennas, an interferometric approach can be exploited to estimate the Direction of Arrival (DoA) of the target echo. This obviously increases the set of available measures thus potentially improving the localization capability of the conceived system. However, since different measures (range/velocity/DoA) might be characterized by different accuracies, proper localization strategies should be designed to jointly exploit them, [36].

ISAR processing. The WiFi-based passive radar guarantees a range resolution limited to tenths meters due to the limited frequency bandwidth occupied by the available signals (e.g. 11 m - 18 m, depending on the adopted modulation). Additional resolution in cross-range direction could be achieved by coherently processing the returns from the target of interest when observed at different aspect angles. Particularly in ISAR the angular aperture needed to this purpose is obtained by exploiting the motion of the target itself, [64]. Therefore in [38] has been shown that a cross-range resolution considerably higher than the range one can be achieved by applying ISAR techniques to targets with a motion component in the cross-range direction.

The main required processing steps are sketched in Figure 1 in the dashed frame. Once a moving target has been detected, the corresponding range strip is selected from the compressed data by retaining the range bins of interest and fed in input to the ISAR processing block constituted by the cascade of target motion estimation, cross-range profile focusing and scaling. Specifically, for the short range surveillance application under consideration, both range and Doppler cell migration might be observed in the acquired range compressed data. This is due to the long CPI used, to the target velocity and its trajectory direction and to the relative position of both the transmitter and receiver with respect to the target. As typical in

ISAR, the target phase history in the ISAR CPI is approximated by a  $M$  degree polynomial law with coefficients  $a_i$  ( $i = 1, \dots, M$ ). In our case, for the considered short range acquisition geometry and motion conditions, usually it is sufficient to set  $M = 3$ .

Specifically in range direction the migration is related mainly to range walk due to the target radial velocity (namely  $\alpha_1$ ). As far as cross-range (Doppler) direction is concerned, the target phase history,  $\varphi_t(t) = 2\pi R_t(t)/\lambda$  in our application is characterized by quadratic and cubic phase terms, that need to be compensated to perform coherent integration over the long ISAR CPI required to achieve the high cross-range resolution. Unfortunately, as typical in the ISAR case, the target motion parameters are usually unknown and thus must be estimated from the received echoes via autofocus. To this purpose, a range strip centered on the range of the detected target is selected from the range compressed data and given as input to the target motion estimation procedure. An effective approach to obtain the parameter estimation is to search for the set of values  $(\alpha_1, \alpha_2, \alpha_3)$  that provides the best quality for the focused profile. Therefore, for any assigned set  $(\alpha_1, \alpha_2, \alpha_3)$  the procedure applies as follows:

- 1) remove the range migration related to  $\alpha_1$  by transforming the data in the fast-frequency slow-time domain, by multiplying the transformed data by

$$\Phi_1 = e^{j2\pi f \frac{2\alpha_1 t}{c}} \quad (7)$$

with  $f$  being the fast-frequency and by inverse Fourier transforming the data back in the range – slow time domain;

- 2) remove the Doppler migration related to  $\alpha_2$  and  $\alpha_3$  by multiplying the compensated range bin by the reference signal:

$$\Phi_2 = e^{j\frac{2\pi f}{\lambda}(\alpha_2 t^2 + \alpha_3 \frac{t^3}{3})} \quad (8)$$

and go in the cross-range profile domain by Fourier transform.

The estimated  $(\alpha_1, \alpha_2, \alpha_3)$  values can be chosen as those values which minimize the entropy  $H$ , [65],

$$H = - \sum_{r=1}^R P_r \ln(P_r), \quad P_r = \frac{I_r}{\sum_{r=1}^R I_r} \quad (9)$$

evaluated over the cross-range profile (intensity values)  $I_r = I_r(\alpha_1, \alpha_2, \alpha_3)$  at the output of step 2 above being  $R$  the number of bins composing the profile.

Once the estimate of  $\hat{\alpha}_2$  is obtained, also the target cross-range velocity  $\hat{v}_{cr}$  can be obtained, which is directly used to scale the Doppler axis, thus mapping Doppler frequencies into cross-range distances.



### 3. ADVANCED DISTURBANCE CANCELLATION TECHNIQUE FOR TARGET DETECTION

The disturbance cancellation represents one of the key stages within a conventional PBR processing scheme due to the fact that undesired signal contribution (above all the direct signal breakthrough and multipath, i.e. bounces on stationary obstacles) could mask weak target echoes. Different approaches have been proposed to cope with this problem yielding solutions with different complexity and effectiveness [66]-[72].

Among these approaches, a widely used cancellation technique is the ECA and its batches version (ECA-B) [44]. A number of contributions appeared in the open literature where the effectiveness of these cancellation approaches has been clearly demonstrated with reference to quite different PBR applications exploiting various waveforms of opportunity [11]-[12], [20], [73]-[78] included WiFi transmissions [35]-[38]. Nevertheless, in this Section we show that the ECA-B might yield some limitations when employed against highly time-varying disturbance scenarios in the presence of slowly moving targets.

Therefore, in this Section, an advanced version of the ECA is proposed for disturbance cancellation and target detection in passive radar.

Firstly, in sub-section 3.1 are shown some WiFi-based real-life examples to demonstrate the benefits of a batches operation; moreover, some specific limitations are identified when dealing with slowly moving targets. Specifically, the need to rapidly adapt the filter coefficients is shown to yield undesired effects on low Doppler target echoes, along with the expected partial cancellation. Therefore, in sub-section 3.2 a sliding version of the ECA (ECA-S) is presented which operates on partially overlapped signals batches and its effectiveness is demonstrated in sub-section 3.3 against live data set compared to previous ECA versions. Obviously, the benefit of ECA-S are paid in terms of computational load since the number of complex operations to be performed increases with the percentage of overlap between successively processed signal fragments. Therefore, sub-section 3.4 reports some expedients to enable an efficient implementation of the proposed approach.

---

#### 3.1. THE ECA AND ECA-BATCHES APPROACHES

##### 3.1.1. DISTURBANCE CANCELLATION CAPABILITY

As shown in Section 2, the ECA-B has been used to remove the undesired contributions in the surveillance channel. In its original version, the ECA requires the filter weights to be estimated by averaging over the whole CPI; in contrast, the ECA-B approach estimates and applies the filter weights over smaller portions (batches) of the integration time. Has been demonstrated in [44] to make the system more robust to the time-varying characteristics of the environment; this has been shown to be an appreciable advantage in many applications, especially when operating against non-stationary disturbance scenarios.

As an example, in this sub-section we report the results obtained using the experimental equipment described more in details in the sub-section 5.1. In particular, an AP was employed, set up to emit the beacon signal at 3 ms, and a quasi monostatic configuration was adopted for the surveillance and the transmitting antennas. Tests have been performed in a parking area using vehicles as cooperative targets.



In addition, in this specific application we were allowed to perform some target-free tests in order to evaluate the disturbance cancellation capability in controlled situations avoiding the target effects. To this purpose, an acquisition of 20 s is considered in the following that includes just disturbance contributions (direct signal and echoes from the stationary scene).

Figure 5 reports the cancellation performance along the acquisition time for the ECA-B operating over a range extension of 500 m with different durations of the batch. The reported clutter attenuation (CA) is defined as the ratio between the power levels measured, on the surveillance channel, at the input and at the output of the cancellation filter. In this application, the measured CA is close to the maximum theoretical expected value (29.4 dB) even operating with long batches (i.e. using a conventional ECA). In fact in this case, the system operates in a scenario that mostly includes man-made objects. Therefore the non-stationary behavior of the received signals is mostly due to the instabilities of both the transmitter and the receiver. Nevertheless the decrease of the batch duration allows a slight improvement in term of average CA: about 0.4 dB gain is obtained moving from  $T_B = 0.5$  s to  $T_B = 15$  ms (Figure 5(a) and Figure 5(d), respectively). Moreover, we observe that a much more stable CA is achieved along the acquisition time which clearly demonstrates the increased capability to adapt to the time-varying characteristics of the collected signals.

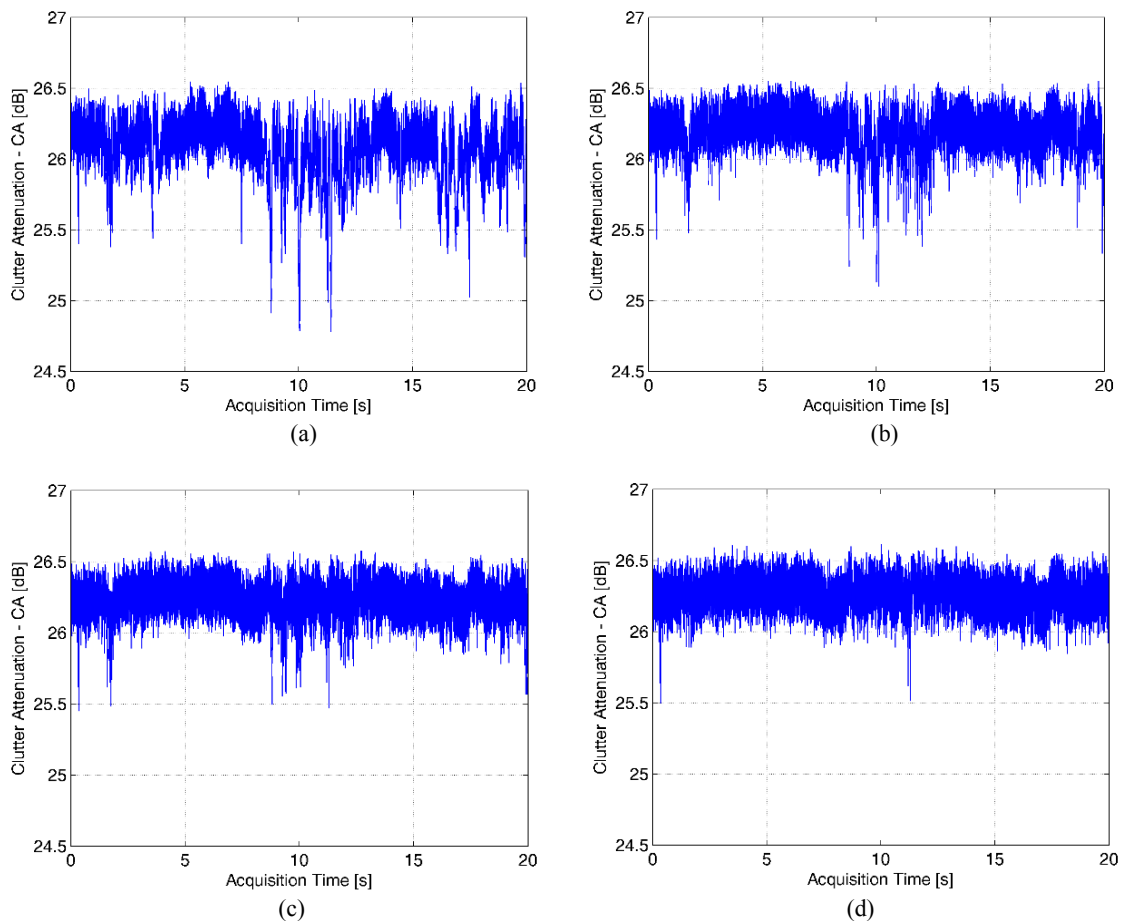


Figure 5. Clutter attenuation (CA) along the acquisition time for the ECA-B operating with different batch durations. (a)  $T_B = 0.5$  s; (b)  $T_B = 0.1$  s; (c)  $T_B = 50$  ms; (d)  $T_B = 15$  ms.

This analysis allows us to select a batch duration between 50 ms and 15 ms. Notice that, in this case it is not recommended to further decrease  $T_B$  since we recall that WiFi transmissions are of a pulsed type and, due to the exploited CSMA approach, the transmission may be inhibited for a long time thus yielding a high temporal separation among consecutive pulses. Therefore operating with very small batches there might be a high variability in the number of pulses included in each batch and, in extreme cases, this might yield empty batches.

### 3.1.2. LIMITATIONS OF THE ECA-B

The benefits of the ECA-B approach have been shown in the previous sub-section in term of disturbance cancellation capability. Specifically, it has been verified that, widening the cancellation notch by reducing the batch duration up to a certain limit allows a better removal of the disturbance contributions.

Obviously, this has a non negligible impact on the target echoes, especially those observed at low Doppler frequencies. However, we show that this impact is not limited only to the typical SNR loss due to the partial cancellation of slowly moving target echoes.

To this purpose we consider the 2D-CCF between the reference signal and the surveillance signal after the disturbance cancellation stage. The resulting map is a representation of the range-Doppler distribution of the signal energy at the output of the cancellation filter. Therefore its analysis gives a further insight into the performance of the considered cancellation algorithm.

Dealing with a WiFi-based PBR we consider short range applications, in which it is quite typical to deal with targets observed at low Doppler frequency, namely slowly-moving targets or targets moving mainly along the cross-range direction (red line in Figure 6). Therefore it is of interest to study the effect of the ECA-B on the detection of such targets. To this purpose we show the results obtained with the same experimental set-up used in the previous sub-section, for a test performed against a vehicular target moving in the cross-range direction with approximate speed 4.5 m/s and distance of minimum approach  $R_0 = 20$  m as shown in Figure 6. In such geometry, the target describes a parabolic trajectory on the bistatic range-Doppler plane and, for a long time, it will be observed at Doppler frequencies within or close to the cancellation filter notch.

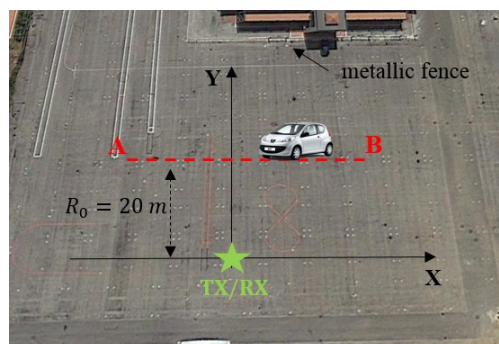


Figure 6. Sketch of a typical acquisition geometry.

As an example, Figure 7 and Figure 8 show the range-Doppler maps obtained after disturbance cancellation with a CPI  $T_{int} = 0.2$  s for two different positions of the target along its trajectory. Proper

techniques have been applied to control the sidelobes level of the signal ambiguity function [41]-[43]. All the reported maps have been normalized to thermal noise power level so that the value at each map location represents the estimated SNR. Notice that the dynamic range has been lower limited to better highlight the main structures arising in the map. The adopted cancellation filters operate over a range extension of 500 m with different values of the batch duration  $T_B$ .

Specifically, Figure 7 accounts for a favorable situation since the target Doppler frequency is reasonably high so that it is not affected by the cancellation stage. In fact, in this case, the ECA-B operates with  $T_B = 50$  ms that yields a notch Doppler extension equal to approximately  $1/T_B (= 1/50 \text{ ms} = 20 \text{ Hz})$  which is significantly smaller than the target Doppler value. As a consequence, after the cancellation stage, the target appears as a strong peak at 53 m and -41 Hz. In addition, a further peak is also visible at 161 m and -33 Hz caused by the double-bounce reflection of the target echo over the metallic fence delimiting the parking area.

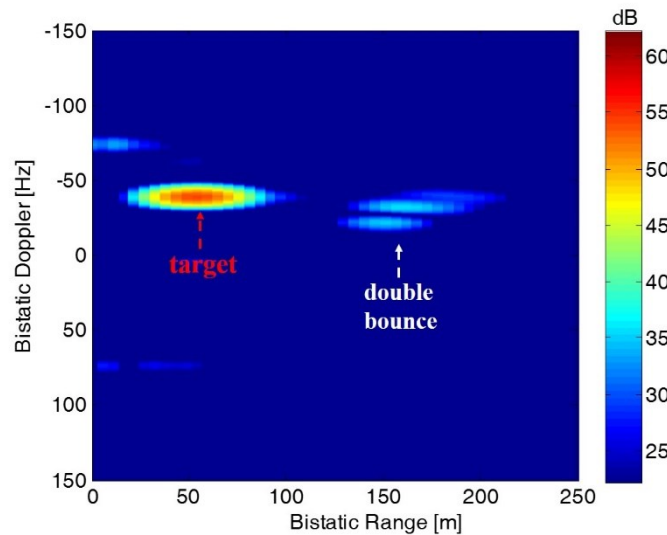


Figure 7. Range-Doppler map after ECA-B with  $T_B = 50$  ms in the case of a high Doppler target.

In contrast, Figure 8 shows the case of a target echo included in the filter notch so that it is expected to be strongly affected by the cancellation stage. In particular, Figure 8(a-c) have been obtained by using batch durations equal to  $T_B = 50$  ms,  $T_B = 30$  ms, and  $T_B = 15$  ms, respectively.

As is apparent, in all cases, the target peak is surrounded by undesired structures in the Doppler dimension that might be responsible of useful dynamic range reduction or masking effects over weak targets, thus limiting the detection capability. These Doppler ambiguities are mainly due to the ECA-B approach that exploits consecutive batches of the received signals where the filter coefficients are separately estimated and applied. In fact this yields discontinuities in the target echo at the output of this stage appearing at regular intervals of  $T_B$  thus setting the Doppler spacing between unwanted peaks ( $1/T_B$ ).

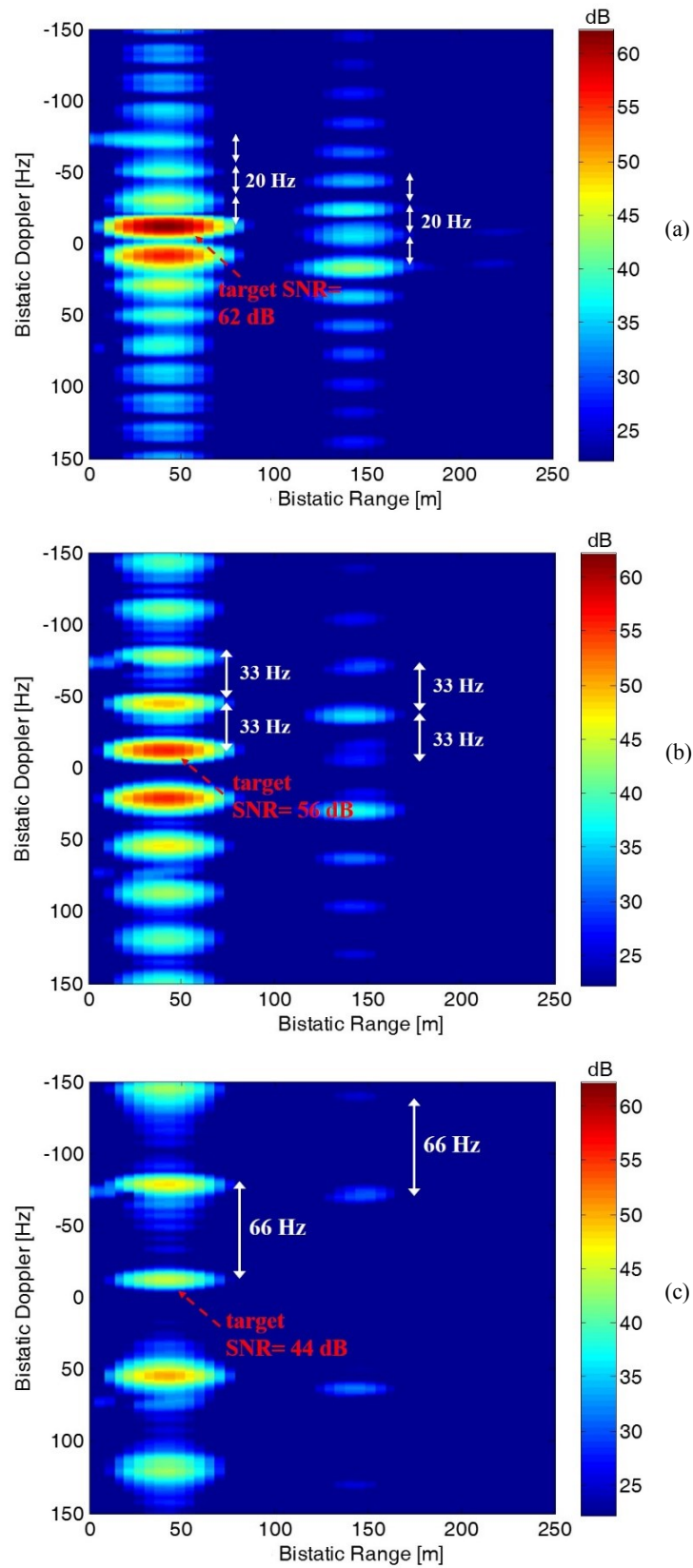


Figure 8. Range-Doppler maps after ECA-B for three different batch durations in the case of a low Doppler target: (a)  $T_B = 50$  ms; (b)  $T_B = 30$  ms; (c)  $T_B = 15$  ms.

This is demonstrated here with reference to the following simplifying hypotheses:

(i) the surveillance signal includes a single moving target echo observed with amplitude  $A_t$  at Doppler  $f_d$  with delay  $\tau = n_\tau/f_s$ , a single zero-Doppler replica of the transmitted signal received from the same target range cell (i.e. delay  $\tau$ ) with amplitude  $A_c$ , and thermal noise  $w_s$ :

$$s_s[n] = A_t d[n - n_\tau] e^{j2\pi f_d n/f_s} + A_c d[n - n_\tau] + w_s[n] \quad n = 0, \dots, N - 1 \quad (10)$$

where  $d[n]$  is the signal emitted by the illuminator of opportunity with unitary average power. Notice that the zero-Doppler term in (10) might represent either the direct signal from the transmitter or a stationary multipath contribution.

(ii) The reference signal is an ideal noise-free copy of the transmitted signal:  $s_r[n] = A_r d[n]$ ,  $n = 0, \dots, N - 1$ .

(iii) The ECA filter operates with a single tap, i.e.  $K = 1$ , against the sole range cell at delay  $\tau$  that includes both the target and the multipath echoes. Without loss of generality we further assume that  $\tau = n_\tau/f_s = 0$ .

With the positions above, the filter in eq. (2) and (4) reduces to a single complex coefficient. In particular, at the  $l$ -th batch ( $l = 0, \dots, \lfloor \frac{N}{N_B} \rfloor - 1$ ), it can be written as:

$$\alpha_0^{(l)} = \frac{1}{\|\mathbf{s}_r^{(l)}\|^2} \mathbf{s}_r^{(l)H} \mathbf{s}_s^{(l)} = \frac{1}{|A_r|^2 \|\mathbf{d}^{(l)}\|^2} \left[ A_r^* A_t \mathbf{d}^{(l)H} \mathbf{d}_{f_d}^{(l)} + A_r^* A_c \|\mathbf{d}^{(l)}\|^2 + A_r^* \mathbf{d}^{(l)H} \mathbf{w}_s^{(l)} \right] \quad (11)$$

where  $\mathbf{d}^{(l)}$  is the  $N_B \times 1$  vector containing the  $l$ -th batch of the direct signal and  $\mathbf{d}_{f_d}^{(l)}$  is its Doppler shifted version.

Consequently, the output of the ECA-B at the  $l$ -th batch is:

$$\begin{aligned} \mathbf{s}_{ECA-B}^{(l)} &= \mathbf{s}_s^{(l)} - \alpha_0^{(l)} \mathbf{s}_r^{(l)} = \\ &= A_t \mathbf{d}_{f_d}^{(l)} - \frac{A_t}{\|\mathbf{d}^{(l)}\|^2} \mathbf{d}^{(l)H} \mathbf{d}_{f_d}^{(l)} \mathbf{d}^{(l)} + \mathbf{w}_s^{(l)} - \frac{1}{\|\mathbf{d}^{(l)}\|^2} \mathbf{d}^{(l)H} \mathbf{w}_s^{(l)} \mathbf{d}^{(l)} \end{aligned} \quad (12)$$

where the original stationary disturbance contribution in the surveillance signal has been perfectly removed thanks to the simplifying hypotheses above. As is apparent the ECA-B output includes the ideal target contribution,  $A_t \mathbf{d}_{f_d}^{(l)}$ , along with an additional zero-Doppler contribution whose amplitude depends both on the target amplitude  $A_t$  and on the target Doppler frequency via the scalar product  $\mathbf{d}^{(l)H} \mathbf{d}_{f_d}^{(l)}$ . Therefore this term cannot be neglected for slowly moving target echoes, i.e. targets observed at low Doppler frequencies, and it encodes the partial removal of the target echo due to the application of the cancellation filter. Similarly, the original thermal noise contribution,  $\mathbf{w}_s^{(l)}$ , is present together with a noise-dependent term which yields the theoretical upper bound to the achievable cancellation of zero-Doppler contributions.

Then we can evaluate the output of the range-Doppler map for the range bin of the target at the generic Doppler frequency  $f_0$ :

$$\chi[f_0] = \mathbf{d}_{f_0}^H \mathbf{s}_{ECA-B} = \mathbf{d}_{f_0}^H \begin{bmatrix} \mathbf{s}_{ECA-B}^0 \\ \vdots \\ \mathbf{s}_{ECA-B}^{B-1} \end{bmatrix} = \sum_{l=0}^{B-1} \mathbf{d}_{f_0}^{(l)H} \mathbf{s}_{ECA-B}^{(l)} \quad (13)$$



Substituting (12) into (13) we obtain:

$$\begin{aligned} \chi[f_0] = & \sum_{l=0}^{B-1} A_t \mathbf{d}_{f_0}^{(l)H} \mathbf{d}_{f_d}^{(l)} - \sum_{l=0}^{B-1} \frac{A_t}{\|\mathbf{d}^{(l)}\|^2} \mathbf{d}^{(l)H} \mathbf{d}_{f_d}^{(l)} \mathbf{d}_{f_0}^{(l)H} \mathbf{d}^{(l)} + \\ & + \sum_{l=0}^{B-1} \left[ \mathbf{d}_{f_0}^{(l)H} - \frac{1}{\|\mathbf{d}^{(l)}\|^2} \mathbf{d}_{f_0}^{(l)H} \mathbf{d}^{(l)} \mathbf{d}^{(l)H} \right] \mathbf{w}_s^{(l)} \end{aligned} \quad (14)$$

Aiming at understanding the impact of the ECA-B on the target echo, we focus our attention on the first two terms in eq. (14). Specifically, for the first term we might write:

$$\chi_I[f_0] = \sum_{l=0}^{B-1} A_t \mathbf{d}_{f_0}^{(l)H} \mathbf{d}_{f_d}^{(l)} = A_t \mathbf{d}_{f_0}^H \mathbf{d}_{f_d} = A_t \sum_{n=0}^{N-1} |d[n]|^2 e^{-j2\pi(f_0-f_d)n/f_s} \quad (15)$$

This term represents the ideal target contribution at the output of the 2D-CCF and its shape in the Doppler dimension strongly depends on the signal ambiguity function. As expected, for a constant modulus signal, eq. (15) yields the typical  $\sin(Nx)/\sin(x)$  shape centered in  $f_0 = f_d$  with peak amplitude  $A_t N$ , main lobe width  $f_s/N = 1/T_{int}$ , and period  $f_s$ :

$$\chi_I[f_0] = A_t \frac{\sin[\pi(f_d - f_0) N/f_s]}{\sin[\pi(f_d - f_0)/f_s]} e^{j\pi(f_d-f_0)(N-1)/f_s} \quad (16)$$

The second term in eq. (14) can be written as:

$$\chi_{II}[f_0] = A_t N_B^2 \sum_{l=0}^{B-1} \frac{1}{\|\mathbf{d}^{(l)}\|^2} g^{(l)}(f_d) [g^{(l)}(f_0)]^* \quad (17)$$

where  $g^{(l)}(f) = \mathbf{d}^{(l)H} \mathbf{d}_f^{(l)}/N_B$  is the output of the zero-Doppler filter for a unitary input signal with Doppler shift  $f$ . Notice that, for a constant amplitude signal, it results

$$g^{(l)}(f) = \frac{1}{N_B} \sum_{n=lN_B}^{(l+1)N_B-1} |d[n]|^2 e^{j2\pi f n/f_s} = g^{(0)}(f) e^{j2\pi f l N_B/f_s} \quad (18)$$

being

$$g^{(0)}(f) = \frac{1}{N_B} \sum_{n=0}^{N_B-1} e^{j2\pi f n/f_s} = \frac{1}{N_B} \frac{\sin[\pi f N_B/f_s]}{\sin[\pi f/f_s]} e^{j\pi f (N_B-1)/f_s} \quad (19)$$

and eq. (17) becomes:

$$\begin{aligned} \chi_{II}[f_0] = & A_t N_B g^{(0)}(f_d) [g^{(0)}(f_0)]^* \sum_{l=0}^{B-1} e^{j2\pi(f_d-f_0)lN_B/f_s} = \\ = & A_t N_B g^{(0)}(f_d) [g^{(0)}(f_0)]^* \frac{\sin[\pi(f_d - f_0) B N_B/f_s]}{\sin[\pi(f_d - f_0) N_B/f_s]} e^{j\pi(f_d-f_0)(B-1)N_B/f_s} \end{aligned} \quad (20)$$

As is apparent  $\chi_{II}[f_0]$  includes a  $\sin(Bx)/\sin(x)$  shaped factor centered in  $f_0 = f_d$  with period  $f_s/N_B = 1/T_B$ . Notice that its main lobe width coincides with that in eq. (16) whereas its peak amplitude is modulated by the product  $G(f_d, f_0) = g^{(0)}(f_d)[g^{(0)}(f_0)]^*$  which separately depends on the target Doppler frequency  $f_d$  and the Doppler of interest  $f_0$  and we have  $|G(f_d, f_0)| \leq 1$ .

Let us consider the global output at specific Doppler values.

Setting  $f_0 = f_d$  we infer that the target peak value is subject to a loss due to the cancellation stage. In fact in this case we obtain:

$$\chi[f_d] = \chi_I[f_d] - \chi_{II}[f_d] = A_t N \left\{ 1 - \left| \frac{1}{N_B} \frac{\sin[\pi f_d N_B / f_s]}{\sin[\pi f_d / f_s]} \right|^2 \right\} \quad (21)$$

As expected, for a given batch duration, the loss depends on the target Doppler frequency and cannot be neglected as far as  $|f_d| < 1/T_B$ .

It is interesting to evaluate the output at the ambiguous peaks of the  $\sin(Bx)/\sin(x)$  term in (20), i.e. for  $|f_0 - f_d| = \frac{p}{T_B}$  ( $p \in \mathbb{Z}, p \neq 0$ ). First of all we observe that this condition does not guarantee that both  $f_0$  and  $f_d$  are multiples of  $\frac{1}{T_B}$ , so that in the general case  $G(f_d, f_0) \neq 0$  and the Doppler ambiguities clearly appear in the final map:

$$\left| \chi \left[ f_d + \frac{p}{T_B} \right] \right| = \left| A_t \frac{N}{N_B^2} \frac{\sin[\pi f_d N_B / f_s]}{\sin[\pi f_d / f_s]} \frac{\sin \left[ \pi \left( f_d + \frac{p}{T_B} \right) N_B / f_s \right]}{\sin \left[ \pi \left( f_d + \frac{p}{T_B} \right) / f_s \right]} \right| \quad (22)$$

For a slowly moving target included in the cancellation notch, i.e.  $|f_d| < 1/T_B$ , the first  $\sin[N_B x]/\sin[x]$  factor has non negligible value while the amplitude of the second factor decreases as  $|p|$  increases. Therefore, in such conditions the target response at the output of the 2D-CCF map shows Doppler ambiguities separated by  $1/T_B$  with amplitudes decaying at high Doppler frequencies.

This is clearly the case observed in Figure 8. Notice that as the batch duration decreases, the Doppler ambiguities spread accordingly. In addition, the cancellation notch is widened and the target SNR is progressively reduced. Further decreasing  $T_B$  would allow the undesired structures to be moved out of the Doppler range of interest. However, this would also yield a more severe slowly-moving target removal and additional adaptivity loss since the disturbance characteristics would be estimated on few signal samples.

These considerations exacerbate in severe scenarios (i.e. those characterized by rapidly varying disturbance characteristics, possibly induced by co- and inter-channel interference, severe multipath, transmitter dependent effects, etc.) where it may be necessary to frequently update the filter coefficients to effectively remove the disturbance. In fact, operating with the ECA-B this is tantamount to the request for batches of extremely small dimension. Unluckily, this results in a considerable widening of the cancellation filter notch thus including even fast moving targets.



### 3.2. THE ECA-SLIDING TECHNIQUE

Based on the previous analysis, when the ECA-B approach is applied, special attention should be devoted to the selection of the batch duration as it affects both the capability to effectively remove the disturbance contributions possibly showing a non-stationary behavior and the possibility to nicely preserve the target echo.

Specifically the two requirements above might set opposite constraints on the selection of  $T_B$ . Long  $T_B$  should be selected to reduce the minimum detectable velocity and to limit the adaptivity loss. In contrast, short  $T_B$  should be preferred to be effective against disturbance with rapidly varying characteristics and to move the target Doppler ambiguities out of the observed Doppler extent.

To overcome this limitation, we propose a sliding version of the ECA (ECA-S) which operates over partially overlapped signal fragments (see Figure 9). This allows to decouple the selection of the batch duration exploited for the filter estimation and the update rate of the filter coefficients so that the requirements above could be more flexibly traded for.

Basically a new parameter is introduced,  $T_S$ , that represents the signal fragment processed using a given filter estimate; apparently,  $T_S$  also coincides with the temporal separation between consecutive updates of the filter coefficients. Thus ECA-S output at the  $l$ -th fragment is written as

$$s_{ECA-S}[n] = s_s[n] - \sum_{k=0}^{K-1} \alpha_k^{(l,T_A)} s_r[n-k] \quad (23)$$

$$n = lN_S, \dots, (l+1)N_S - 1; l = 0, \dots, B_S - 1$$

where  $N_S$  is the dimension of each fragment (i.e.  $N_S = T_S f_s$ ),  $B_S = \lfloor \frac{N}{N_S} \rfloor$  is the number of consecutive fragments in the CPI, and  $\boldsymbol{\alpha}^{(l,T_A)} = [\alpha_0^{(l,T_A)} \alpha_1^{(l,T_A)} \dots \alpha_{K-1}^{(l,T_A)}]^T$  are the current filter coefficients. The latter are adaptively estimated on a longer signal fragment of duration  $T_A = N_A/f_s$ , symmetrically taken around the current signal fragment to be processed (see Figure 9). Basically  $\boldsymbol{\alpha}^{(l,T_A)}$  are evaluated as

$$\boldsymbol{\alpha}^{(l,T_A)} = [\mathbf{s}_r^{(l,T_A)H} \mathbf{S}_r^{(l,T_A)}]^{-1} \mathbf{s}_r^{(l,T_A)H} \mathbf{s}_s^{(l,T_A)} \quad (24)$$

where the surveillance vector is given by

$$\mathbf{s}_s^{(l,T_A)} = \left[ s_s \left[ lN_S + \frac{N_S - N_A}{2} \right], s_s \left[ lN_S + \frac{N_S - N_A}{2} + 1 \right], \dots, s_s \left[ lN_S + \frac{N_S + N_A}{2} - 1 \right] \right]^T (N_A \times 1) \quad (25)$$

and  $\mathbf{S}_r^{(l,T_A)}$  is a  $N_A \times K$  matrix collecting the delayed copies of the corresponding reference signal fragment of duration  $T_A$ . Obviously, with the ECA-B approach we have  $T_B = T_S = T_A$ .



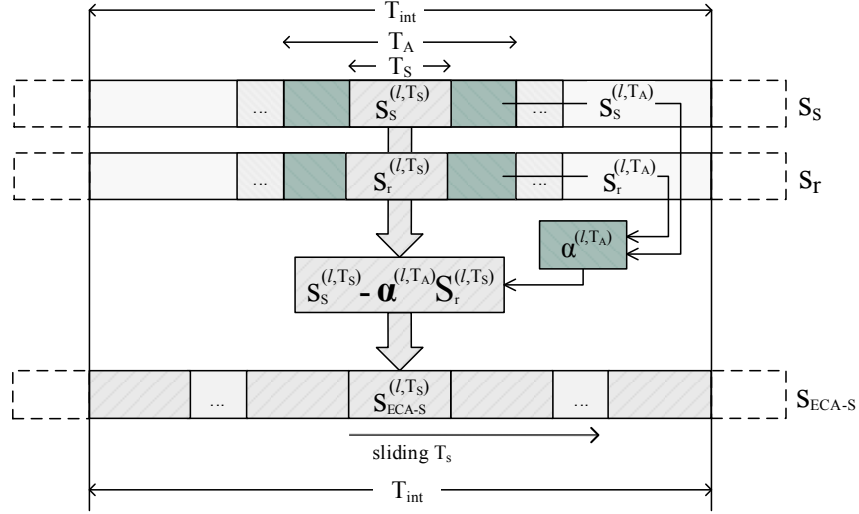


Figure 9. Block diagram of ECA-S.

Based on the ECA-S cancellation algorithm, the theoretical derivation in sub-section 3.1.2 can be repeated under the same simplifying hypotheses. To this purpose, let us collect in vectors  $\mathbf{s}_s^{(l, T_s)}$  and  $\mathbf{s}_r^{(l, T_s)}$  the  $N_s$  samples of the  $l$ -th fragment of the surveillance and the reference signals, respectively:

$$\mathbf{s}_{s/r}^{(l, T_s)} = [s_{s/r}[lN_s], s_{s/r}[lN_s + 1], \dots, s_{s/r}[(l + 1)N_s - 1]]^T \quad (N_s \times 1) \quad (26)$$

These vectors include the  $N_s$  samples that are processed using the same filter weights according to (23). Therefore, eq. (23) can be written in matrix notation as:

$$\mathbf{s}_{ECA-S}^{(l, T_s)} = \mathbf{s}_s^{(l, T_s)} - \alpha_0^{(l, T_A)} \mathbf{s}_r^{(l, T_s)} \quad (27)$$

where

$$\alpha_0^{(l, T_A)} = \frac{1}{\|\mathbf{s}_r^{(l, T_A)}\|^2} \mathbf{s}_r^{(l, T_A)H} \mathbf{s}_s^{(l, T_A)} = \frac{1}{|A_r|^2 \|\mathbf{d}^{(l, T_A)}\|^2} [A_r^* A_t \mathbf{d}^{(l, T_A)H} \mathbf{d}_{fd}^{(l, T_A)} + A_r^* A_c \|\mathbf{d}^{(l, T_A)}\|^2 + A_r^* \mathbf{d}^{(l, T_A)H} \mathbf{w}_s^{(l, T_A)}] \quad (28)$$

being  $\mathbf{d}^{(l, T_A)}$  and  $\mathbf{d}_{fd}^{(l, T_A)}$  the  $N_A \times 1$  vectors containing the  $l$ -th overlapped batch of duration  $T_A$  of the direct signal and its Doppler shifted version.

Therefore, proceeding as in (13)-(14), we evaluate the output of the range-Doppler map for the range bin of the target at the generic Doppler frequency  $f_0$ :

$$\chi[f_0] = \sum_{l=0}^{B_S-1} A_t \mathbf{d}_{f_0}^{(l, T_s)H} \mathbf{d}_{fd}^{(l, T_s)} - \sum_{l=0}^{B_S-1} \frac{A_t}{\|\mathbf{d}^{(l, T_A)}\|^2} \mathbf{d}^{(l, T_A)H} \mathbf{d}_{fd}^{(l, T_A)} \mathbf{d}_{f_0}^{(l, T_s)H} \mathbf{d}^{(l, T_s)} + \sum_{l=0}^{B_S-1} \left[ \mathbf{d}_{f_0}^{(l, T_s)H} \mathbf{w}_s^{(l, T_s)} - \frac{1}{\|\mathbf{d}^{(l, T_A)}\|^2} \mathbf{d}_{f_0}^{(l, T_s)H} \mathbf{d}^{(l, T_s)} \mathbf{d}^{(l, T_A)H} \mathbf{w}_s^{(l, T_A)} \right] \quad (29)$$

Again, the first target contribution in (29) results:

$$\chi_I[f_0] = A_t \frac{\sin[\pi(f_d - f_0) N/f_s]}{\sin[\pi(f_d - f_0)/f_s]} e^{j\pi(f_d - f_0)(N-1)/f_s} \quad (30)$$

This coincides with eq. (16) since this term represents the ideal target contribution at the output of the 2D-CCF and it is not affected by the cancellation stage.

The second term in eq. (29) can be written as:

$$\chi_{II}[f_0] = A_t N_A N_S \sum_{l=0}^{B_S-1} \frac{1}{\|\mathbf{d}^{(l,T_A)}\|^2} g^{(l,T_A)}(f_d) [g^{(l,T_S)}(f_0)]^* \quad (31)$$

where

$$g^{(l,T_A)}(f) = \mathbf{d}^{(l,T_A)H} \mathbf{d}_f^{(l,T_A)} / N_A = \frac{1}{N_A} \sum_{n=lN_S + \frac{N_S + N_A - 1}{2}}^{lN_S + \frac{N_S + N_A - 1}{2}} |d[n]|^2 e^{j2\pi f n / f_s} = g^{(0,T_A)}(f) e^{j2\pi f l N_S / f_s} \quad (32)$$

and

$$g^{(l,T_S)}(f) = \mathbf{d}^{(l,T_S)H} \mathbf{d}_f^{(l,T_S)} / N_S = \frac{1}{N_S} \sum_{n=lN_S}^{(l+1)N_S-1} |d[n]|^2 e^{j2\pi f n / f_s} = g^{(0,T_S)}(f) e^{j2\pi f l N_S / f_s} \quad (33)$$

being

$$g^{(0,T_A)}(f) = \frac{1}{N_A} \frac{\sin[\pi f N_A / f_s]}{\sin[\pi f / f_s]} e^{j\pi f (N_S - 1) / f_s} \quad (34)$$

and

$$g^{(0,T_S)}(f) = \frac{1}{N_S} \frac{\sin[\pi f N_S / f_s]}{\sin[\pi f / f_s]} e^{j\pi f (N_S - 1) / f_s} \quad (35)$$

Therefore eq. (31) becomes:

$$\chi_{II}[f_0] = A_t N_S g^{(0,T_A)}(f_d) [g^{(0,T_S)}(f_0)]^* \frac{\sin[\pi(f_d - f_0) B_S N_S / f_s]}{\sin[\pi(f_d - f_0) N_S / f_s]} e^{j\pi(f_d - f_0) N_S (B_S - 1) / f_s} \quad (36)$$

As is apparent, this term still include a  $\sin(B_S x) / \sin(x)$  factor; however in this case the period is set by the filter update rate. In other words, operating with the ECA-S approach, the Doppler ambiguities associated to low Doppler targets are expected to appear with Doppler separation equal to  $\frac{f_s}{N_S} = \frac{1}{T_S}$ . Therefore, a reasonable strategy to design this parameter is to select  $T_S$  so that to move out of the Doppler range of interest  $[-f_{Dmax}, f_{Dmax}]$  the undesired structures arising from the batch processing of the received signals. By imposing this condition for all the targets belonging to the cancellation notch area, we obtain  $T_S < \left(f_{Dmax} + \frac{1}{2T_A}\right)^{-1}$ . A good cancellation capability can be still guaranteed by acting on the other independent parameter  $T_A$ . Specifically this can be selected according to the analysis reported in sub-section 3.1.1, in order to allow remarkable cancellation performance against the time-varying

characteristics of the disturbance for the specific operative scenario; obviously, this should be partly traded with the minimum detectable velocity to be guaranteed.

In fact the target peak amplitude (i.e. for  $f_0 = f_d$ ) at the output of the 2D-CCF can be evaluated in this case as:

$$\chi[f_d] = \chi_I[f_d] - \chi_{II}[f_d] = A_t N \left\{ 1 - \frac{1}{N_S N_A} \frac{\sin[\pi f_d N_S / f_s] \sin[\pi f_d N_A / f_s]}{\sin[\pi f_d / f_s]} \right\} \quad (37)$$

As is apparent, the target SNR loss, and in turn, the cancellation notch width, depends on both  $T_A$  and  $T_S$ .

Notice that if the ECA-B operates with  $T_B = T_S$  aiming at excluding the ambiguities from the observed Doppler region, a wide cancellation notch could be achieved; in contrast the ECA-S yields the possibility to significantly narrow the cancellation notch by properly selecting  $T_A > T_S$ .

However, when the batch duration of the ECA-B is selected as  $T_B = T_A$  to maximize the cancellation capability, the ECA-S typically yields a wider Doppler extent of the cancellation area with respect to the ECA-B since the  $T_S$  value required to remove Doppler ambiguities is much smaller than  $T_A$  (see eqs. (37) and (21)). In other words, operating with the ECA-S allows to trade the ambiguities removal with a limited SNR loss. In turn, the latter can be traded with a small cancellation loss if  $T_A$  is slightly increased with respect to the initial choice  $T_A = T_B$ .

Based on the considerations above, we here address the design of the ECA-S parameters with reference to the case study considered in sub-section 3.1.1.

In particular, a batch duration  $T_A = 50$  ms has been shown to be a good compromise for effective disturbance removal and reasonable target echo preservation. Moreover, as the maximum Doppler frequency observed is  $f_{Dmax} = 70$  Hz, we might set  $T_S < 12.5$  ms.

---

### 3.3. PERFORMANCE ANALYSIS

The effectiveness of the sliding version of the ECA is shown in this sub-section with reference to the case studies considered in sub-section 3.1 (test against a vehicular target moving in the cross-range direction).

Specifically Figure 10 shows the range-Doppler map obtained with the ECA-S for the same data set considered in Figure 8. The adopted parameters are  $T_A = 50$  ms and  $T_S = 3$  ms; for a practical application, we set the filter update rate to be equal to the beacon emission rate of the exploited AP, i.e. the filter coefficients are updated beacon by beacon. Notice that, the batch duration  $T_A$  coincides with that used in Figure 8(a). We observe that, with the adopted parameters, the new version of the ECA allows to move the Doppler ambiguities out of the Doppler extent of interest so that a single peak appear for the vehicular target (aside from the double-bounce contribution). However, exploiting a batch duration  $T_A = 50$  ms for the adaptive filter coefficients estimation yields an effective removal of the disturbance and allows to better preserve the slowly moving target echo.

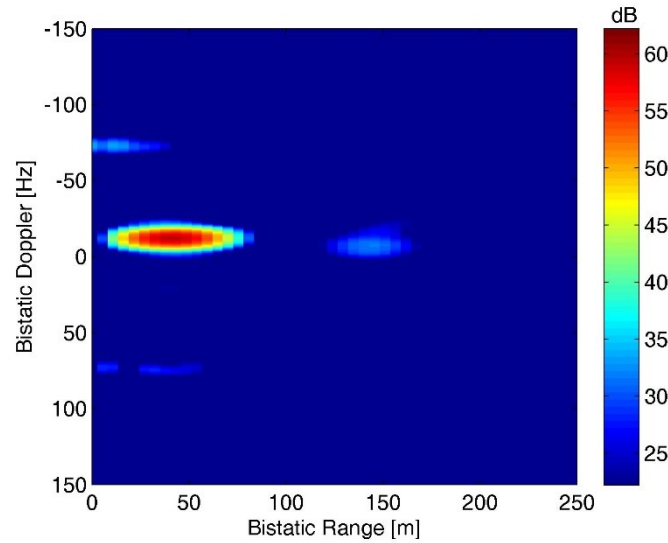


Figure 10. Range-Doppler map after ECA-S for  $T_B = 50$  ms and  $T_S = 3$  ms.

In addition, the improvement achieved by the proposed ECA-S approach is investigated in term of detection performance of the PBR system. This analysis allows us to gain a further insight into the operation of both the ECA-B and the ECA-S and to clearly demonstrate how the proposed modification recovers for the limitations identified in sub-section 3.1.

Figure 11 shows the detection results obtained with ECA-B and ECA-S for the same data set considered in sub-section 3.1. The data collected has been processed according to the WiFi-based passive radar processing scheme presented in Figure 1. In particular, the cancellation stage is performed by adopting the ECA-B or the ECA-S over a range of 500 m. A CPI of 0.2 s is then used to evaluate the bistatic range-velocity map over consecutive portions of the acquired signals (frames) with a fixed displacement of 0.1 s (10 frames per second are thus obtained); finally, target detection is performed by resorting to a standard cell-average CFAR threshold with a probability of false alarm equal to  $10^{-5}$ .

In Figure 11 we report the raw detections over the bistatic range/velocity plane collected along the whole acquisition (20 seconds). Specifically Figure 11(a) has been obtained after cancellation via ECA-B operating with  $T_B = 50$  ms while Figure 11(b) is the result of the application of the ECA-S. Notice that for ECA-S, the adopted parameters are  $T_A = 50$  ms and  $T_S = 3$  ms.

As is apparent, in both figures, in addition to the target returns (the cross-range movement of the target results in a parabolic sequence of detections over the range/velocity plane with vertex in (40;0)), there are also the double bounce returns caused by the reflection of the target echo over the metallic fence delimiting the parking area (parabolic sequence with vertex in (140;0)) and false alarms.

In addition, operating with the ECA-B yields a number of false plots due to Doppler ambiguities with 2.3 m/s spacing (corresponding to  $1/T_B = 20$  Hz). These ambiguities arise both from the main target echo and from its double-bounce return; however they are more evident in the first case due to the higher SNR of the originating echo. False tracks are usually discontinuous thanks to the masking effect of the real target echo at the detection stage. Nevertheless, they are quite apparent and might significantly limit the capability to identify and effectively track the true targets.

In contrast, we observe that the ECA-S allows to move the Doppler ambiguities out of the Doppler extent of interest while guaranteeing largely comparable detection capability against the true target echoes.

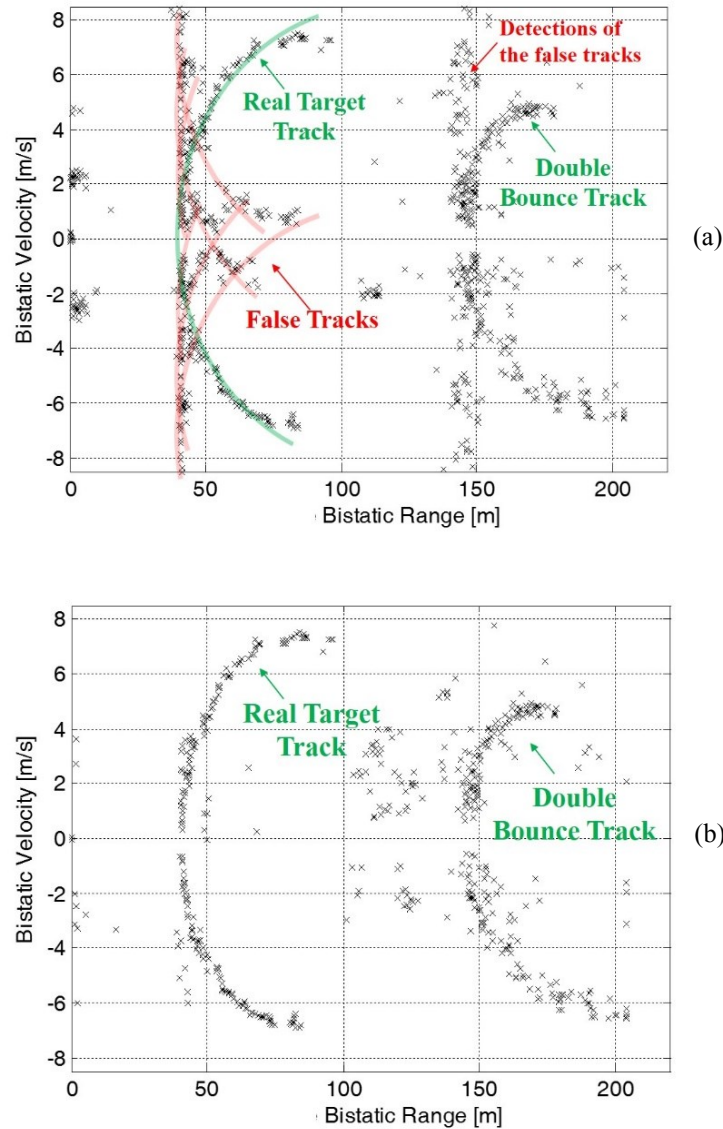


Figure 11. Detection results over the bistatic range-velocity plane when disturbance removal is performed via: (a) the ECA-B with  $T_B = 50$  ms; (b) the ECA-S with  $T_A = 50$  ms and  $T_S = 3$  ms.

Obviously, the above limitations of the ECA-B are apparent in PBR local area applications where it is quite typical to deal with slowly moving targets. Notice that, similar effects can be observed also in longer range applications, especially when exploiting signals of opportunity in the VHF or UHF band since there is a reasonable probability to observe a target at low Doppler frequency. This certainly applies to the maritime surveillance application where small boats or docked vessels might show very limited velocities. However, even in Air Traffic Control (ATC) applications, targets could be present moving mainly along the cross-range direction. This is shown in [J2] where the advantages yield by the proposed ECA-S are verified not only with reference to WiFi transmissions but also with reference two very different PBR applications. Specifically, a DVB-T-based PBR is considered is exploited for medium range maritime surveillance and a FM-based PBR is employed for typical ATC applications.



## 4. ENHANCED WIFI-BASED PASSIVE ISAR FOR VEHICULAR TARGETS

As briefly mentioned in Section 2, WiFi transmissions allow a range resolution typically limited to tenths of meters, due to the limited frequency bandwidth occupied by the available signals (e.g. 11-18 m, depending on the adopted modulation). For these reasons, it is of great interest to investigate the possibility to exploit the motion of the target itself in order to achieve a high resolution in the cross-range direction (up to tens of centimeters) by applying ISAR processing techniques.

Preliminary results along this line have been reported in [38] against vehicular targets and the basic ISAR scheme for cross-range has been shown in Figure 1 and briefly described in Section 2. In [38] has been proved that the disturbance cancellation stage is a mandatory step not only for target detection but also for the ISAR profiling. Nevertheless the background removal can have a non negligible effect on the target signal in input to the ISAR processing thus potentially degrading its cross-range profile formation; as a consequence, the processing techniques described in [38] and showed in Section 2 might yield limited performance especially when accurate profiling is required. In fact, when dealing with man-made targets typically ISAR techniques are employed to achieve high resolution products to be exploited by the classification and recognition procedures. In this case high quality products are needed in order to assure a reliable classification.

Although an optimization of the disturbance cancellation technique has been proposed in the previous Section, however, all ECA versions distort the target spectrum at very low Doppler frequency by inserting a cancellation notch.

Therefore, in this work an enhanced ISAR profiling technique is proposed to obtain an effective removal of such disturbance while preserving the target contribution and, consequently, the quality of the ISAR processing. Based on an iterative target preserving algorithm, the proposed processing strategy is shown to overcome the limitations of the other cancellation approaches.

The Section is organized as follow. In sub-section 4.1 the effect of the cancellation stage on ISAR product is discussed. Sub-section 4.2 introduces the innovative cancellation approach able to preserve the quality of the ISAR products and its effectiveness is analyzed preliminary against synthetic target echoes injected in real stationary background. In addition, the performance of the conceived technique and the resulting cross-range profiling capability of the WiFi-based PBR sensor are verified in sub-Section 4.3 against real vehicular targets moving in a parking area.

The reported results prove that reliable cross-range profiles can be achieved, fruitfully exploitable by a classification scheme based on an appropriate signatures database.

### 4.1. EFFECT OF THE DISTURBANCE CANCELLATION STAGE ON ISAR PRODUCTS

When dealing with man-made targets typically ISAR techniques are employed to achieve high resolution products to be exploited by the classification and recognition procedures. In this case, high quality products are needed in order to assure a reliable classification.

The results in [38] showed that the disturbance cancellation stage is essential for target detection and motion estimation but it has a non negligible effect on the target signal fed in input to the ISAR processing so that it might reduce the quality of the ISAR products. In fact, all ECA versions strongly

attenuate the target signal components at low Doppler frequencies since they are recognized as stationary contributions and included in the adaptive estimation of the cancellation weights. As a consequence, a considerable part of the target Doppler chirp can be lost and this potentially cause a degradation of the ISAR products. This degradation can occur in the case of slow-moving targets as well as in the case of targets moving along the cross-range direction, that are the most interesting ones to apply the ISAR processing schemes.

Therefore, in [38], an alternative cancellation approach has been presented. According to this approach, the cancellation filter weights have to be estimated and updated only at signal fragments that do not contain target contributions at low Doppler frequencies (being this information made available by the previous tracking stage). This in principle allows to remove the strongest disturbance components in the observed scene as they are stationary during the ISAR CPI. In contrast this prevents the cancellation of the target echoes as it crosses the zero-Doppler along its motion.

However, this approach has some limitations that may make it ineffective in a number of situations. In particular, in scenarios with possibly high density of targets, it could be very unlikely to identify a signal fragment that does not include low Doppler target echoes. As a result, the filter weights would be seldom updated so that the cancellation capability of slowly varying disturbance contributions can be seriously degraded. Notice that the slowly varying characteristics of the stationary background can be also ascribed to the instability of the employed receiver (phase noise of local oscillators, time jitter of ADC, etc.) so that the possibility to frequently update the filter coefficients is critical.

---

## 4.2. ENHANCED ISAR PROFILING TECHNIQUE

For the reasons above, in this work we present an innovative target preserving disturbance cancellation technique able to overcome the limitations of previous approaches and to provide enhanced quality profiles of moving man-made targets. Particularly sub-section 4.2.1 describes the new technique while sub-section 4.2.2 analyses the corresponding Point Spread Function (PSF) by injecting a moving point-like object into the real back-ground.

### 4.2.1. ITERATIVE TARGET PRESERVING (ITP) CANCELLATION ALGORITHM

To preserve the target signal for the following ISAR processing, its contribution to the received signal should be properly reduced prior to estimating the cancellation filter coefficients. To this purpose, the proposed approach exploits the output of the ISAR profiling stage to retrieve from it the signal contribution concerning the considered target and uses this recovered component to clean the received surveillance signal. In this way the estimation of the cancellation filter weights can be repeated using a signal with “target reduced” characteristics. By iteratively repeating the above steps, progressively a “target free” signal is made available for filter weights estimation and the low-frequency components of the target returns are better reconstructed.

Thus the proposed technique somehow follows a CLEAN-like philosophy [79]. The CLEAN algorithm has been used in passive radar in [39] and [80] with the purpose of removing stationary clutter and direct signal contributions from the received signal by operating in the signal domain or in the range–Doppler space.



In this work, the target cancellation stage benefits of an increased CPI duration that allows a more accurate estimate of the target contribution to be removed. In this regard, the proposed strategy resembles the approach of CLEAN techniques adopted in conventional radar imaging, [79], aimed at extracting those scatterers of the imaged targets typically masked by the sidelobes of dominant ones. This task is achieved by estimating the contribution from the dominant scatterers and progressively cleaning the image from them so that weak scatterers could be observed. In contrast, the objective of the proposed approach is to feed the adaptive stage of the ECA-S with a "target free" version of the received signal.

The block diagram of the proposed iterative target preserving (ITP) technique is sketched in Figure 12. First of all we observe that the disturbance cancellation has to be repeated at each iteration of the proposed algorithm. According to the processing scheme presented in Figure 1, this stage precedes the range compression so that an iterative cancellation approach would require a high computational load.

However, we point out that the two stages above can be nicely swapped by observing that

(i) the cancellation filter can be applied against the range compressed data  $\chi[q, n]$ , (where  $q$  is the range bin index and  $n$  accounts for the slow-time), and

(ii) the estimation of the filter weights might follow the evaluation of both the reference signal autocorrelation and the cross-correlation between the reference signal and the surveillance signal. In fact, the matrix  $\mathbf{S}_r^H \mathbf{S}_r$  ( $K \times K$ ) in (24) represents an estimated version of the reference signal autocorrelation matrix accounting for the first  $K$  time bins and obtained by averaging over the selected batch duration. Similarly, the  $K$ -dimensional vector  $\mathbf{S}_r^H \mathbf{s}_s$  in (24) represents an estimate of the cross-correlation between the reference signal and the surveillance signal which can be evaluated by averaging the results of the range compression stage over consecutive pulses. With the above position, the proposed approach can be easily integrated, as an advanced mode, in the basic processing scheme devoted to target detection and tracking.

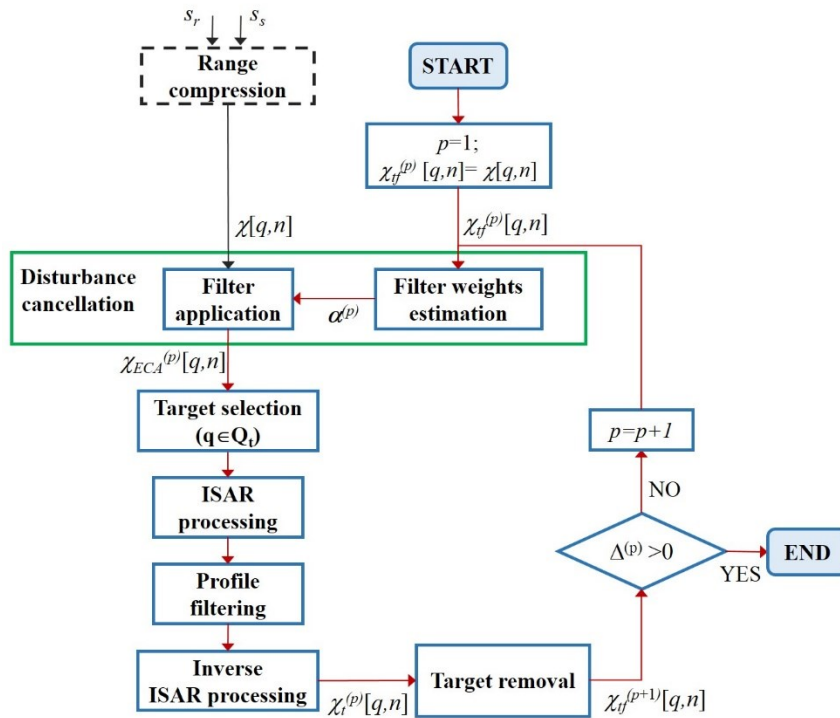


Figure 12. Block diagram of the ITP ISAR profiling technique.



At the p-th iteration of the proposed algorithm the following steps must be performed:

- 1) The weights  $\alpha^{(p)}$  of the ECA-S are adaptively estimated based on the current "target free" version of the surveillance signal  $\chi_{tf}^{(p)}[q, n]$  after range compression. At the first iteration (p=1) this signal coincides with the original range compressed signal.
- 2) The filter weights  $\alpha^{(p)}$  are applied against the original surveillance signal to obtain its disturbance free version  $\chi_{ECA}^{(p)}[q, n]$ . It has to be noticed that, at the first iteration, this output coincides with the standard ECA-S applied against the original data.
- 3) The signal at the selected target range strip is extracted (i.e.  $\chi_{ECA}^{(p)}[\bar{q}, n] \mid \bar{q} \in Q_t$ , where  $Q_t$  identifies the range bins spanned by the target along its motion) and fed in input to the ISAR processing stages that include the target motion estimation and its cross-range profile formation in the Doppler dimension. Range strip selection is enabled by the information provided by the tracking output.
- 4) The target profile is properly filtered to reject the residual background and to enhance the selected target contribution; to this purpose a rectangular window is adaptively defined, based on the selection of a proper threshold to be applied against the current cross-range profile to identify its essential portions.
- 5) Then a reverse focusing is applied to the filtered ISAR profile to recover the current estimate of the target signal in the range-compressed slow-time domain ( $\chi_t^{(p)}[\bar{q}, n] \mid \bar{q} \in Q_t$ ). Specifically this stage includes:
  - an inverse Fourier transform to move from Doppler frequency to slow time domain;
  - the insertion of the range migration that can be achieved by (i) transforming the data in the fast-frequency slow-time domain, (ii) applying a linear phase term depending on  $\hat{a}_1$  (estimated target Doppler centroid), and (iii) inverse Fourier transforming the data back in the range-slow time domain;
  - the insertion of the Doppler migration resulting from the estimated target motion parameters (i.e.  $\hat{a}_i, i > 1$ ).
- 6) Finally, the recovered signal is subtracted from the original surveillance signal to provide the new "target free" version to be exploited at the following iteration:

$$\chi_{tf}^{(p+1)}[q, n] = \begin{cases} \chi[q, n] - \chi_t^{(p)}[q, n] & q \in Q_t \\ \chi[q, n] & q \notin Q_t \end{cases} \quad (38)$$

Notice that, as the target return is better recovered, its contribution to the ECA weights estimation is progressively limited thus reducing its "auto-cancellation" effect. In contrast, the target-free signal can be successfully exploited to estimate the stationary disturbance characteristics so that its removal is kept guaranteed, or even improved, as the algorithm progresses.

The algorithm should be arrested at the time that the signal  $\chi_{tf}^{(p)}[q, n]$  is likely to contain only stationary scatterers contributions (or possibly contributions from other targets). To this aim, a simple stop condition can be defined based on the estimated power level of the target-free signal at the range bins of interest along the whole ISAR CPI:

$$P_{tf}^{(p)} = \sum_{q \in Q_t} \sum_n |\chi_{tf}^{(p+1)}[q, n]|^2 \quad (39)$$

This power level is expected to rapidly decrease at the first iterations where the target main components are easily recovered and subtracted from the available signal, while the reduction of  $P_{tf}^{(p)}$  might become slower as  $p$  grows. Therefore, to limit the required computational load, the algorithm can be stopped when this parameter reaches a desired value (depending on the estimated noise floor) or when its slope is sufficiently flat. However, we have experimentally verified that this parameter usually exhibits a minimum as a function of the iteration number (this will be shown in the next sub-section). Consequently, a reasonable stop condition can be based on the following rule:

$$\Delta^{(p)} = P_{tf}^{(p+1)} - P_{tf}^{(p)} > 0 \quad (40)$$

When such condition holds, the output target Doppler profile is assigned to the last ISAR stage output and, as the final step, undergoes cross-range scaling.

Obviously the enhanced quality of the achieved ISAR profile is paid in terms of an increased computational cost of the iterative technique with respect to the standard one (basically almost coinciding with the first iteration). If we indicate with  $P$  the generic number of iterations needed before reaching the stop condition then the overall computational cost of the iterative technique in principle increases linearly with  $P$ . However it is worth observing that:

- as demonstrated by the results shown in the following, typically few iterations ( $P$  in the order of 10÷20) are needed to reach the stop condition;
- at the  $p$ -th iteration, with  $p \geq 2$ , results from the previous iteration can be suitably exploited in order to limit the selected range strip to the strictly needed range bins (thus limiting the data to be processed) and to initialize the motion estimation techniques (thus requiring not a completely new estimate but a refinement of the previous step).

Based on the two above considerations we can conclude that the increase of the computational cost required by the iterative technique is still manageable and therefore the proposed approach is suitable for application to solve real-world problems.

#### 4.2.2. RESULTS AGAINST SYNTHETIC TARGET ECHOES INJECTED IN REAL STATIONARY BACKGROUND

Aiming at understanding the effect of the cancellation techniques on the ISAR PSF of the system, some controlled tests have been performed. To this purpose an acquisition of duration 6 seconds is considered in the following that contains only the returns from the stationary scene (namely, no targets were employed in this test). The echoes of a fictitious point-like target has been then injected in the collected data.

In particular, with reference to the Figure 16, it is assumed that, during the ISAR CPI of 6 s, the target moves from point  $(x_A, y_A) = (-13.5\text{m}, 50\text{m})$  to point  $(x_B, y_B) = (13.5\text{m}, 50\text{m})$  with constant velocity  $v_x = 4.5$  m/s, distance of minimum approach  $R_0 = 50$  m and  $\text{SNR} = -20$  dB. This particular value of SNR has been chosen since it widely resembles the measurement of the target's RCS previously performed in [35]-[38].

Figure 13(a) shows the Doppler spectrum of the overall signal containing both target and clutter contributions (black curve) compared to the theoretical Doppler spectrum of the target only signal (red curve) which is used as benchmark. The signals are scaled so that the 0 dB level represents the system noise floor. As is apparent a strong component appears at zero Doppler due to the stationary scene; this is

well above the contribution of the fictitious scatterer which yields a rectangular shaped spectrum spanning about 40 Hz around 0 Hz.

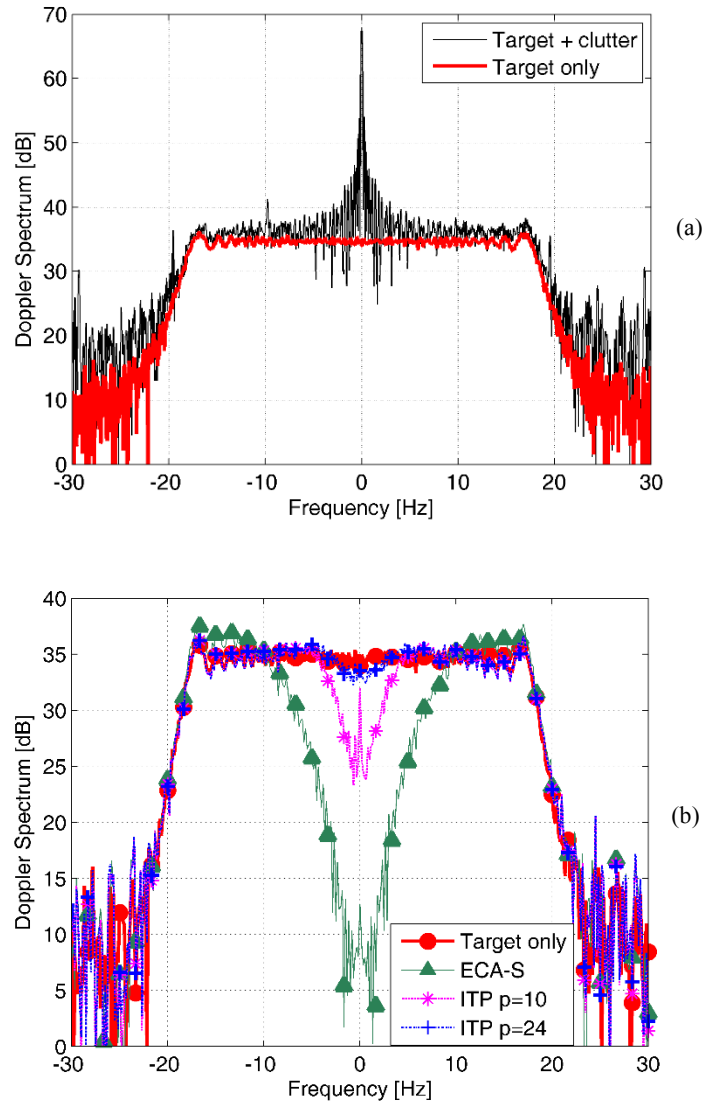


Figure 13. Signal Doppler spectrum: (a) Before disturbance cancellation; (b) After disturbance cancellation using different techniques.

In [38] the strong stationary contribution has been shown to prevent an effective target motion estimation so that the disturbance cancellation stage can be regarded as a necessary step for the successful formation of target cross-range profiles.

Therefore, in Figure 13(b) we report the result obtained after a standard cancellation based on the ECA-S (green curve). As is apparent, the disturbance component is effectively removed. However, as expected, the cancellation filter has dramatically distorted the target spectrum shape at low Doppler frequencies by inserting a cancellation notch. This clearly shows the "auto-cancellation" effect of the target echoes; basically these echoes strongly affect the cancellation filter evaluation as long as the target moves with low radial velocity with respect to the TX/RX so that they are indiscriminately removed together with the stationary scene. Such effect certainly degrades the effectiveness of the subsequent ISAR processing

which needs the entire Doppler frequency history of the target to generate the clairvoyant cross-range profile. Specifically, this yields a corresponding SNR loss that in turn results in a reduced accuracy in the target motion estimation and in a corresponding loss in terms of cross-profile amplitude. Moreover, depending on the portion of the target spectrum that has been cancelled (i.e. central or side part), the above effect might cause severe ambiguities or cross-range resolution degradation.

In the considered case-study, the observed warp of the target spectrum mainly yields an increased sidelobe level in the achievable cross-range profile. This is shown in Figure 14 that reports the cross-range profile obtained for the fictitious target after the application of the conventional ECA-S (green curve) compared to the clairvoyant, target only, profile (red curve) which represents the ideal ISAR PSF of the system. Correspondingly, Table I reports the main characteristics of the obtained cross-range profiles in terms of amplitude loss, cross-range resolution, and peak-to-sidelobe ratio (PSLR). The ECA-S cancellation filter operates over partially overlapped batches ( $T_s = 1 \text{ ms} = \text{PRT}$ ) of 0.1 seconds each, and the filter length  $K$  is set equal to 92, which corresponds to a bistatic range extent of about 500 m at the considered sampling rate. The reported profiles have been obtained by setting  $M=3$ .

As is apparent, the achievable PSLR is 4.17 dB when a conventional ECA-S approach is adopted for disturbance cancellation; this value has to be compared to the theoretical 12 dB obtained in the target-only case (notice that, by limiting the polynomial approximation of the phase history to the third order, uncompensated phase terms of higher orders are accepted that are responsible for a slight PSLR degradation with respect to the 13.26 dB expected for a point-like scatterer in the ideal case). Moreover, a significant amplitude loss is observed since much of the target spectrum has been cancelled by the ECA-S. Finally, it is to be noticed that the slight increase in terms of cross-range resolution is just a misleading effect of the profile warp.

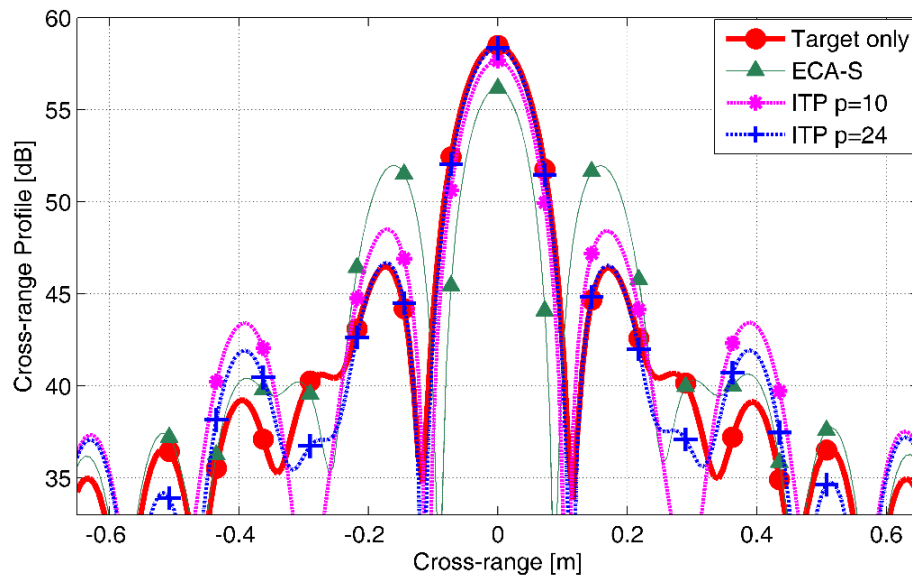


Figure 14. Cross-range profiles for the fictitious target.

Table I. Characteristics of the cross-range profiles obtained for the fictitious target.

|                               | Target only | ITP-based ISAR technique          |             |              |              |              |
|-------------------------------|-------------|-----------------------------------|-------------|--------------|--------------|--------------|
|                               |             | Iter p=1<br>Conventional<br>ECA-S | Iter<br>p=5 | Iter<br>p=10 | Iter<br>p=20 | Iter<br>p=24 |
| <b>Amplitude Loss</b>         | 0 dB        | 2.33 dB                           | 1.35 dB     | 0.82 dB      | 0.27 dB      | 0.14 dB      |
| <b>Cross-Range Resolution</b> | 11.6 cm     | 10 cm                             | 11.6 cm     | 11.6 cm      | 11.6 cm      | 11.6 cm      |
| <b>PSLR</b>                   | 12 dB       | 4.17 dB                           | 7.62 dB     | 9.17 dB      | 11.13 dB     | 11.66 dB     |

The results obtained after the application of the ITP technique are shown in Figure 13(b) and Figure 14 for an increasing number  $p$  of iterations (we recall that the conventional ECA-S coincides with the first iteration of the proposed technique). As is apparent, as  $p$  increases, the target "auto-cancellation" effect is progressively smoothed so that the Doppler spectrum is comparable with the theoretical one (see Figure 13(b)). Correspondingly, the obtained cross-range profile resembles the clairvoyant target-only profile with only small deviations in the low side-lobes region (see Figure 14). This depends on the threshold adopted in the ITP approach to identify the target contribution (in this case 20 dB below the highest target peak) which sets the dynamic range for the recovery of the target signal.

To investigate the reliability of the proposed stop condition, in Figure 15 we show the residual power level  $P_{tf}^{(p)}$  defined in (39) as a function of the iteration number  $p$ .

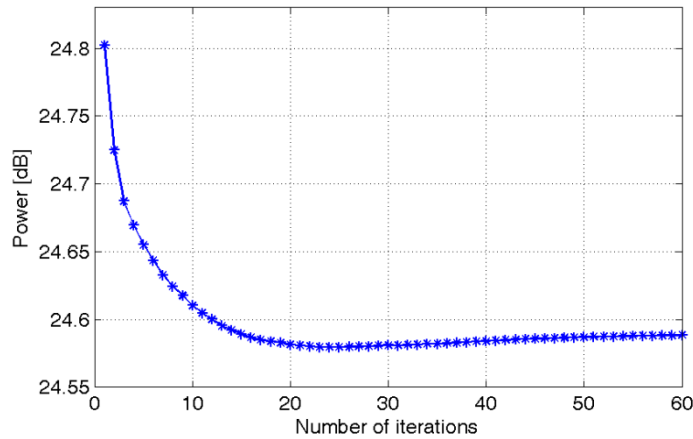


Figure 15. Estimated power level of the target-free signal at the range bin of interest as a function of the iteration number.

As is apparent, the main target contributions are rapidly gathered at the first iterations; however at least 20 iterations are required for the target signal to be better reconstructed. Notice that, as previously mentioned, the reported curve shows a minimum at  $p=24$ . Therefore, the algorithm can be arrested after  $p=24$  iterations since this stage yields the best reconstruction of the target signal. This is also confirmed by the results obtained in terms of cross-range profile and its characteristics (see Table I). In particular, after  $p=24$  iterations, the amplitude loss and the PSLR degradation have been almost totally recovered

and the obtained cross-range profile coincides with the theoretical one in the region encompassing the main lobe and first sidelobes.

### 4.3. EXPERIMENTAL RESULTS AGAINST MOVING MAN-MADE TARGETS

In this sub-section, the performance of the proposed strategy is analyzed against live data and compared to the conventional ECA-S. The considered data set has been collected by means the PBR receiver described in the following. However, aiming at understanding the potentialities of the conceived sensor also for applications of vehicles monitoring and classification, we have been compelled to perform the dedicated test campaigns in outdoor scenarios.

#### 4.3.1. EXPERIMENTAL SET-UP AND ACQUISITION SCENARIO

In this sub-section we introduce our experimental setup and the performed acquisition campaign. The considered data set has been collected by means of the experimental setup sketched in Figure 16.

A portable wireless router was connected to the TX antenna while a directional coupler was used to gather the transmitted signal in a dedicated receiving channel (reference channel). A second receiving channel was connected to a separate receiving (RX) antenna which was used to collect the surveillance signal. The antennas are characterized by a beamwidth of about  $15^\circ$ . The two channels are coherently down-converted to appropriate intermediate frequency of 119 MHz and converted to a digital data stream (sampling frequency of 28 MHz), which is further processed by digital down-conversion and filtering to provide the dual channel I&Q data stream for offline processing.

The router was configured to transmit in channel 1 of the WiFi band (2412 MHz). It was set up to roam for connected devices emitting a regular Beacon signal exploiting a DSSS modulation at 1 ms intervals. Acquisitions of duration of about 10 s overall were performed. Since a dual channel receiver was adopted, data collected by a single passive radar sensor are available so that the results will be shown on the range/velocity plane only.

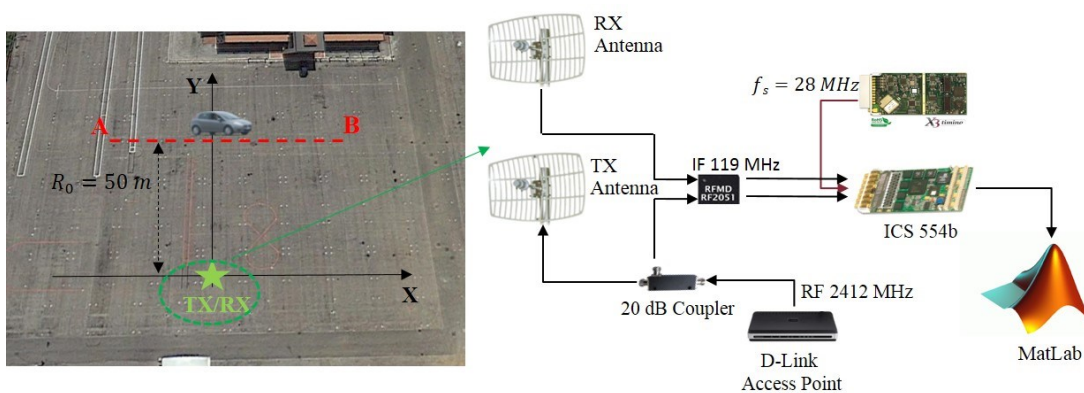


Figure 16. Sketch of the experimental setup and performed tests.

Specifically, the tests were performed in a parking area in front of a private building (see Figure 16 on the left). A single surveillance antenna has been employed, mounted just below the transmitting antenna in a quasi-monostatic configuration. An  $(X,Y)$  coordinate system is defined with the origin in the TX/RX antennas location.

Cars have been used as cooperative targets to demonstrate the practical effectiveness of the proposed approach. Two different tests (M1 and M2) were performed using one or two identical cars (i.e. Fiat Punto Evo) with length of about 4 meters. In both cases the vehicular targets move along the axis  $y=y_0=50$  m (red dashed line in Figure 16) at about  $v_x=4.5$  m/s. Specifically, in test M1, a single car was present approximately crossing the point  $(x_0,y_0)\equiv (0 \text{ m}; 50 \text{ m})$  at the middle of the acquisition. For test M2 a second identical car was employed moving behind the first car with a separation of about 2-3 meters along the x-axis so that, at the middle of the acquisition, they were almost symmetrically displaced about the point  $(0 \text{ m}; 50 \text{ m})$ .

#### 4.3.2. ITP STRATEGY COMPARED WITH ECA

The overall duration of each acquisition is 10 seconds; the results shown in the following have been obtained by using an ISAR CPI set to 6 s properly selected from the whole recording.

Figure 17(a) compares the Doppler spectrum obtained for test M1 in absence of the cancellation stage (black curve), using the conventional ECA-S (green curve), and after the iterative target preserving cancellation approach (blue curve). The latter algorithm has been arrested after 8 iterations according to the proposed stop condition since the power level  $P_{tf}^{(p)}$  defined in (39) exhibits a minimum in  $p=8$  (see Figure 17(b)). Moreover, in this case, the threshold adopted to identify the target contributions based on the current profile has been set experimentally at 13 dB.

As observable from Figure 17(a) the original Doppler spectrum is the sum of the targets contributions and a strong stationary contribution around the zero Doppler. After the application of ECA-S, the disturbance component has been effectively removed but the filter cancellation notch in Doppler dimension has also reduced the target contribution at low frequencies. In contrast, the benefits of the proposed iterative algorithm are clearly visible as it better preserves the target spectral components at low Doppler frequencies while still guaranteeing an effective cancellation of the echoes from the stationary scene. This behavior resembles that shown for the fictitious target in sub-section 4.2.2: obviously in this case a less regularly shaped Doppler spectrum is observed because we are now dealing with a real target instead of the ideal point-like isotropic scatterer.



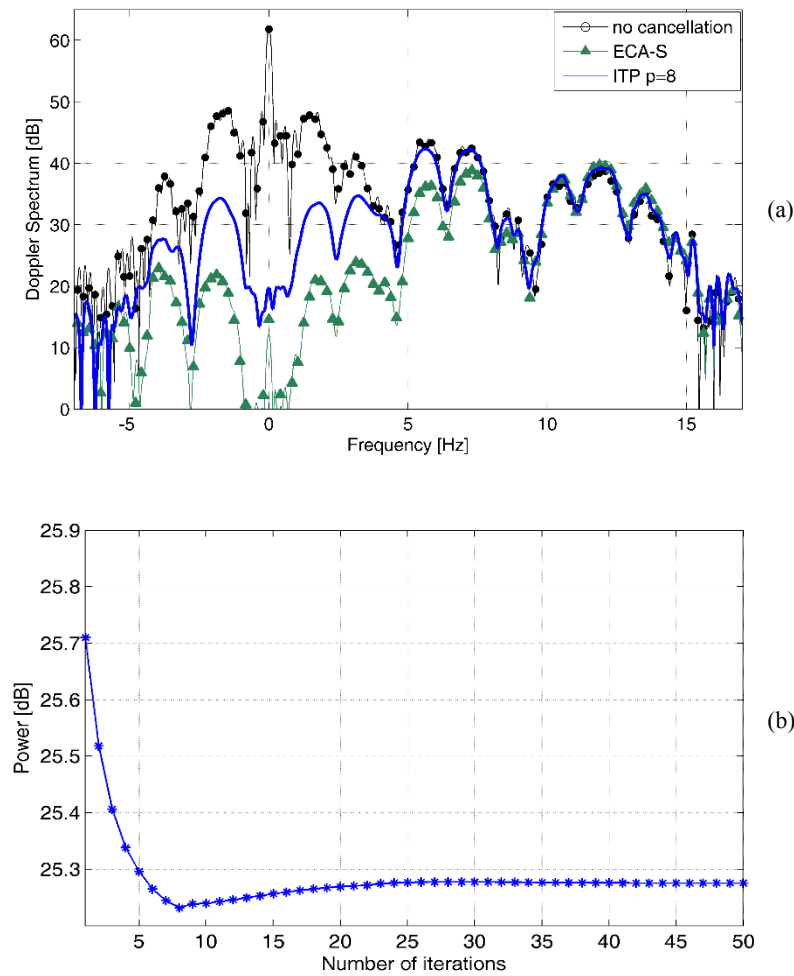


Figure 17. Experiment M1: (a) Signal Doppler spectrum; (b) Residual power level of the target-free signal at the range bin of interest as a function of the iteration number.

The corresponding cross-range profiles are shown in Figure 18(a). We observe that, as for the case of the fictitious target, the newly proposed target preserving strategy yields an improvement of few dBs in terms of profile amplitude. In fact, the capability to preserve a greater portion of the target spectrum has been shown to improve the performance of the subsequent ISAR processing in terms of both target motion estimation and target focusing. This in turn should lead to the formation of more stable profiles to be exploited for the extraction of reliable information on the observed targets. To further demonstrate the reliability of the achieved results, Figure 18(b) shows the cross-range profiles achieved for experiment M2. In this case the ITP algorithm stops after 16 iterations according to the stop condition in (39). As it is apparent, with both the ECA-S and the ITP cancellation approach, the profiles reveal the presence of two similar patterns characterized by three main peaks (labeled with capital letters) which correspond to the main scattering centers of the two identical cars used for the considered experiment.

As an example, in Table II we evaluate the distances between homologous points of the cars (i.e. profile peaks) from the cross-range profiles obtained with the ECA-S and the ITP approaches, respectively. Even if the actual value of this distance is not available, it is expected to be constant independently of the considered pair of peaks. Apparently, the values obtained for the three pairs of peaks are well in line with the test geometry (we recall that the length of each car is 4 meter and their separation along the path is

about 2-3 m); however, for all the three considered pairs, the use of the iterative technique provides less scattered values, when compared to ECA-S, thus proving a more accurate extraction of the target scattering centres by means of ITP technique.

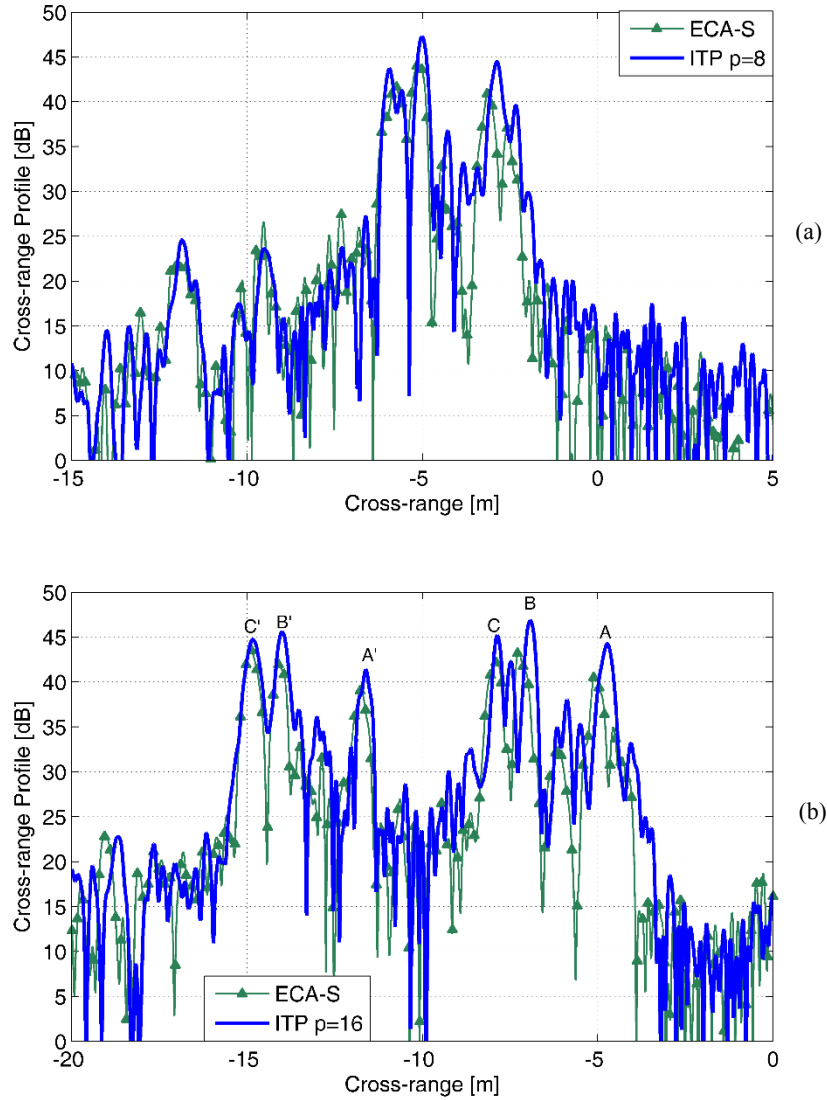


Figure 18. Cross-range profiles comparison for the real data. (a) Experiment M1; (b) Experiment M2.

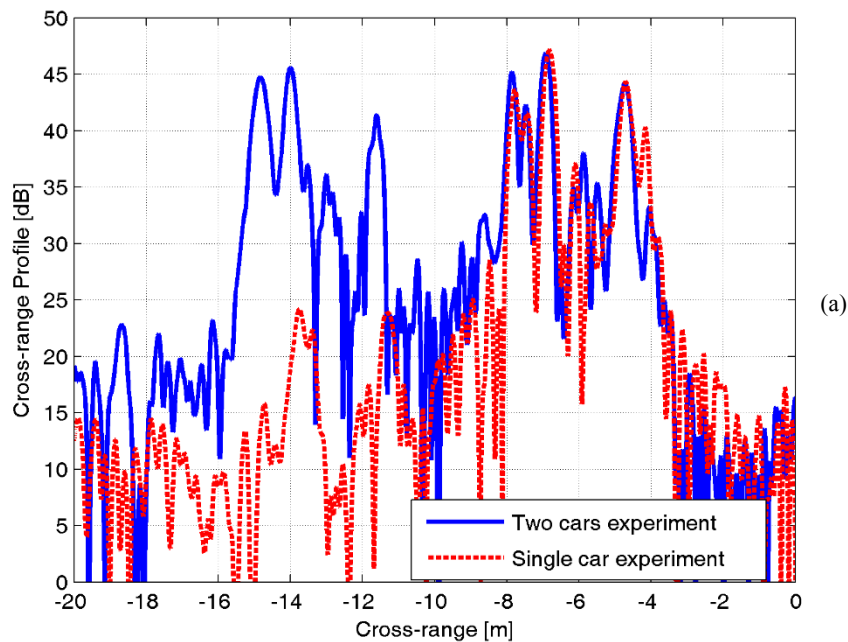
Table II. Cross-range displacements of homologous points of the profiles obtained for test M2.

|                  | ECA-S  | ITP (iter p=16) |
|------------------|--------|-----------------|
| $D_A =  A' - A $ | 6.67 m | 6.88 m          |
| $D_B =  B' - B $ | 6.84 m | 7.08 m          |
| $D_C =  C' - C $ | 7.03 m | 6.97 m          |

To further investigate the reliability of the profiles obtained after the proposed CLEAN-based technique, we compare in Figure 19 the results obtained for test M2 to that of test M1. Specifically, Figure 19(a) and Figure 19(b) have been obtained by exploiting ISAR CPIs of 6 sec temporally displaced along the available acquisitions of 10 sec; moreover, for a convenient comparison, the CPIs adopted for test M1 have been properly selected so as to guarantee that the car was observed from about the same view angle with respect to the leading car of test M2.

Notice that, in both figures, the corresponding cross-range profiles largely overlap, namely almost the same pattern of dominant scatterers is obtained even if different experiments (M1 and M2) are considered. In addition, by comparing Figure 19(a) and Figure 19(b), we might observe that the shape of the profiles has a remarkable temporal stability along the performed acquisition for both test M1 and test M2.

The reported results demonstrate the effectiveness of the proposed experimental setup and processing scheme and support the practical application of the WiFi-based passive ISAR for short range (both indoor/outdoor) surveillance applications. In particular, the comparison above clearly shows the reliability and stability of the achieved profiles which might fruitfully feed a classification stage based on appropriate signatures database.



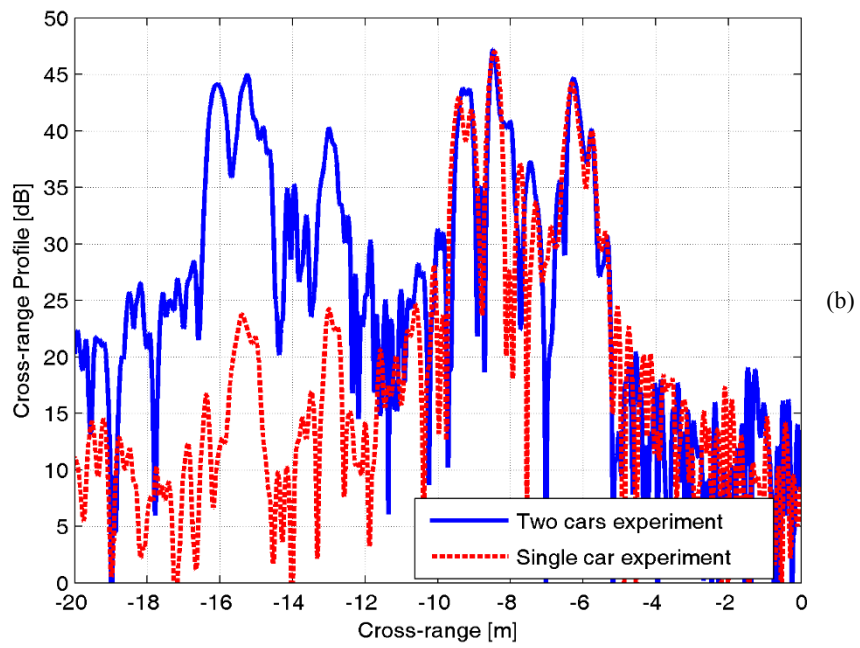


Figure 19. Profiles comparison between test M1 (single car) and test M2 (two cars) for two different selected CPI with ITP technique.

## 5. INDOOR RADAR SURVEILLANCE AGAINST HUMAN TARGETS

The WiFi-based processing scheme depicted in Figure 1 and the processing techniques described in the previous Sections have been mostly demonstrated in outdoor scenarios while few results are available for indoor monitoring.

Therefore, the first objective of this Section is to demonstrate the surveillance capability of WiFi-based PBR in indoor environment. To this purpose, the above techniques are tailored to face the specific challenges of the considered application and validated using real datasets. An experimental setup developed at the University of Rome “La Sapienza” is employed in order to perform different acquisitions against human targets. The reported results prove the actual possibility to detect and accurately track persons moving in realistic indoor environment. However, there are some limitations when the targets move close each other.

For these reasons, the second main goal of this Section is to provide the PBR sensor with the advanced capability to obtain high resolution cross-range profiles of moving targets. This could be an invaluable characteristic in indoor scenarios as it would yield an improved resolving capability to be exploited against the typically high concentration of targets moving in the surveyed scene.

The Section is organized as follow. Sub-section 5.1 describes the real data sets acquired against people walking in a hall and the results are quantified in terms of detection and localization capability of the human targets. In sub-section 5.2, the potentialities of ISAR processing for improved cross-range resolution are demonstrated with reference to human target moving in a cluttered indoor scenario.

### 5.1. TARGET DETECTION AND LOCALIZATION: EXPERIMENTAL RESULTS

In the last years, the research group of DIET Department of the University of Rome “La Sapienza” has been involved in two EU Projects aimed at the demonstration of the effectiveness of WiFi-based PBR sensors for the surveillance of airport terminal areas [45]. In this context, extensive test campaigns have been carried on for different indoor scenarios using cooperative human targets.

The passive radar prototype developed at the DIET Department of the University of Rome “La Sapienza” has been employed [81]. It consists of four receiving channels providing a fully coherent base-band down-conversion of the input signals; these are then synchronously sampled at 22 MHz and stored for off-line processing.

In this work we report the results obtained against the data collected with the experimental setup depicted in Figure 20. The PBR receiver has been fielded in a wide exhibition hall of the “Nuova Fiera di Roma” whose size is comparable with an airport’s terminal. In particular, the exhibition hall is approximately 77 meters wide and 120 meters long (see Figure 20). An (X,Y) coordinate system has been defined with the X axis aligned with the short side of the hall and the Y axis oriented toward its center, being the origin of the system located on the TX antenna.

A commercial WiFi AP was used as transmitter of opportunity. Its output was connected to the transmitting antenna while a directional coupler was used to send a -20 dB copy of the transmitted signal (the reference signal) to the first receiving channel of the quad-channel PBR receiver. Two surveillance antennas (RX 1 and RX 2) were employed, aligned along the X direction at a distance of 12 cm which gives a 45° ambiguity for the target DoA estimation. The transmitting antenna was mounted at a height of

about 2 meters from ground while the two receiving antennas were placed about 40 cm below, in a quasi-monostatic configuration, and steered toward the positive Y axis. All the antennas are commercial WiFi panel antennas and are characterized by a gain of 12 dBi, a front-to-back ratio of 15 dB and beamwidths equal to about  $80^\circ$  and  $23^\circ$  on the horizontal and the vertical plane, respectively.

The router was configured to transmit in channel 1 of the WiFi band (2412 MHz). It was set up to roam for connected devices emitting a regular Beacon signal exploiting a DSSS modulation at 3 ms intervals.

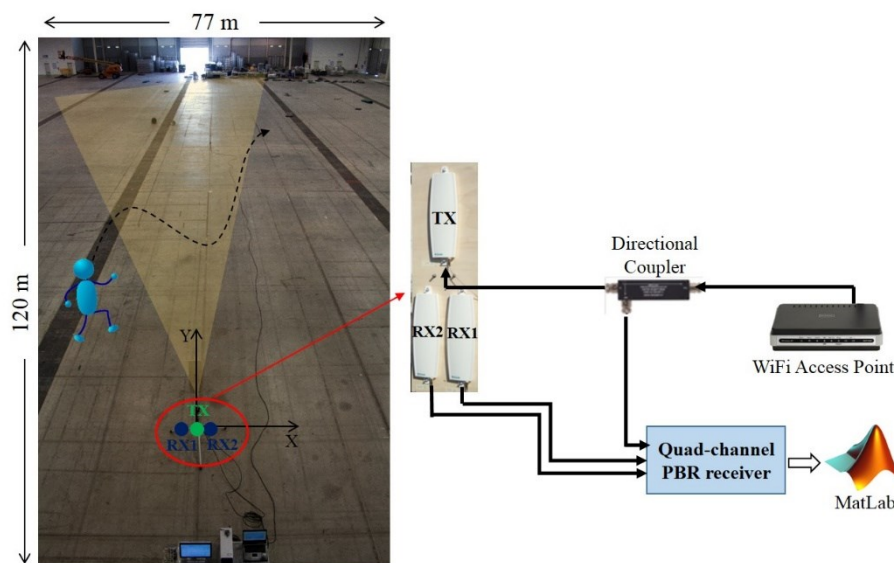
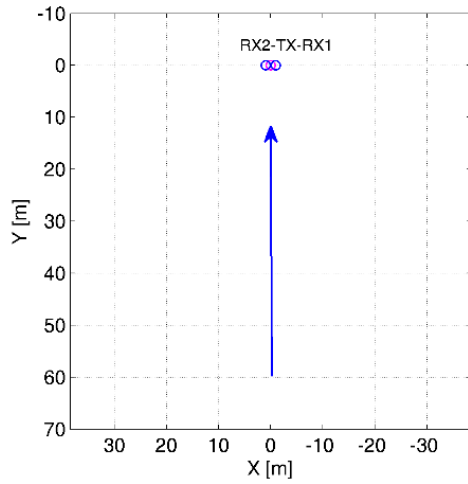


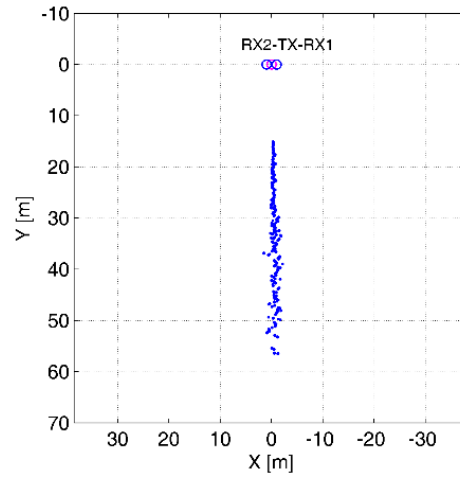
Figure 20. Sketch of the experimental setup and indoor scenario.

About 60 different tests have been performed using one or two human targets walking simultaneously in the area to be surveyed. In the following, for illustrative purposes, we will report the results of the three tests described below:

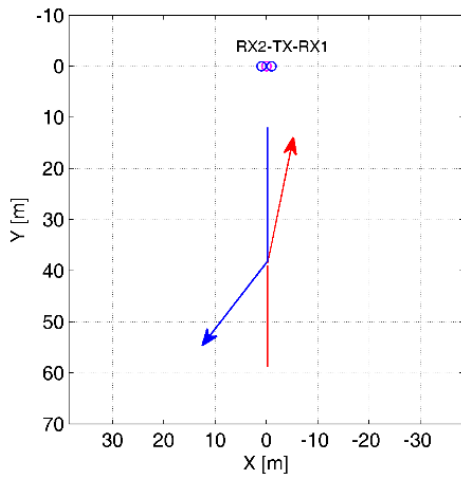
- test T1 [Figure 21(a)]: a man moves toward the transmitter of opportunity with roughly constant velocity along the Y axis (i.e. DoA equal to zero degrees);
- test T2 [Figure 21(b)]: two men walk along crossing paths. In particular, they initially move closer together; once they have come across, they contemporaneously change they walking directions departing from the Y axis with different angles;
- test T3 [Figure 21(c)]: two men move along partially overlapping paths. In particular, they initially walk on the same direction with a constant separation of about 1 m; then they abruptly change their heading, going towards opposite sides of the hall.



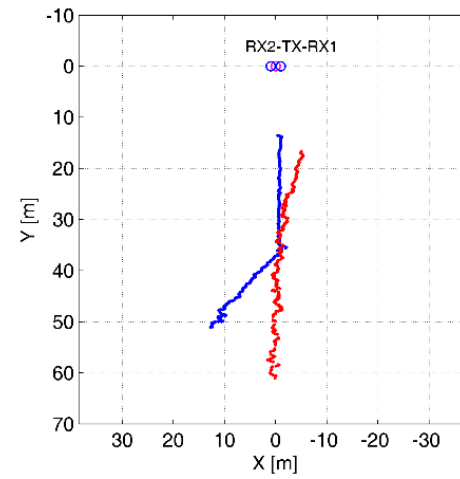
(a)



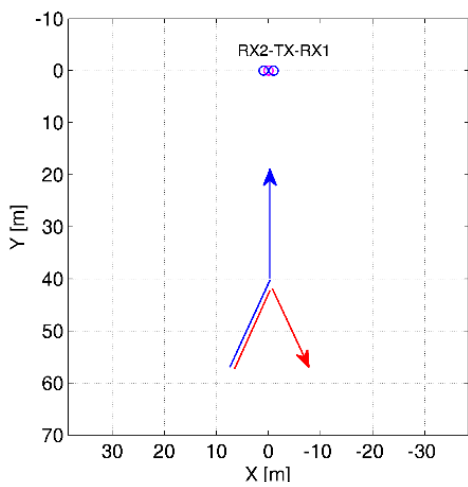
(d)



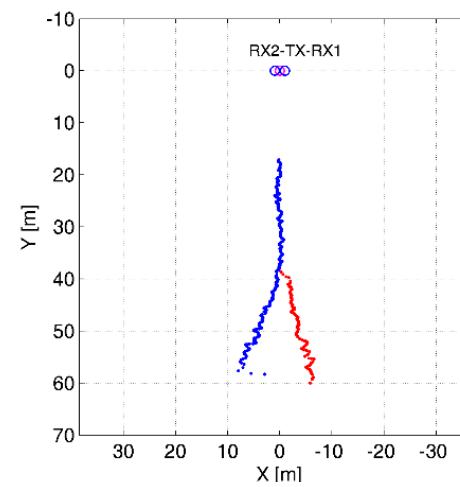
(b)



(e)



(c)



(f)

Figure 21. Real target trajectories for (a) Test T1; (b) Test T2; and (c) Test T3. PBR localization results for (d) Test T1; (e) Test T2; and (f) Test T3.



The data collected for each test covers a length of time equal to 25 sec and each surveillance signal has been processed according to the WiFi-based passive radar processing scheme of Figure 22 paying special attention to the adjustments made to guarantee their effectiveness in the considered indoor application. In particular, notice that for the indoor application, the ECA-S filter (K) can be limited to few tenths of taps since the equivalent path length of the main multipath contributions is expected to not exceed few hundreds of meters. In addition, the batch duration  $T_B$  or  $T_A$  (respectively for ECA-B or ECA-S), has to be carefully selected as it determines the signal fragment over which the filter weights are estimated so that it affects the capability to adapt to the varying characteristics of the environment. As mentioned in the previous Sections, reducing the batch duration widens the filter cancellation notch in the Doppler dimension, so that it should be traded with the minimum target detectable velocity to be guaranteed. In conclusion, for the considered application, the ECA-S is applied with a batch duration  $T_A = 100$  ms and  $T_S = 3$  ms (we set the filter update rate to be equal to the beacon emission rate of the exploited AP) over a range of 300 m. Then, a CPI of 0.5 s is used to evaluate the bistatic range-velocity map over consecutive portions of the acquired signals (frames) with a fixed displacement of 0.1 s (10 frames per second are thus obtained); and target detection is performed by resorting to a standard cell-average CFAR threshold with a probability of false alarm equal to  $10^{-4}$ .

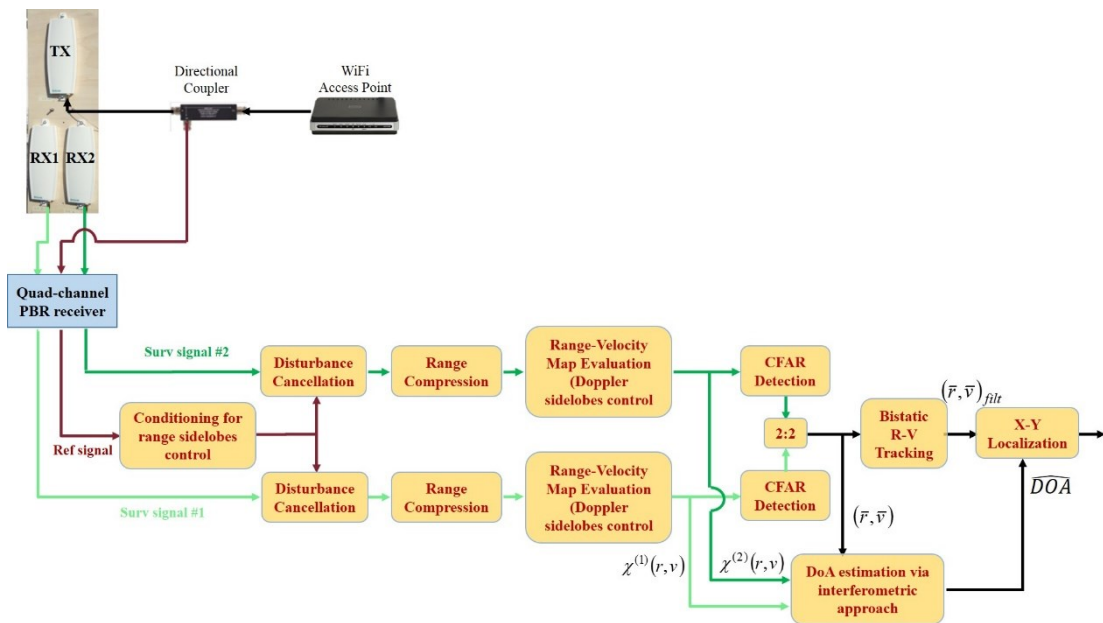


Figure 22. WiFi-based processing scheme for target localization.

As an example, in Figure 23(a) we report, on the same range/velocity plane, the raw detections collected along the whole acquisition (25 seconds) for test T1 (black ‘×’ markers). As is apparent different kinds of detections can occur that might be classified as follows:

- (i) Detections which are likely to correspond to the target returns as they are compliant with the test geometry. It is worth noticing that such detections spread over the velocity dimension; this can be reasonably related to the motion of the legs and arms of the human body that induce Doppler modulations around the main target Doppler shift (micro-Doppler effect).

- (ii) Detections resulting from the multipath effect caused by reflections of the target echo over either the walls or the ceiling of the hall; in fact they draw a range/velocity trajectory that can be predicted based on the real target trajectory by applying geometrical optics rules.
- (iii) Spurious Doppler peaks due to the PBR receiver non-idealities. These are responsible for detections appearing for all the performed tests at constant velocity and very short ranges.
- (iv) False alarms due thermal noise and disturbance residuals; in this specific case, few false alarms arise thanks to the '2-out-of-2' criterion adopted to integrate the detection results separately obtained at the two surveillance channels. Anyway isolated false alarms might be easily discarded by a tracking algorithm.

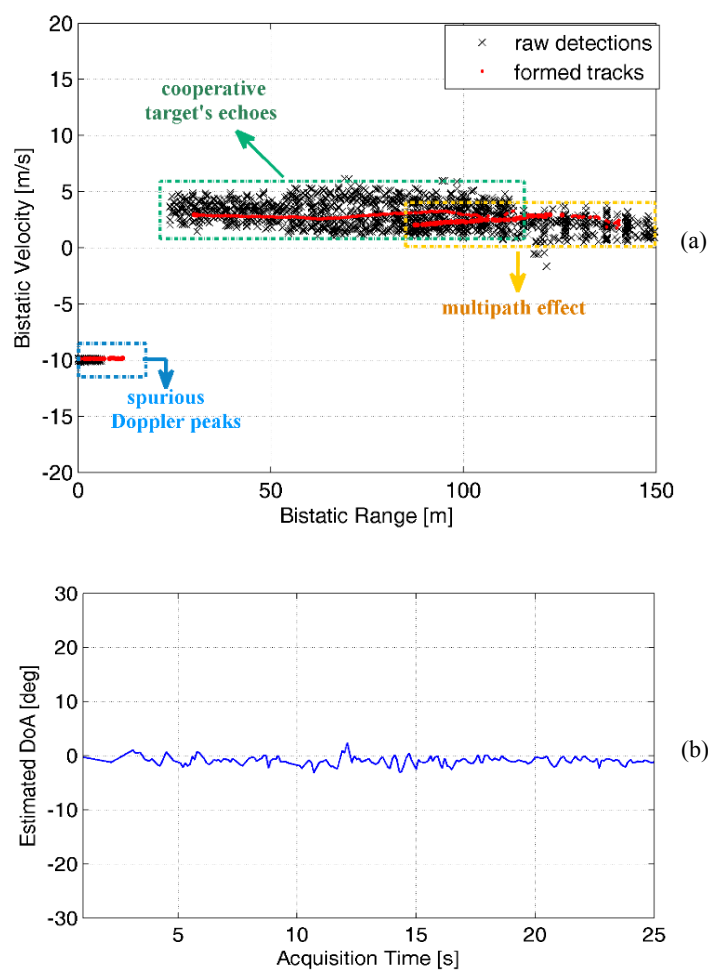


Figure 23. Target detection and DoA estimation results for test T1. (a) Plots and tracks over the range/velocity plane. (b) Estimated target DoA vs time.

The output of a conventional Kalman tracking algorithm operating over the range-velocity plane is also reported in Figure 23(a) (red circles). The plot association stage exploits a nearest neighbour approach that follows a careful selection of the raw detections. In fact, while the analysis of the complex target micro-Doppler signature might be useful if target recognition is required, for the purpose of our analysis, the raw detections arising from this effect are properly discarded by retaining a single detection for each range cell where the CFAR threshold has been exceeded.

The phase difference  $\Delta\phi$  between the range/velocity maps obtained for RX 1 and RX 2, taken at the target detection point, is then exploited to obtain the target DoA estimation as follow:

$$\widehat{DOA} = \sin^{-1}\left(\frac{\Delta\phi\lambda}{2\pi d}\right) \quad (41)$$

where  $d=12$  cm is the distance of the surveillance antennas (see Figure 20). The estimated target DoA along the performed acquisition is shown in Figure 23(b) for the longest track identified on the range/velocity plane in Figure 23(a). As is apparent, the reported result is well in line with the test T1 geometry as the target moves along the Y axis.

Finally, by jointly exploiting bistatic range and DoA measurements, target 2D localization is obtained using the approach described in [36]. The result obtained for the target of test T1 is reported in Figure 21(d). Correspondingly, Figure 21(e)-(f) report the X-Y output for tests T2 and T3, respectively.

As is apparent, in all cases, only small deviations are observed with respect to the real targets trajectory [see Figure 21(a)-(c)]; these are mainly due to the target range/DoA estimation accuracies and their projection on the X-Y plane. Anyway, better results are expected by exploiting multiple PBR sensors properly dislocated around the hall [36]; moreover the achievable positioning accuracy can be increased by applying a second tracking stage on the Cartesian plane.

With reference to the experimental tests involving two targets (i.e. T2 and T3), we observe that the conceived system is able to correctly identify and track the two men moving in the hall as far as they can be distinguished in the range/velocity plane; in particular, when the targets move towards opposite directions they yield echoes with opposite Doppler frequencies [see Figure 21(b)-(e)].

In contrast, in test T3, only a single target is recognized and tracked in the first part of the acquisition as the two men walk close each other [see Figure 21(c)-(f)]. Obviously, this is a consequence of the limited resolution provided by the WiFi-based PBR, especially in the range dimension. Therefore, whereas the above results clearly show the promising characteristics of the conceived sensor for indoor target localization and tracking in surveillance applications, it is of great interest the study of alternative processing techniques able to provide an improved resolution capability on the observed targets, along the line investigated in [38] and in Section 4.

---

## 5.2. ISAR TECHNIQUES FOR IMPROVED CROSS-RANGE RESOLUTION

As is well known, the WiFi-based passive radar guarantees equivalent monostatic range resolution of tens of meters. Additional resolution in cross-range direction could be achieved by coherently processing the returns from the target of interest when observed at different aspect angles. Particularly in ISAR the angular aperture needed to this purpose is obtained by exploiting the motion of the target itself, [64]. Therefore, in [38] and in Section 4 we have shown that a cross-range resolution considerably higher than the range resolution can be achieved by applying ISAR techniques to targets with a motion component in the cross-range direction.

Obviously different applications impose different constraints and requirements on the quality of the ISAR products so that this potential degradation might be appreciable or not. Particularly when considering man-made targets (such as vehicles), the requirement is on the accurate separation and extraction of the different scattering centres of the same target so that ATR (Automatic Target Recognition) procedures could be enabled. In contrast, when dealing with human targets the strong requirement is on the resolution

capability enabling the separation of the different targets. While enhanced quality products are essential for classification purposes, standard quality ISAR products can allow the separation of different targets.

Potential of ISAR techniques in resolving closely spaced human targets moving in a cluttered indoor scenario is here demonstrated by using live data acquired by means of the PBR receiver described in the previous sub-section and reported in Figure 24. The PBR receiver has been fielded in the canteen of the School of Engineering at University of Rome “La Sapienza” whose size is approximately equal 11 meters wide and 28 meters long (Figure 25). An (X,Y) reference system has been defined similarly to that in Figure 20. Tests have been performed using two human targets about 2 meters apart moving in cross-range direction (i.e. trajectory parallel to X axis) with approximate speed 1.3 m/s, distance of minimum approach  $R_0=24.4$  m and overall test duration equal 10 sec.

The acquired data has been processed via the whole processing scheme in Figure 1 with ECA-S applied with a batch duration  $T_A = 400$  ms and  $T_S = 3$  ms (we set the filter update rate to be equal to the beacon emission rate of the exploited AP) over a range of 300 m. Moreover, the bistatic range-Doppler map is evaluated over a CPI of 0.5 s.

As an example, Figure 26 shows the range-Doppler map after disturbance cancellation and sidelobe control in the range and Doppler dimensions. We note as the targets appears as a strong peak in the map at about 54 m and 2.4 Hz. Moreover, additional peaks are present at further ranges and Doppler due to the multiple signal bounce against the room’s wall. Therefore, the two targets give rise to the presence of a single peak meaning that the two targets can be detected but not resolved; this is due to the fact that in this case the separation between the two persons is lower than the system resolution, as a consequence the two persons appear as a single peak in the evaluated map.

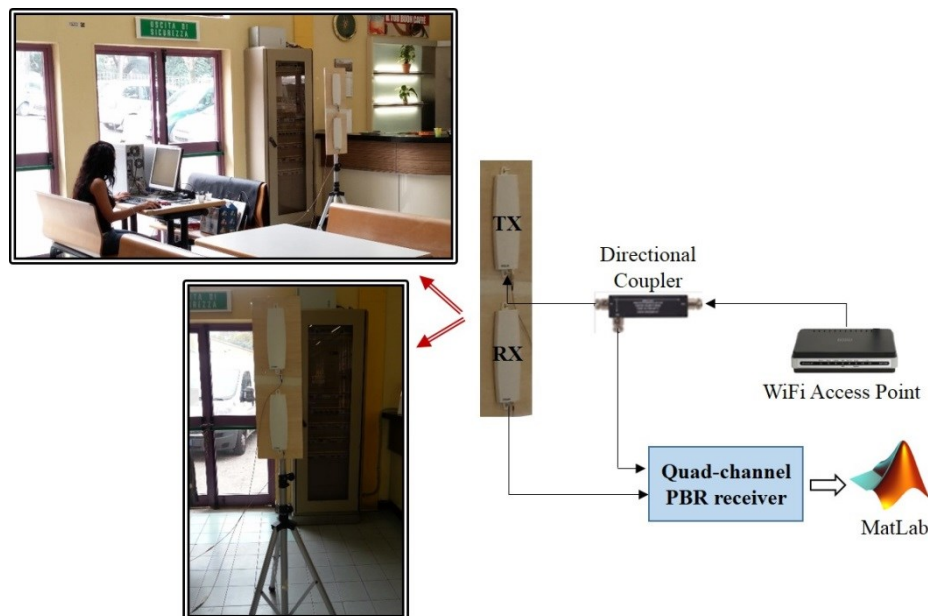


Figure 24. Sketch of the experimental setup.



Figure 25. Sketch of the acquisition geometry.

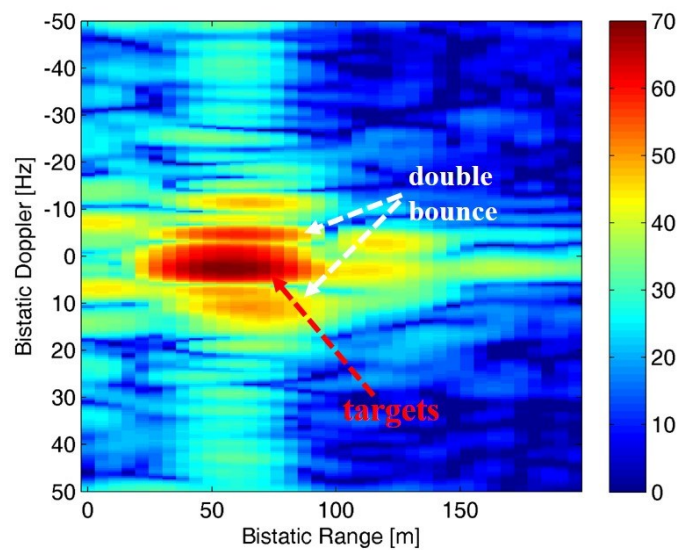


Figure 26. Range-Doppler map.

Obviously, for security applications, like that foreseen by the ATOM and SOS projects that aims to jointly employ the WiFi PBR sensor with other active and passive radar sensors to enhance the security level in the airport terminal area, this represents a limitation.

For these reasons, ISAR techniques have been applied in the next sub-section to obtain additional resolution in cross-range direction by coherently processing the returns from the target of interest when observed at different aspect angles.

However, due to the presence of the multiple signal bounces, the range compressed data can't go directly in input to the basic ISAR processing scheme described in Figure 1. For these reasons, once a moving target has been detected, the range compressed data has been filtered in the Doppler bandwidth of interest and then the corresponding range strip is selected and fed in input to the ISAR processing block



constituted by the cascade of target motion estimation, cross-range profile focusing and scaling as shown in Figure 1.

In our case, for the considered short-range acquisition geometry depicted in Figure 25 and for the motion conditions, it is sufficient to set  $M = 3$  by considering an ISAR CPI of 3 s.

A cut of the bistatic range-Doppler map at the range bin interested by the two human targets is reported in Figure 27 (blue curve). As previously shown in Figure 26 we can observe that the two targets give rise to the presence of a single strong peak meaning that the two targets can be detected but not resolved. By increasing the coherent processing interval and feeding the ISAR processing block the red curve in Figure 27 is obtained. We observe that the increased CPI provides an improvement in terms of both Doppler resolution and target peak power. Particularly, the two targets give rise to the presence of two clearly resolved peaks.

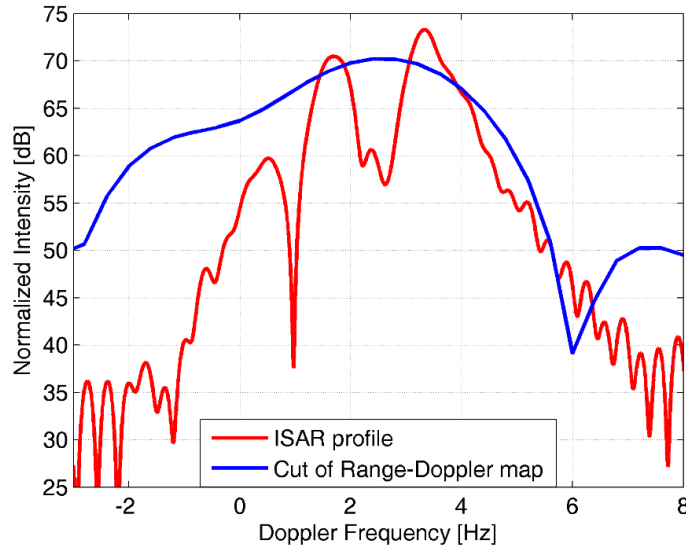


Figure 27. Cut of the Range-Doppler map (CPI=0.5 sec) and ISAR profile (CPI=3 sec) comparison.

Figure 28 shows the cut of the entropy cost function as a function of the  $\alpha_2$  parameter. As is apparent, the entropy curve shows a marked minimum in correspondence of  $\hat{\alpha}_2 = 0.069 \text{ m/s}^2$ . Once the  $\hat{\alpha}_2$  value is known, also the cross-range velocity can be obtained as  $\hat{v}_{cr} = \sqrt{\hat{\alpha}_2 R_0} = \sqrt{0.069 \cdot 24.4} = 1.2975 \text{ m/s}$ , [38]. Notice that such value of  $\hat{v}_{cr}$  is well in line with the considered test geometry. Finally,  $\hat{v}_{cr}$  is directly used to scale the Doppler axis thus mapping Doppler frequencies into cross-range distances and the corresponding cross-range profiles is reported in Figure 29. We note as the cross-range separation of the two peaks is about 1.85 m which is largely in agreement with the actual separation between the targets.

The reported results clearly show that the motion of the targets can be fruitfully exploited to improve cross-range resolution so that closely spaced targets can be effectively discriminated whereas they could not be resolved by a conventional processing. In particular, the obtainable cross-range resolution  $r_{cr}$  is:

$$r_{cr} = \frac{\hat{v}_{cr}}{B_D} \quad \text{with} \quad B_D = \frac{2}{\lambda} \hat{\alpha}_2 T_{ISAR} \quad (42)$$

where  $B_D$  is the Doppler bandwidth whereas  $T_{ISAR}$  is the ISAR CPI. For the considered case, the obtainable cross-range resolution is about 37 cm.

Therefore, a cross-range resolution considerably higher than the range resolution can be achieved by applying ISAR techniques. Moreover the characteristics of the considered indoor scenario demonstrates the potential of the proposed approach in cases of practical interest.

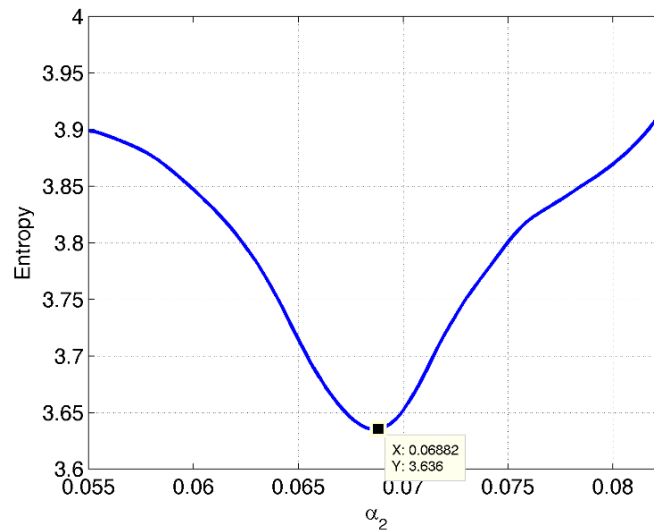


Figure 28. Entropy cost function versus  $\alpha_2$  parameter.

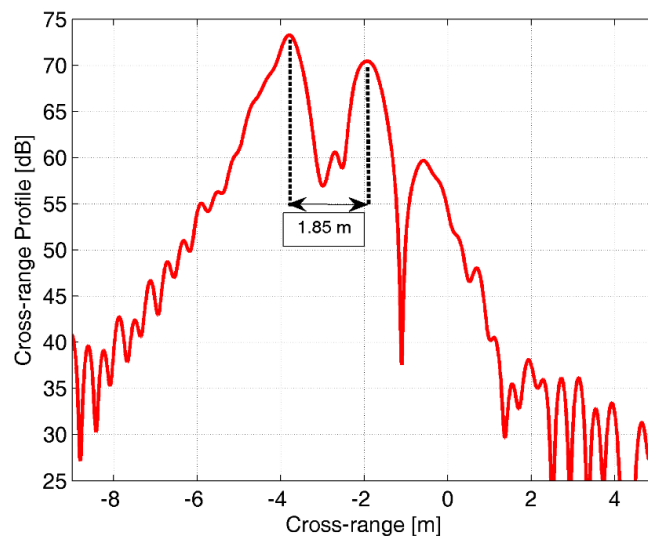


Figure 29. Cross-range profile.





## 6. SMALL PRIVATE AIRPORTS SURVEILLANCE

In this Section, the potential exploitation of WiFi-based PBR systems is investigated with reference to a real-world civil application where these sensors are expected to nicely complement the existing technologies adopted for monitoring purposes, especially when operating against non-cooperative targets.

In particular, we consider the monitoring application of small private airstrips or airfields. With this terminology, we refer to open areas designated for the taking-off and landing of small aircrafts, but which, unlike an airport, have generally short and possibly unpaved runways (e.g. grass, dirt, sand, or gravel surfaces) and do not necessarily have terminals. More important, such areas usually are devoid of conventional technologies, equipment, or procedures adopted to guarantee safety and security in large aerodromes.

The study has been conducted within the SOS project which intends to develop a non-intrusive and pervasive surveillance system for airport and air transport security, based on an innovative combination of passive and active radar sensors operating at various frequency bands, [45]. In this work, we report the results obtained in a test campaign performed in a small private airfield for light/ultralight airplanes by simultaneously employing the WiFi-based passive radar prototype developed at University of Rome “La Sapienza”, [81], and a Ku-band FMCW radar developed by MetaSensing [82]. Aircrafts, cars, and people have been employed as targets of opportunity to simulate different operative conditions of interest.

The results obtained with the conceived sensor support the practical applicability of the WiFi-based passive radar concept for improving safety and security of small private airfields and demonstrate its suitability to be usefully employed in such scenarios in the near future.

The paper is organized as follows. The proposed application is discussed in sub-section 6.1 where the main challenges and typical operative conditions are identified. sub-section 6.2 illustrates the performed test campaign, the experimental PBR receiver set-up, and the signal processing steps adopted for the results reported in this work. The results obtained in different experimental tests with the WiFi-based PBR system are reported in sub-section 6.3.

### 6.1. ULTRALIGHT AIRFIELDS MONITORING APPLICATION

There exist a huge number of small, privately owned and unlicensed airfields around the world. Private aircraft owners mainly use these “airports” for recreational, single-person or private flights for small groups and training flight purposes. In addition, residential airparks have proliferated in recent years, especially in the US, Canada, and South Africa. A residential airpark, or “fly-in community”, features common airstrips where homes with attached hangars allow owners to taxi from their hangar to a shared runway. In many cases, roads are dual-use for both, cars and planes, [83].

As previously mentioned, ultralight airfields, small private runways, and even airparks, are usually devoid of conventional technologies adopted to guarantee safety and security in large aerodromes, there including navigation aids, signs and lighting. The use of the runways is usually limited to the daylight hours and mostly controlled by dedicated operators equipped with radio transceivers in the HF/VHF band to communicate with the pilots of the aircrafts. These are expected to be cooperative, expert, and well-intentioned users, and to adhere to basic procedures during landing/taking off, taxiing, etc. The operator visually verifies that the runway is empty before authorizing an interested user to occupy it.

Depending on the length of the runways and visibility conditions, several operators might be required to monitor the whole area of interest in order to avoid runway incursions by other aircrafts, vehicles, people, and even animals. In this regard, it is worth mentioning that many of the considered “small airports” are rarely enclosed in a monitored perimeter (e.g. barrier, fencing, etc.) and the edges between runways and taxiways are not clearly indicated. Therefore, it is possible that vehicles or beings intrude onto the runways either intentionally or accidentally. In addition, it would be desirable to monitor the airstrips and neighboring zones also when they are not being used by conventional users (i.e. night-hours, closing times, etc.) in order to avoid an illicit use by ill-intentioned persons.

A pictorial view of the considered scenario is reported in Figure 30. The figure sketches both the conventional activities and possible hazards related to different users of the airstrips, either allowed or not-permitted.

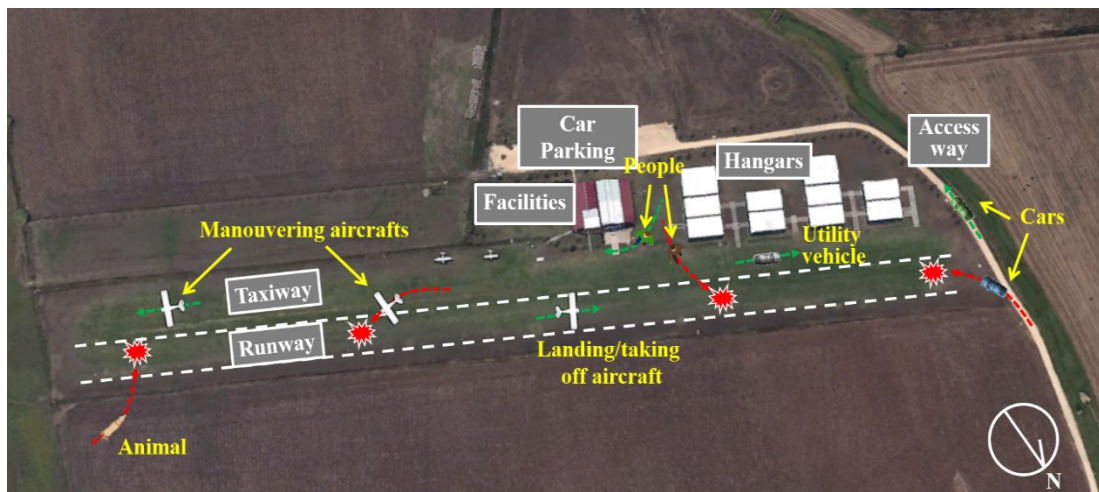


Figure 30. Scenarios of potential interest in small private airfield monitoring application.

As is apparent, there is substantial scope for an improvement in situational awareness in such scenario. In particular, the probability of accidents could be significantly reduced if an automatic control is implemented on the activities that occur on the runway and in neighboring zones.

To this purpose, it would be of great potential interest the possibility to employ low-cost, compact, non-intrusive, and non-transmitting sensors as a way to improve safety and security with limited impact on the airstrips users. Specifically the opportunistic exploitation of transmissions for networking (WiFi, WiMAX, LTE, etc.) is especially attractive since they have been proliferating at a very rapid rate for both commercial and private use and nowadays represent a widely accessible source of opportunity.

Among them, the IEEE 802.11 Standard based (WiFi) transmissions seem to be an appropriate choice in the considered scenarios. Basically, even though they do not feature real terminals, airstrips owners eventually began to offer services and facilities to its users. These typically include the WiFi connection that sometimes is also adopted for pre-flight briefing. Based on the passive radar principle, the same WiFi AP might be exploited to provide the required radar surveillance capability in the area of interest. Notice that the requirement for a continuous coverage of the airfield might result in a suitable number of passive receivers to be deployed along the runways and neighbouring zones.

According to the considerations above, in the following we investigate the performance of a WiFi-based PBR sensor in small private airfield monitoring application. The aim is to assess the capability to detect, localize and track authorized/unauthorized targets that can be occupying the runway and the surrounding areas.

## 6.2. ACQUISITION CAMPAIGN AND SET-UP

We report the results obtained in the test campaign performed in a small airfield named “Aviosuperficie Monti della Tolfa” [84] located in Santa Severa (about 60km North of Rome). Figure 30 reports an aerial view of the airfield area. The airfield is only used for recreational and training flight purposes. It features a single runway, 520 meters long and 20 meters wide, with a grass surface. Depending on wind direction, take-offs and landings are performed with heading  $120^\circ$  or  $300^\circ$  w.r.t. North. A dedicated operator is in charge of the control of the traffic on the runway and neighboring areas.

In the performed test campaign, we employed the same experimental PBR quad-channel receiver developed at the University of Rome "La Sapienza" described in Section 5, [81]. The router WiFi was configured to transmit in channel 7 of the WiFi band (2442 MHz). It was set up to roam for connected devices emitting a regular Beacon signal exploiting a DSSS modulation at 3 ms intervals. Other two rx channels are connected to commercial WiFi panel antennas to collect the surveillance signals; the employed antennas are characterized by a gain of 12 dBi, a front-to-back ratio of 15 dB and beamwidths equal to about  $80^\circ$  and  $23^\circ$  on the horizontal and the vertical plane, respectively. The surveillance antennas (see Figure 31) were mounted at a height of about 1.6 meters from ground, about 40 cm below the transmitting antenna, in a quasi-monostatic configuration, and they were pointed at  $345^\circ$  w.r.t. North. Moreover, they were displaced in the horizontal direction by 12 cm, which gives a  $45^\circ$  ambiguity for the target DoA estimation, based on an interferometric approach.

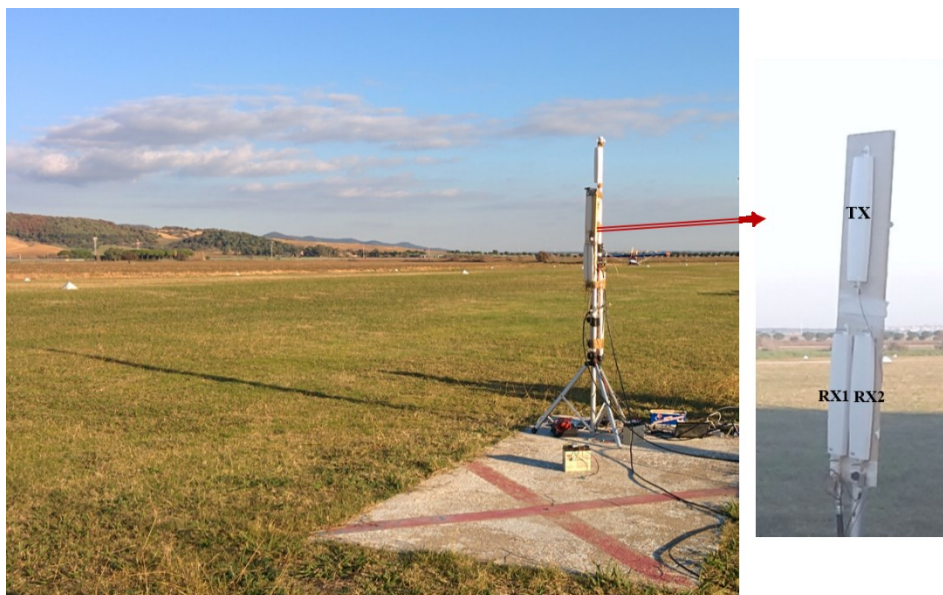


Figure 31. Sketch of the antennas displacement.

Each surveillance signal separately undergoes the signal processing stages illustrated in Figure 22. In particular, the removal of undesired contributions is performed with the sliding version of the extensive cancellation algorithm (ECA-S) over a range of 600 m with a batch duration equal to 0.2 s whereas the filter update rate is equal to the beacon emission rate of the exploited AP. A CPI of 0.3 s is then used to evaluate the bistatic range-velocity map over consecutive portions of the acquired signals with a fixed displacement of 0.1 s and target detection is performed by resorting to a standard cell-average CFAR threshold with probability of false alarm equal to  $10^{-4}$ . Then, a two-out-of-two detection criterion is adopted for the two surveillance channels which allows to collect a set of bistatic range and Doppler frequency measurements and to reduce the number of false alarms.

As an example, for the case of an test with two targets which will be shown in the next sub-Section (Figure 34), in Figure 32 are reported in 'x' markers all the plot collected over the whole acquisition time. In order to reduce the false alarms while yielding more accurate range/velocity measurements, a conventional Kalman tracking algorithm over the bistatic range/velocity plane has been applied. Specifically, in Figure 32 the sequence of green and blue dotted markers represents the first and the second formed tracks, respectively. We observe the above processing scheme allows to continuously detected and accurately tracked both targets although they have different velocities. Finally, the phase difference between the two receivers measured at the target detection point is exploited to obtain the target DOA estimation. In fact, target 2D localization in local Cartesian coordinates can be obtained by exploiting the range and DOA measurements provided by the two horizontally displaced surveillance antennas [36].

Several tests have been performed against different targets of interest aiming at assessing the suitability of the conceived system with reference to typical operative conditions. Some examples are reported in the following sub-section.

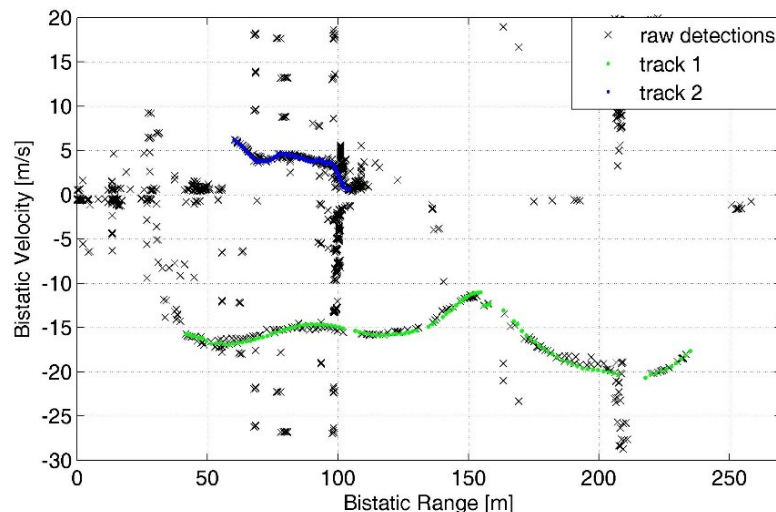


Figure 32. Detection over the Range-velocity plane for the test in Figure 34.

### 6.3. RESULTS AGAINST EXPERIMENTAL DATA

The experimental results reported in this sub-section refer to the following test types:

- Test A: small aircrafts moving on the runway for landing/taking-off;



- Test B: small aircrafts maneuvering in different areas of the airfield;
- Test C: vehicles moving in the proximities of the runway/taxiway;
- Test D: people walking around the airfield.

Different tests are addressed in the subsequent dedicated sub-sub-Sections.

### 6.3.1. TEST AGAINST A LANDING AIRCRAFT

The first test employed a small aircraft as a cooperative target [see Figure 33(a)], equipped with a GPS receiver that continuously recorded its position [green markers in Figure 33(b)]. The WiFi-based PBR receiver performed a 20 s registration; during this period the aircraft moved on the runway just after landing, travelling a distance of about 110 meters, away from the receiver location. The position and the main beam angular coverage of the PBR antennas is sketched in yellow in Figure 33(b).

The results obtained after the basic processing stages illustrated above are reported in Figure 33(b) as red markers. The good agreement with the available ground-truth demonstrates the capability of the PBR system to monitor conventional activities occurring on the runway. In fact the small aircraft is continuously detected along its trajectory and its position is estimated with good accuracy at least when it is included in the receiver antennas beamwidth. For the most part of the target trajectory, the positioning errors are largely comparable with the target size. As expected the target localization accuracy rapidly degrades as the aircraft gets far away from the PBR receiver; basically this is due to the decrease in the target echo power level and to the widening of the uncertainty x-y area caused by a given DoA error.

In addition, Figure 33(c) reports the localization results of the same aircraft just after a different landing; we observe again a good agreement with the available ground-truth.

Obviously, better results could be obtained by applying a second tracking stage over the x-y plane and/or jointly exploiting the range and angle measurements provided by multiple PBR sensors properly dislocated on the area to be surveyed, [36].



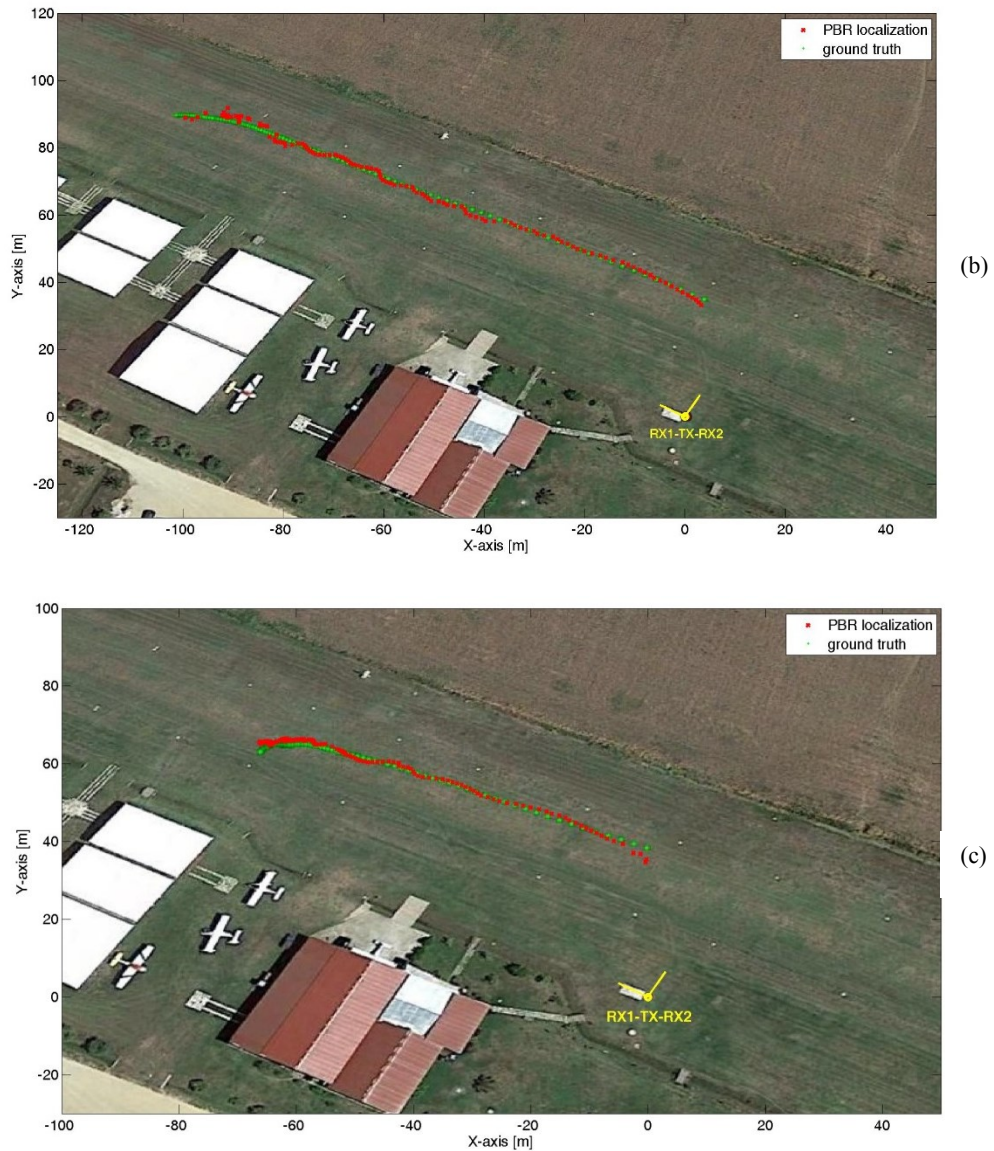


Figure 33. Tests against a landing aircraft: (a) picture of the performed tests; (b)-(c) PBR results compared to the available ground-truth for two different tests.

### 6.3.2. TEST AGAINST SMALL AIRCRAFTS MANEUVERING ALONG THE AIRFIELD

In this sub-section, we report the results of a test performed against two targets of opportunity taken during a typical operative condition of the airfield. Specifically, during the PBR receiver registration of 20 s, a small aircraft, after leaving the hangar, was moving toward the taxiway (see the aircraft on the ground on the left side of Figure 34(a)). Contemporaneously, an ultralight aircraft, a powered paraglider, was flying over the runway involved in a ‘touch and go’ landing maneuver.

The output yield by the PBR sensor fielded in that area is shown in Figure 34(b). Specifically, different colors are used for the different sequences of plots identified by the tracker on the range/velocity plane

(see Figure 32). Once converted in Cartesian coordinates, the two sequences of plots clearly reveal the presence of the two observed targets with a reliable indication of their instantaneous positions.

In this particular test, it would have been of great interest the capability to measure the target height above ground. This could be in principle obtained by exploiting an additional surveillance antenna displaced in the vertical direction in order to estimate the elevation angle of the target's echo. Unfortunately, such additional antenna was not available during this test as it was mostly intended to demonstrate the ground targets surveillance capability of the PBR sensor.

In addition, Figure 35 and Figure 36 report the results of other two tests involving different target types.

All the results obtained with the adopted setup show that the conceived system can be effective in monitoring aircraft activities in the proximity of the runway in order to avoid accidents due to intentional/unintentional runway incursions.

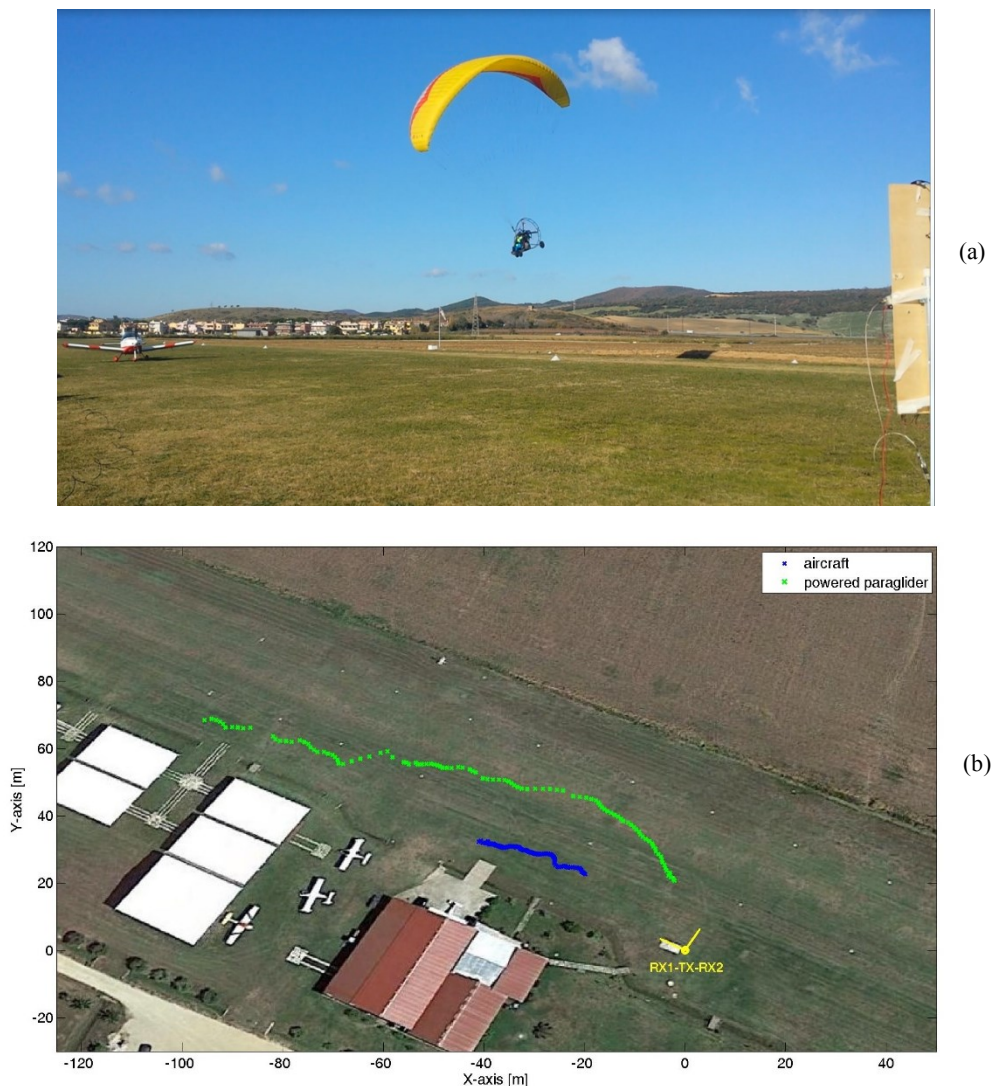


Figure 34. Test against two maneuvering aircrafts: (a) picture of the performed test; (b) PBR results compared to the available ground-truth.





(a)



(b)

Figure 35. Test against a maneuvering aircrafts: (a) picture of the performed test; (b) PBR results compared to the available ground-truth.



(a)



(b)

Figure 36. Test against a small maneuvering aircraft: (a) picture of the performed test; (b) Wi-based PBR localization results.

### 6.3.3. TEST AGAINST AN UTILITY VEHICLE

As mentioned in sub-section 6.2, various ground vehicles might be moving on the airfield surface or in its neighboring areas. Such vehicles might include private cars belonging to the airfield users or utility vehicles employed within the airfield for maintenance, service and rescue activities.

To verify the possibility of the PBR sensor to effectively control the ground vehicles traffic along the airfield, the third reported test type employed an utility car as cooperative target [see Figure 37(a)]. During this test, the car performed a U-turn during which it got very close to the runway. The comparison between the PBR results and the GPS based ground truth is shown in Figure 37(b), where again we observe that they are in large agreement.

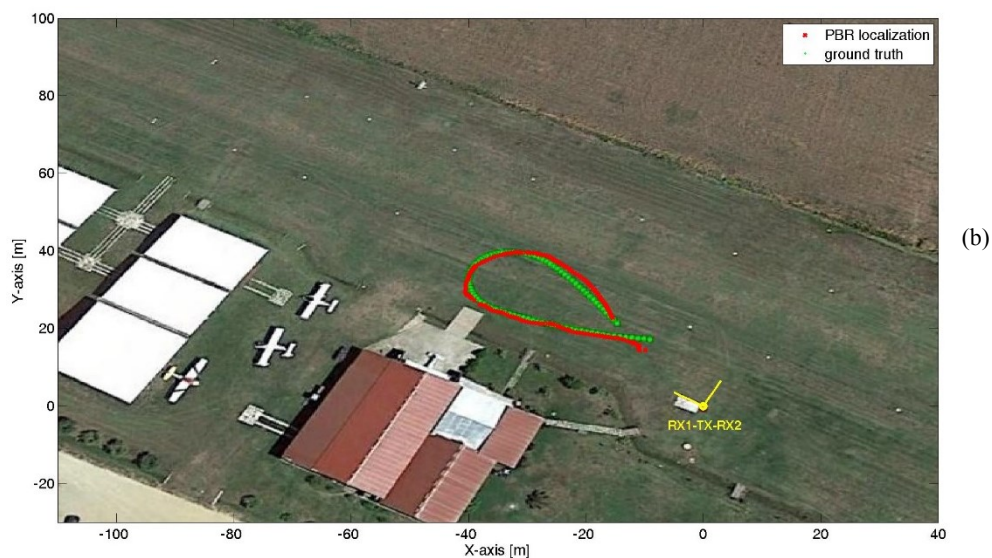


Figure 37. Test against an utility vehicle: (a) vehicular target employed; (b) PBR results compared to the available ground-truth.

#### 6.3.4. TEST AGAINST HUMAN TARGETS

In typical operative conditions, many people might be walking around different airfield areas. Therefore, aiming at improving safety and security in such scenarios, the capability to reliably detect, localize and track human targets might be crucial.

This possibility is proved in this last reported test, where the PBR sensor is operated against three people walking in the proximity of the airfield facilities (i.e. club-house, restaurant, etc.) along different trajectories [see Figure 38(a)]. The PBR results are reported in Figure 38(b) where different colors are used to indicate different tracks. For illustration purposes, ideal boundaries have been defined between an allowed area (close to the airfield facilities) and a forbidden area (that adjacent to the runway) and the red color has been used for the tracks of the targets crossing the boundaries.



Despite the accuracy of the sensor is not extremely high when operating against human targets, the performed exercise resembling a possible security application proves its suitability in the considered scenarios. Notice that the same approach can be exploited to prevent runway incursions by ill-intentioned people and wild animals living in neighboring areas.

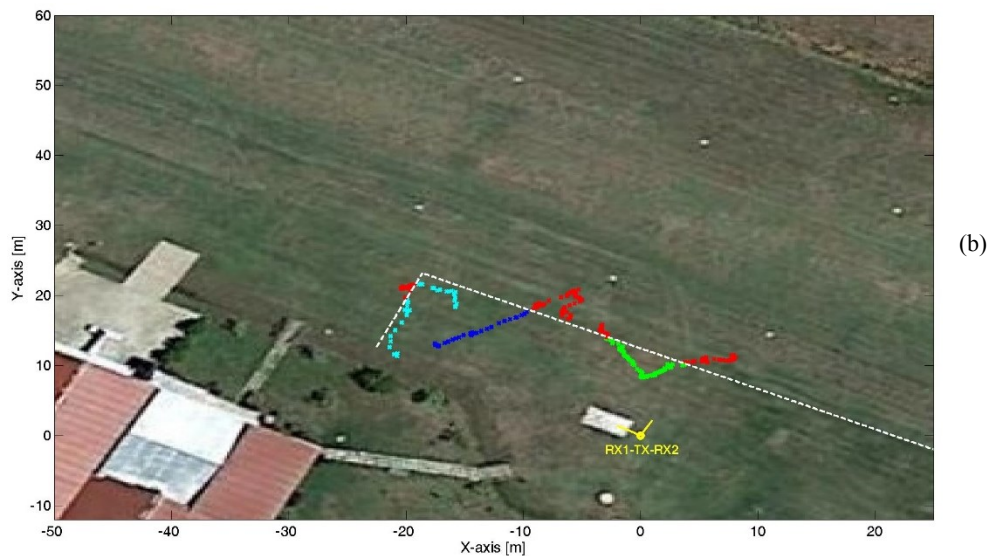


Figure 38. Test against human targets: (a) picture of the performed test; (b) PBR results employed for the security exercise.

As a last remark, it is worth recalling that all the reported results do not include a tracking stage in the  $x$ - $y$  plane which might increase the final positioning accuracy. Moreover both the achievable coverage and the target localization capability could be significantly enhanced if an appropriate network of passive receivers was deployed in the considered area. This is indeed a viable solution particularly when monitoring areas of small dimensions, since the network geometry can be carefully designed to limit the system complexity while guaranteeing the availability of measurements with a sufficient degree of spatial diversity.



## 7. WIFI-BASED PASSIVE RADAR IN FORWARD SCATTER CONFIGURATION

So far, WiFi transmissions have been exploited for target detection, localization and imaging against conventional geometries.

Aiming at extending the range of possible applications for the conceived sensor, the feasibility of non-conventional geometries has been also investigated in this work. In particular, WiFi signals are considered as potential source of opportunity for a passive radar in forward scatter configuration.

### 7.1. MOTIVATIONS

In the last years, the forward scattering radar (FSR) has received significantly interest. FSR is an extreme bistatic radar configuration where the bistatic angle is near to  $180^\circ$  (see Figure 39). Differently from monostatic and bistatic operation modes, the received signal is not the reflection from the target but rather the shadow of the target. In fact, when the target moves on or close to the baseline, it blocks part of the transmitted signal and this leads to a reduction of the received signal power, [46]-[48].

As well known from the literature, due to the forward scattering effect, the FSR offers a number of interesting features. Its most attractive peculiarity is the enhancement of the radar cross-section (RCS) when a target crosses the baseline, which might result in a significant improvement in detection capability compared with the monostatic geometry. Moreover, it is independent from the target material; therefore, these systems are robust to detect stealth and other such targets. In addition, when a target moves across the baseline, the target signature is produced as a result of the interference between the direct signal from the transmitter antenna and the target signal. Obviously, different targets have different shapes, so automatic target classification (ATC) can be applied. Alternatively, Shadow Inverse Synthetic Aperture Radar (SISAR) techniques can be applied on the forward signal to extract a profile of the target that can be used as input in ATC procedures. On the other hand, FSR system is characterized by the absence of range resolution and a limited operational area (when the targets approach the baseline, namely when the bistatic angle is nearly to  $180^\circ$ ).

Numerous works proved the effectiveness of FSR using active systems. For example, in [49]-[53] it was shown that FSR can be used for ground target detection and classification. In [54]-[55] FSR is applied for air target detection and tracking whereas in [56]-[57] for detection and classification of maritime objects. Moreover, recently, there has been a growing attention in the use of FSR configuration in passive radar [58]. In fact, the exploitation of an existing illuminator of opportunity allows additional advantages such as low cost, low vulnerability to electronic countermeasure, covert operation and low environmental impact. In particular, in [59]-[63] has been demonstrated the feasibility of such geometry using GSM, GNSS and DVB-T signals as illuminators of opportunity.

In this work, aiming at local area monitoring, WiFi signals are considered as potential source of opportunity for a passive forward scatter radar (PFSR).

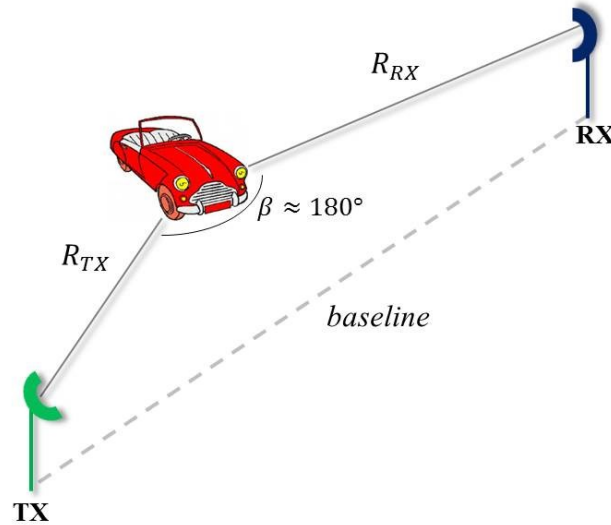


Figure 39. FSR geometry.

## 7.2. ACQUISITION CAMPAIGN AND DATA COLLECTION

Aiming at understanding the impact of the forward geometry for applications of vehicles monitoring, a dedicated acquisition campaign has been performed.

Specifically, the tests have been performed in a wide parking area in Cisterna di Latina (Italy) and the exploited geometry is depicted in Figure 40. The considered live data have been collected by means of the quad-channel PBR receiver described in sub-section 5.1.

A commercial WiFi AP was used as transmitter of opportunity; in particular, it was configured to transmit in channel 6 of the WiFi band (2437 MHz), set up to emit a regular Beacon signal exploiting a DSSS modulation at 3 ms. Its output was connected to the TX antenna, located at the point with coordinates  $(x_{TX}, y_{TX}) = (0,0)$  m. Then a directional coupler was used to send a -20 dB copy of the transmitted signal (the reference signal) to the first receiving channel. The second channel of the receiving system was directly connected to the surveillance antenna (RX) which was located in  $(x_{RX_F}, y_{RX_F}) = (0,D)$  m in forward configuration with respect to the TX with baseline  $D=40$  m. Both antennas were mounted at about 1.25 m of height with respect to the ground. After a fully coherent base-band down-conversion stage, the signals collected at the different receiving channels are sampled at 22 MHz and stored for off-line processing. In addition, also the monostatic geometry has been considered (see Figure 40) in  $(x_{RX_M}, y_{RX_M}) = (0,0)$  m. In particular, the comparison between monostatic and forward configurations will be shown in the next section. Notice that for a fair comparison between monostatic and forward configurations, all the antennas are commercial WiFi panel antennas and are characterized by a gain of 12 dBi, a front-to-back ratio of 15 dB and beamwidths equal to  $80^\circ$  and  $23^\circ$  on the horizontal and vertical planes, respectively. Moreover, cables of the same length (100 m) were employed in order to have comparable losses in both receivers.

Different tests have been performed using cars as cooperative targets. The cars move orthogonally to the TX-  $RX_F$  baseline crossing it at the middle point with a bistatic angle  $\beta \approx 180^\circ$ . Specifically, they move from point  $A \approx (-40,20)$  m to point  $B \approx (40,20)$  m (red line in Figure 40) with velocity of about 4-5 m/s depending on the considered test. Four car models have been taken in account: Peugeot 107, Volkswagen

Polo, Citroen C3 and Fiat Punto Evo. The dimensions, the photos and the number of performed tests for each car are reported in Table III.

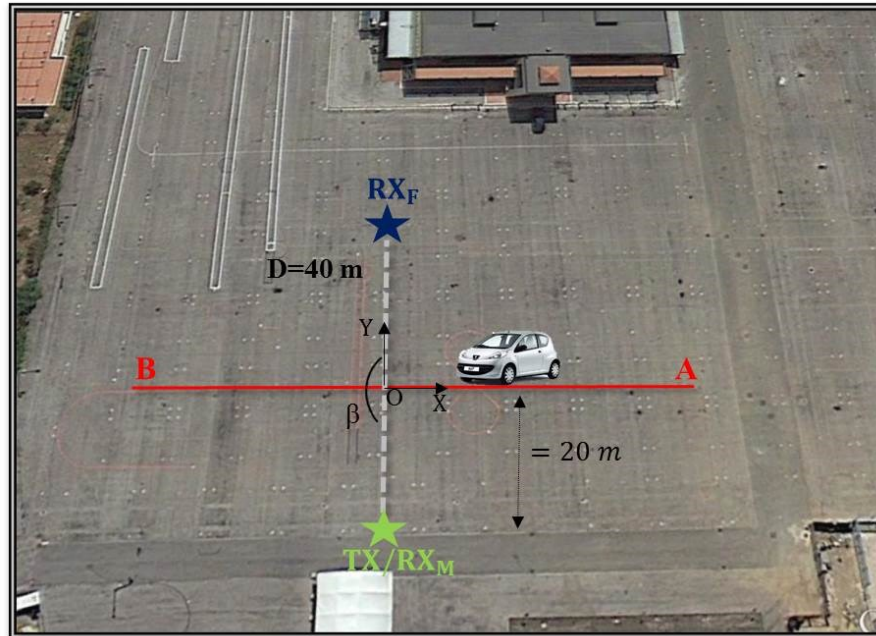






Figure 40. Sketch of the acquisition geometry.

Table III. Car models used in the acquisition campaign.

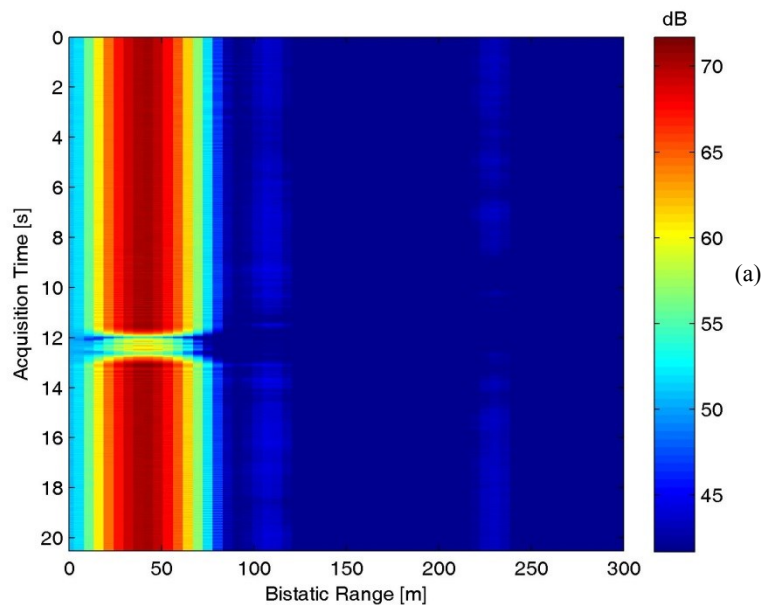
| Car model          | Dimensions<br>(length, width, height) | Photo                                                                                | Number of<br>test |
|--------------------|---------------------------------------|--------------------------------------------------------------------------------------|-------------------|
| Peugeot 107        | 3.43 x 1.63 x 1.47 m                  |  | 8                 |
| Volkswagen<br>Polo | 3.715 x 1.655 x 1.420 m               |  | 4                 |
| Citroen C3         | 3.941 x 1.728 x 1.524 m               |  | 5                 |
| Fiat Punto Evo     | 4.065 x 1.690 x 1.49 m                |  | 10                |



In order to evaluate the effectiveness of the existing processing chain, the same WiFi-based passive radar processing scheme for target detection depicted in Figure 1 has been applied against the collected forward signal.

### 7.2.1. ANALYSIS OF THE RANGE COMPRESSED DATA

As an example, Figure 41(a) shows the bistatic range-acquisition time map with range sidelobes control and without disturbance cancellation for a test with a Fiat Punto Evo as cooperative target. The map has been normalized to the thermal noise power level so that the value at each map location represents the estimated SNR. As it is apparent, a strong contribution appears at about 40 m spreading along the acquisition time corresponding to the direct signal transmitted by the transmitting antenna. However, we observe a reduction of the direct signal power approximately in correspondence of the time interval from 12 to 13 s; this is a consequence of the fact that when the target crosses the baseline, it blocks the incident wave of the TX antenna. The same results are visible in Figure 41(b), which reports the bistatic range-acquisition time map for a test with a Peugeot 107 as cooperative target. In this case, a direct signal power reduction is observed in the time interval 10-11 s.



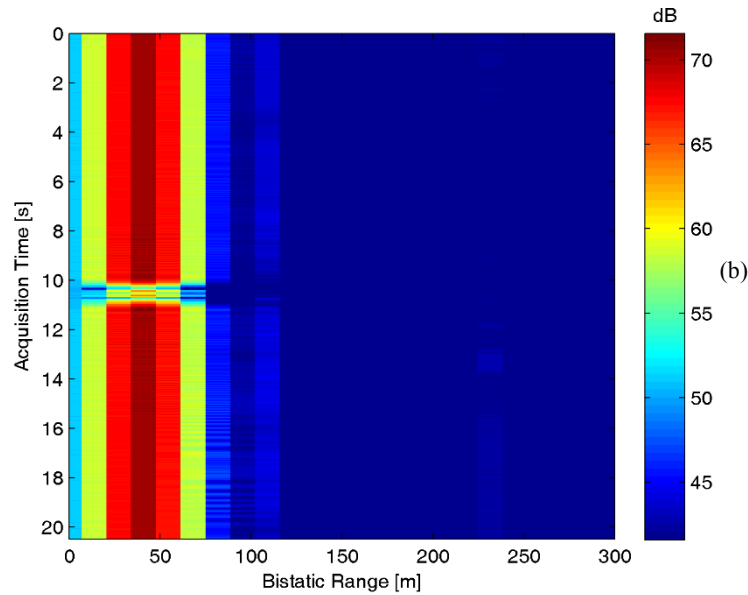
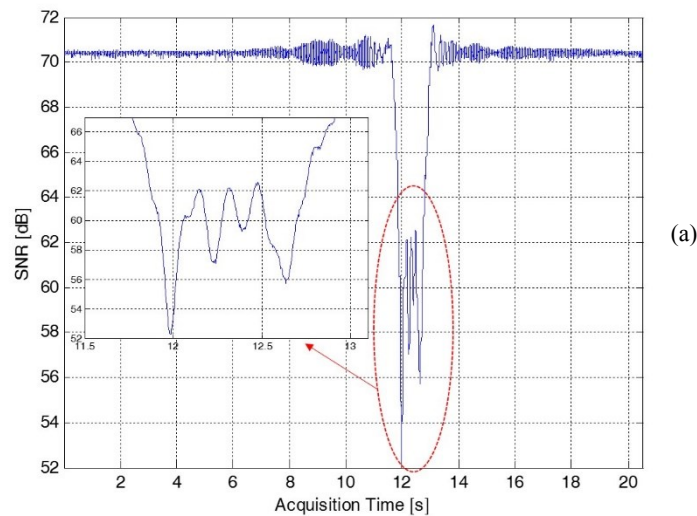


Figure 41. Bistatic range-acquisition time maps for two different tests involving two different car models. (a) Fiat Punto Evo; (b) Peugeot 107.

From the range compressed data without disturbance cancellation, the slow-time profile at the direct signal range bin can be extracted. Subsequently, its square modulus can be obtained, representing the target signature.

As an example, Figure 42 shows the Fiat Punto Evo and Peugeot 107 vehicle signature, respectively, which have been extracted from the bistatic range-acquisition time map of Figure 41. In both cases, we observe a direct signal power reduction up to 18 dB when the target crosses the baseline. In addition, it is interesting to notice as different car models yields different signature shapes. These can be exploited by a “Signature analysis” block as described in the following sections.



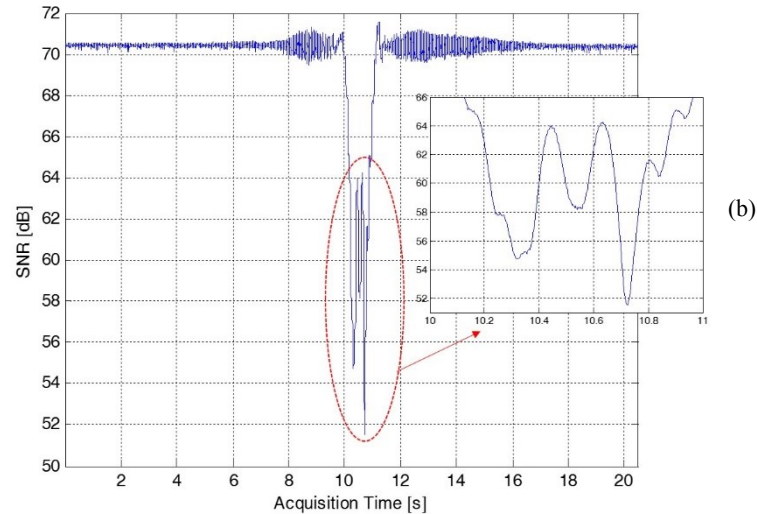


Figure 42. Target signature for the same test of Figure 41. (a) Fiat Punto Evo; (b) Peugeot 107.

### 7.2.2. DETECTION PERFORMANCE

In this sub-section, we evaluate the detection performance of the forward configuration.

The WiFi-based passive radar processing scheme for target detection depicted in Figure 1 has been applied against the collected surveillance signal. In particular, the cancellation stage has been performed by adopting the ECA-S over a range of 500 m (i.e.  $K = 36$  taps @  $f_s = 22\text{MHz}$ ) with  $T_A = 0.1$  s and  $T_S = 3$  ms. Notice that this value of range extension has been selected in order to remove the direct signal and all the disturbance contributions at zero velocity, thus allowing us to correctly detect the target. A CPI of 0.1 s is used to evaluate the bistatic range-velocity map over consecutive portions of the acquired signals (frames) with a fixed displacement of 0.1 s (10 frames per second are thus obtained); finally, target detection is performed by resorting to a standard cell-average CFAR threshold with a probability of false alarm  $P_{fa}$  equal to  $10^{-4}$ .

As an example, Figure 43 shows all the plots collected over the whole acquisition time over the bistatic range-velocity plane for the same tests considered in Figure 41 and Figure 42. As it is apparent, in both cases the target has been detected. In particular, the cross-range movement of the target (see Figure 40) results in a parabolic sequence of detections over the bistatic range-velocity plane with vertex (40,0) m. We note that we have not only target detection but also false alarms (that might be easily discarded by a tracking algorithm as shown in sub-section 5.1) and multipath effects.

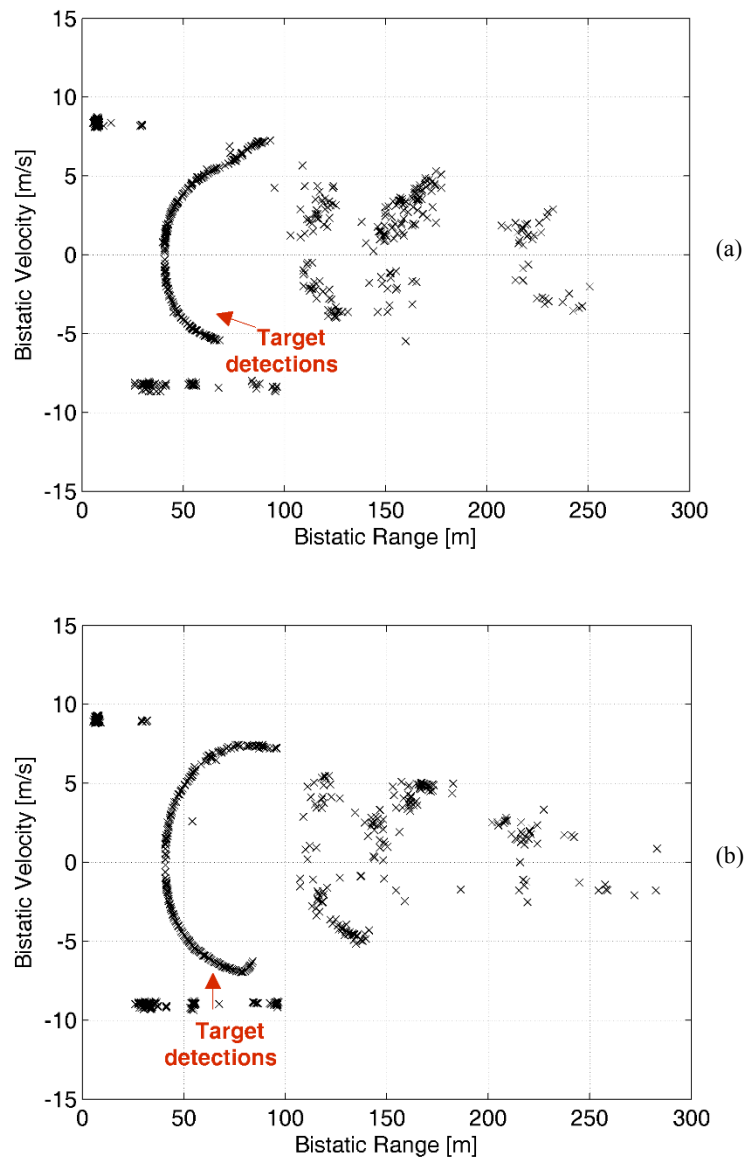


Figure 43. Detections over the range-velocity plane for the same tests of Figure 41 and Figure 42. (a) Fiat Punto Evo; (b) Peugeot 107.

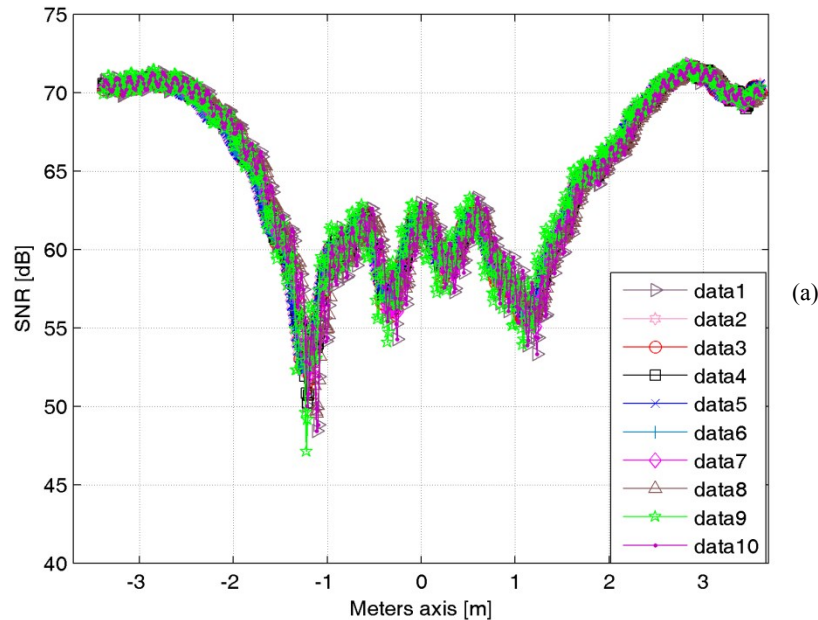
### 7.3. TARGET CLASSIFICATION RESULTS

In this sub-section, we investigated the potentialities of WiFi-based PFSR for ATC of ground moving targets.

#### 7.3.1. SIGNATURE ANALYSIS AND POSSIBLE EXPLOITATION

For a fair comparison, the vehicle signature extracted from the range compressed data (see Figure 42) cannot be used directly in a classification system because its velocity affects its shape. Therefore, a target motion estimation procedure has to be applied. Following the same strategy as in Section 4, in this work, the signal after disturbance cancellation is used to estimate the component  $\hat{v}$  of the target velocity orthogonal to the baseline. This estimate is then used to scale the vehicle signature from time-axis to meters-axis. This allows to directly compare (on a common axis) the signatures yield by each vehicle at different tests.

For example, Figure 44(a) reports all the signatures of the Fiat Punto Evo obtained in the performed tests. A similar shape is clearly visible for all the cases. In addition, Figure 44(b) shows the signature of the Peugeot 107 on 8 tests; we observe that also in this case, the same vehicle yields a very stable signature. Moreover, it is interesting to notice as different car models have different signature shapes. This suggests the possibility to exploit the signatures for classification purposes.



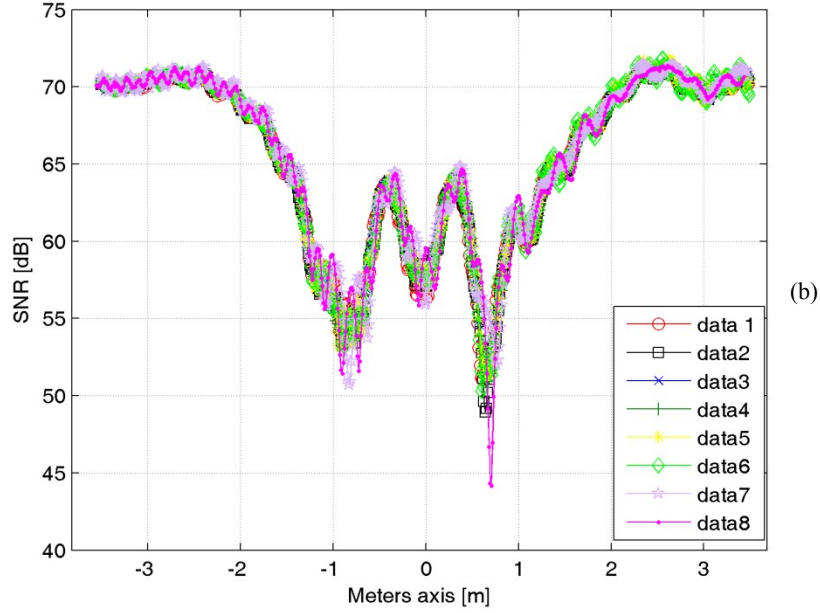


Figure 44. Signatures comparison for the same target model on different tests. (a) Fiat Punto Evo; (b) Peugeot 107.

In particular, a minimum Euclidean distance criteria has been adopted to evaluate the similarity among different car models.

The adopted methodology is explained below. The target signature obtained from the  $k$ -th car model at the  $m$ -th test is collected in the vector  $\underline{X}_{k,m}$  of dimensions  $N \times 1$ . For the considered case,  $k = 1, \dots, 4$  and  $m = 1, \dots, M_k$  where  $M_k$  is the number of the performed tests for the  $k$ -th car model (see Table III). Successively, each target signature  $\underline{X}_{\bar{k},\bar{m}}$  is assumed to be the reference signature and the Euclidean distance  $\eta_{k,m}^{(\bar{k},\bar{m})}$  with all the other signatures  $\underline{X}_{k,m}$  is evaluated:

$$\eta_{k,m}^{(\bar{k},\bar{m})} = \frac{1}{N} \|\underline{X}_{\bar{k},\bar{m}} - \underline{X}_{k,m}\|^2 \quad (43)$$

with  $k = 1, \dots, 4$  and  $m = 1, \dots, M_k$ .

Obviously, for  $\bar{k} = k$  and  $\bar{m} = m$  (i.e. when the same car and number of test is considered), we obtain  $\eta_{k,m}^{(\bar{k},\bar{m})} = 0$ .

As is apparent, by successively varying the reference signature ( $\bar{k} = 1, \dots, 4$  and  $\bar{m} = 1, \dots, M_{\bar{k}}$ ) a  $P \times P$  matrix of values is obtained, being  $P = \sum_{k=1}^4 M_k$ , containing all the Euclidean distances evaluated for every possible pairs of tests.

### 7.3.2. RESULTS AGAINST EXPERIMENTAL DATA

Based on the methodology described in the previous sub-section, the Table IV shows the results obtained against the tests that employed the Peugeot 107 and the Fiat Punto Evo. Specifically the table reports the



Euclidean distances (in logarithmic scale) evaluated using pairs of tests employing the same car (the Peugeot) and pairs of tests employing the two different cars. As it is apparent, the distances achieved when same car model signatures are compared are always lower than the distances achieved when different car models have been considered. Following the same criteria, Figure 45 reports in logarithmic scale the estimated distances for all the considered tests (i.e. the whole  $P \times P$  matrix, being  $P = 27$  in our case). Notice that the color scale dynamic range has been lower limited since zeros are obtained on the main diagonal. In particular, the first block (surrounded by a blue dashed line) and the fourth block (surrounded by a light blue dashed line) on the first block column correspond to the first and second blocks of Table IV, respectively.

Table IV. Euclidean distance values ( $10 \log_{10} \eta$ ) between Peugeot 107 and Fiat Punto Evo.

|             |    | Peugeot 107 |             |             |             |             |             |             |             |
|-------------|----|-------------|-------------|-------------|-------------|-------------|-------------|-------------|-------------|
|             |    | 1           | 2           | 3           | 4           | 5           | 6           | 7           | 8           |
| Peugeot 107 | 1  | <u>-Inf</u> | 35,62       | 35,44       | 36,64       | 37,13       | 37,46       | 42,72       | 42,83       |
|             | 2  | 35,63       | <u>-Inf</u> | 33,43       | 33,84       | 35,48       | 38,27       | 42,88       | 42,60       |
|             | 3  | 35,44       | 33,43       | <u>-Inf</u> | 31,28       | 34,16       | 37,76       | 42,25       | 42,15       |
|             | 4  | 36,64       | 33,84       | 31,28       | <u>-Inf</u> | 35,58       | 38,96       | 43,16       | 42,51       |
|             | 5  | 37,13       | 35,48       | 34,17       | 35,58       | <u>-Inf</u> | 38,08       | 42,83       | 42,68       |
|             | 6  | 37,46       | 38,26       | 37,77       | 38,95       | 38,06       | <u>-Inf</u> | 43,03       | 43,43       |
|             | 7  | 42,73       | 42,88       | 42,25       | 43,15       | 42,83       | 43,04       | <u>-Inf</u> | 45,16       |
|             | 8  | 42,82       | 42,53       | 42,14       | 42,46       | 42,68       | 43,37       | 45,16       | <u>-Inf</u> |
| FIAT Punto  | 1  | 55,08       | 55,02       | 55,10       | 54,85       | 55,18       | 55,44       | 55,53       | 55,32       |
|             | 2  | 55,20       | 55,13       | 55,22       | 54,97       | 55,29       | 55,56       | 55,67       | 55,44       |
|             | 3  | 55,16       | 55,10       | 55,16       | 54,94       | 55,26       | 55,50       | 55,55       | 55,34       |
|             | 4  | 55,20       | 55,13       | 55,21       | 54,97       | 55,30       | 55,55       | 55,61       | 55,39       |
|             | 5  | 55,08       | 55,02       | 55,11       | 54,85       | 55,18       | 55,44       | 55,57       | 55,34       |
|             | 6  | 54,69       | 54,62       | 54,68       | 54,42       | 54,78       | 55,02       | 55,17       | 54,95       |
|             | 7  | 54,76       | 54,72       | 54,80       | 54,57       | 54,87       | 55,12       | 55,24       | 55,04       |
|             | 8  | 54,89       | 54,84       | 54,91       | 54,66       | 54,97       | 55,20       | 55,37       | 55,17       |
|             | 9  | 54,69       | 54,64       | 54,73       | 54,48       | 54,80       | 55,08       | 55,19       | 54,96       |
|             | 10 | 54,66       | 54,60       | 54,67       | 54,41       | 54,77       | 55,02       | 55,16       | 54,94       |

From Figure 45, it is evident that the lowest values of the Euclidean distances are on the main diagonal blocks, which correspond to the tests involving the same car. Being the targets sorted in ascending order of dimensions, it is interesting to observe that the greater the difference in length among the cars, the greater the obtained distances.

For a numerical comparison, for each reference signature  $\underline{X}_{k,\bar{m}}$  we report in Table V a synthesis of the results shown in Figure 45. Specifically the following strategy is adopted. The highest value is selected among results obtained with pairs of test employing the same car, namely the largest distance is reported between homologous tests (green cells). In contrast, the smallest value is reported among those obtained with pairs of tests involving a different car (yellow cells). Basically, the generic columns of Table V ( $D_k^{(\bar{k},\bar{m})}$ ,  $k = 1, \dots, 4$ ) is based on the reference signature  $\underline{X}_{k,\bar{m}}$  and is built as:

$$D_k^{(\bar{k}, \bar{m})} = \begin{cases} \max_{m=1, \dots, M_k} \eta_{k,m}^{(\bar{k}, \bar{m})} & \text{for } k = \bar{k} \\ \min_{m=1, \dots, M_k} \eta_{k,m}^{(\bar{k}, \bar{m})} & \text{for } k \neq \bar{k} \end{cases} \quad (44)$$

It is worth noticing that a worst-case strategy is adopted that clearly penalizes the tests performed with identical cars. For a given target signature  $X_{\bar{k}, \bar{m}}$ , we conclude that the system is able to discriminate among different car signatures if the largest Euclidean distance measured among homologous tests is smaller than the smallest distance measured with any of the tests employing a different car model. If this is the case, the last row of the Table **v** is set to 1, otherwise is 0. Therefore:

$$F^{(\bar{k}, \bar{m})} = \begin{cases} 1 & \text{if } D_{\bar{k}}^{(\bar{k}, \bar{m})} < \min_{\substack{k=1, \dots, 4 \\ k \neq \bar{k}}} D_k^{(\bar{k}, \bar{m})} \\ 0 & \text{if } D_{\bar{k}}^{(\bar{k}, \bar{m})} > \min_{\substack{k=1, \dots, 4 \\ k \neq \bar{k}}} D_k^{(\bar{k}, \bar{m})} \end{cases} \quad (45)$$

As it is apparent, in the majority of cases, the system is able to correctly associate the target signature to its class. Just in a single case, the Fiat Punto is confused with the Citroen C3. However, it should be pointed out that these two employed vehicles have quite similar shape and dimensions (see Table III). Nevertheless, a number of tests employing these two cars still yield correct results.

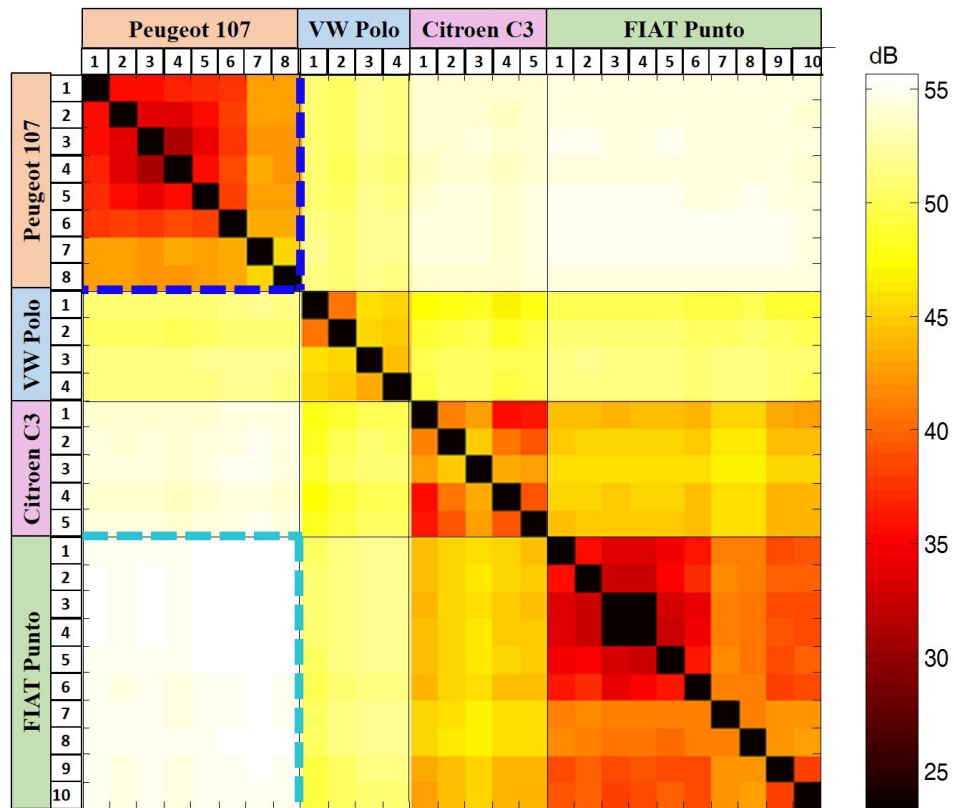


Figure 45. Euclidean distance values for all the considered tests.



Table V. Synthesis of the results presented in Figure 45 ( $10\log_{10} \eta$ ).

|                    | Peugeot 107 |       |       |       |       |       |       |       | VW Polo |       |       |       |       | Citroen C3 |       |       |       |       | FIAT Punto |       |       |       |       |       |       |       |       |  |
|--------------------|-------------|-------|-------|-------|-------|-------|-------|-------|---------|-------|-------|-------|-------|------------|-------|-------|-------|-------|------------|-------|-------|-------|-------|-------|-------|-------|-------|--|
|                    | 1           | 2     | 3     | 4     | 5     | 6     | 7     | 8     | 1       | 2     | 3     | 4     | 1     | 2          | 3     | 4     | 5     | 1     | 2          | 3     | 4     | 5     | 6     | 7     | 8     | 9     | 10    |  |
| <b>Peugeot 107</b> | 42,82       | 42,88 | 42,25 | 43,15 | 42,83 | 43,37 | 45,16 | 45,16 | 50,61   | 49,95 | 51,47 | 51,09 | 53,59 | 53,80      | 53,82 | 53,40 | 53,79 | 54,43 | 54,46      | 54,32 | 54,33 | 54,43 | 54,20 | 54,26 | 54,35 | 54,24 | 54,07 |  |
| <b>VW Polo</b>     | 50,26       | 50,30 | 50,22 | 49,97 | 50,45 | 50,87 | 50,89 | 50,88 | 45,99   | 45,19 | 45,76 | 45,44 | 47,33 | 47,98      | 48,31 | 47,06 | 47,76 | 49,84 | 49,99      | 49,75 | 49,84 | 49,82 | 49,31 | 49,53 | 49,85 | 48,79 | 48,83 |  |
| <b>Citroen C3</b>  | 53,74       | 53,65 | 53,72 | 53,39 | 53,78 | 54,17 | 54,34 | 54,04 | 47,34   | 48,66 | 49,77 | 49,70 | 42,62 | 44,87      | 44,97 | 43,15 | 42,93 | 44,19 | 44,30      | 44,01 | 44,20 | 44,45 | 43,59 | 45,29 | 45,29 | 43,18 | 42,69 |  |
| <b>FIAT Punto</b>  | 54,66       | 54,60 | 54,67 | 54,41 | 54,77 | 55,02 | 55,16 | 54,94 | 49,17   | 50,23 | 50,86 | 50,92 | 42,71 | 44,40      | 45,31 | 43,72 | 43,67 | 41,52 | 41,54      | 41,14 | 41,29 | 41,40 | 41,19 | 42,32 | 42,76 | 42,22 | 42,60 |  |
|                    | 1           | 1     | 1     | 1     | 1     | 1     | 1     | 1     | 1       | 1     | 1     | 1     | 1     | 0          | 1     | 1     | 1     | 1     | 1          | 1     | 1     | 1     | 1     | 1     | 1     | 1     | 1     |  |

## 8. MONOSTATIC VS FORWARD GEOMETRY

As well known from the literature [46]-[48], due to the forward scattering effect, the most attractive peculiarity of the FSR geometry is the enhancement of RCS when a target crosses the baseline, which might result in a significant improvement in detection capability compared with the monostatic geometry.

In sub-section 8.1, first we focus on the power budget analysis in both monostatic and forward configurations assuming an isotropic RCS pattern. Then, in sub-section 8.2 in order to evaluate only the effect of the target RCS and effectively verify that the forward geometry yields an enhancement of the RCS compared with the conventional geometries, different tests were performed using more vehicular targets (each one characterized by its own RCS). In addition, the Monostatic and Forward configurations are compared in terms of target detection capability. Finally, in sub-section 8.3, some considerations about the computational load saving and the system complexity reduction in FW geometry are discussed.

### 8.1. POWER BUDGET ANALYSIS

In this sub-section, we focus on the power budget analysis in both monostatic and the forward configurations for ground target detection assuming an isotropic RCS pattern.

In particular, we assume to be interested in monitoring a rectangular area of length  $D$  and width  $W$  as shown in Figure 46; two different radar geometries have been considered: monostatic and forward. The monostatic receiver is situated in the point  $TX = RX_M = (X_{TX}, Y_{TX}, Z_{TX})$  and the forward receiver in  $RX_F = (X_{RX_F}, Y_{RX_F}, Z_{RX_F})$  where the distance  $D$  represents the baseline. A  $(X, Y, Z)$  coordinate system has been defined assuming the origin of the system located on the middle of the baseline with X axis aligned with the width of the area and Y axis aligned along the baseline. Supposing that the heights of the transmitting and receiving antennas are the same and equal to  $z_0$ , the coordinates of the transmitter and the receivers become  $TX = RX_M = (0, -D/2, z_0)$  and  $RX_F = (0, D/2, z_0)$ .

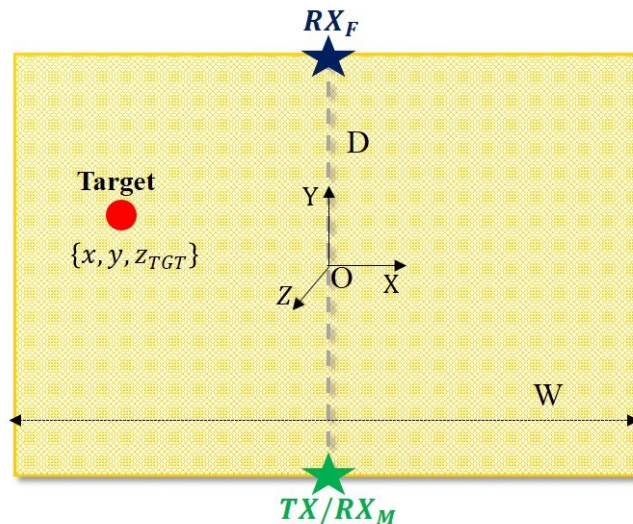


Figure 46. Example of region to be monitored.

The power  $P_{RX}$  received from a target moving in the region of interest, for any bistatic radar including forward and monostatic geometry, can be written as:

$$P_{RX} = P_{TX} G_{TX} G_{RX} \frac{4\pi}{\lambda^2} \sigma_{RCS} L_{TX} L_{RX} \quad (46)$$

where  $P_{TX}$  is the transmitted power,  $G_{TX}$  and  $G_{RX}$  are the gains of the transmitting and receiving antennas in the target's direction, respectively,  $\lambda$  is the wavelength,  $\sigma_{RCS}$  is the target's RCS and  $L_{TX}$  and  $L_{RX}$  are the propagation losses due to the transmitter-to-target and target-to-receiver path, respectively. Obviously, the parameters  $G_{TX}$ ,  $G_{RX}$ ,  $\sigma_{RCS}$ ,  $L_{TX}$  and  $L_{RX}$  depend on the system's geometry or viewing angles. If we assume that the target has an isotropic RCS pattern, the target's RCS does not depend on viewing angles and  $\sigma_{RCS}$  is a constant.

Under the condition of free-space model (that assumes that there are not ground reflections, see Figure 39), the propagation losses depend only from  $\lambda$  and the direct paths  $R_{TX}$  and  $R_{RX}$  [85]-[86]:

$$L_{TX} = \left( \frac{\lambda}{4\pi R_{TX}} \right)^2 \quad ; \quad L_{RX} = \left( \frac{\lambda}{4\pi R_{RX}} \right)^2 \quad (47)$$

Therefore, the received target power becomes:

$$P_{RX} = P_{TX} G_{TX} G_{RX} \sigma_{RCS} \frac{\lambda^2}{(4\pi)^3 R_{TX}^2 R_{RX}^2} \quad (48)$$

For a generic target of coordinates  $(x, y, z)$  within the rectangular region (namely,  $|x| < \frac{W}{2}$ ,  $|y| < \frac{D}{2}$  and  $z = z_{TGT}$ ), the SNR is defined as the ratio between the received power from the target  $P_{RX}$  and the noise power  $P_n$ . Therefore:

$$SNR = \frac{P_{TX} G_{TX} G_{RX} \sigma_{RCS} \lambda^2}{(4\pi)^3 R_{TX}^2 R_{RX}^2 P_n} \quad (49)$$

For sake of simplicity, it is assumed that the transmitting and both receiving antennas are isotropic (namely that  $G_{TX} = G_{RX} = 1$ ) and that  $\sigma_{RCS}$ ,  $P_n$ ,  $\lambda$  and  $P_{TX}$  are the same for the monostatic and forward receivers. In this way, the SNR in (49) can be written as:

$$SNR_M = \frac{K}{R_{TX}^2 R_{RX_M}^2} \quad ; \quad SNR_F = \frac{K}{R_{TX}^2 R_{RX_F}^2} \quad \text{with } K = \frac{P_{TX} \sigma_{RCS} \lambda^2}{(4\pi)^3 P_n} \quad (50)$$

for monostatic ( $SNR_M$ ) and forward ( $SNR_F$ ) case, respectively, where  $R_{RX_M}$  is the target-to-monostatic receiver distance whereas  $R_{RX_F}$  is the target-to-forward receiver distance. Specifically, with reference to Figure 46:

$$R_{TX} = R_{RX_M} = \sqrt{(x - x_{TX})^2 + (y - y_{TX})^2 + (z - z_0)^2} = \sqrt{x^2 + \left(y + \frac{D}{2}\right)^2 + \Delta z^2} \quad (51)$$

$$R_{RX_F} = \sqrt{(x - x_{RX_F})^2 + (y - y_{RX_F})^2 + (z - z_0)^2} = \sqrt{x^2 + \left(y - \frac{D}{2}\right)^2 + \Delta z^2}$$

with  $\Delta z = z - z_0$ .

The simplified version of bistatic radar equation in (50) highlights that, for each point of the space, the SNR measured at the receiver depends on the target position with respect to both the transmitter and the receiver. In particular, it is easy to note in eq. (50) that the SNR is inversely proportional to the product between transmitter-to-target and target-to-receiver distances. It is evident that among all points within the rectangular region, the worst-point SNR is the one with the maximum product of the between transmitter-to-target and target-to-receiver distances. In particular:

$$R_{TX}R_{RXM} = x^2 + \left(y + \frac{D}{2}\right)^2 + \Delta z^2 \quad (52)$$

$$R_{TX}R_{RXF} = \sqrt{\left[x^2 + \left(y + \frac{D}{2}\right)^2 + \Delta z^2\right] \left[x^2 + \left(y - \frac{D}{2}\right)^2 + \Delta z^2\right]}$$

Therefore, after few steps, it is easy to obtain:

$$\max_{(x,y)}(R_{TX}R_{RXM}) = \left(\frac{W}{2}\right)^2 + D^2 + \Delta z^2 \quad \text{in } (|x|, y) = \left(\frac{W}{2}, \frac{D}{2}\right) \quad (53)$$

$$\begin{aligned} \max_{(x,y)}(R_{TX}R_{RXF}) &= \\ &= \begin{cases} \sqrt{\left[\left(\frac{W}{2}\right)^2 + D^2 + \Delta z^2\right] \left[\left(\frac{W}{2}\right)^2 + \Delta z^2\right]} & \text{in } (|x|, |y|) = \left(\frac{W}{2}, \frac{D}{2}\right) \quad \text{if } D < \sqrt{2W^2 + 8\Delta z^2} \\ \left(\frac{W}{2}\right)^2 + \left(\frac{D}{2}\right)^2 + \Delta z^2 & \text{in } (|x|, y) = \left(\frac{W}{2}, 0\right) \quad \text{if } D > \sqrt{2W^2 + 8\Delta z^2} \end{cases} \quad (54) \end{aligned}$$

We can introduce the parameter  $G_{SNR}$  defined as

$$G_{SNR} = \frac{\max_{(x,y)} \left( [R_{TX}R_{RXM}]^2 \right)}{\max_{(x,y)} \left( [R_{TX}R_{RXF}]^2 \right)} \quad (55)$$

which represents the gain in SNR of the forward compared to monostatic receiver in the worst-point of the monitored area in the case of free space model with isotropic antennas.

Substituting eq. (53) and (54) into (55) we obtain:

$$G_{SNR} = \begin{cases} \frac{\left[\left(\frac{W}{2}\right)^2 + D^2 + \Delta z^2\right]^2}{\left[\left(\frac{W}{2}\right)^2 + D^2 + \Delta z^2\right] \left[\left(\frac{W}{2}\right)^2 + \Delta z^2\right]} & \text{if } D < \sqrt{2W^2 + 8\Delta z^2} \\ \frac{\left[\left(\frac{W}{2}\right)^2 + D^2 + \Delta z^2\right]^2}{\left[\left(\frac{W}{2}\right)^2 + \left(\frac{D}{2}\right)^2 + \Delta z^2\right]^2} & \text{if } D > \sqrt{2W^2 + 8\Delta z^2} \end{cases} \quad (56)$$

So  $G_{SNR}$  can be expressed as



$$G_{SNR} = \begin{cases} 1 + \frac{4D^2}{W^2 + 4\Delta z^2} & \text{if } D < \sqrt{2W^2 + 8\Delta z^2} \\ 1 + \frac{3D^2}{W^2 + D^2 + 4\Delta z^2} & \text{if } D > \sqrt{2W^2 + 8\Delta z^2} \end{cases} \quad (57)$$

Let us consider, for example, numerical values with reference to the acquisition campaign described in details in Section 7. We suppose a width  $W = 80 \text{ m}$  for the region to be monitored, a target with height  $z_{TGT} = 0.9 \text{ m}$  and transmitting and receiving antennas with height  $z_0 = 1.25 \text{ m}$ . Figure 47 reports the trend of  $G_{SNR}$  as a function of the length of the baseline  $D$ . As is apparent, the gain in SNR of the forward receiver is always positive. Specifically, the two receivers are comparable (namely  $G_{SNR} \approx 0 \text{ dB}$ ) when  $D \ll W$  whereas by increasing  $D$  with respect to  $W$ ,  $G_{SNR}$  tends to 12 dB.

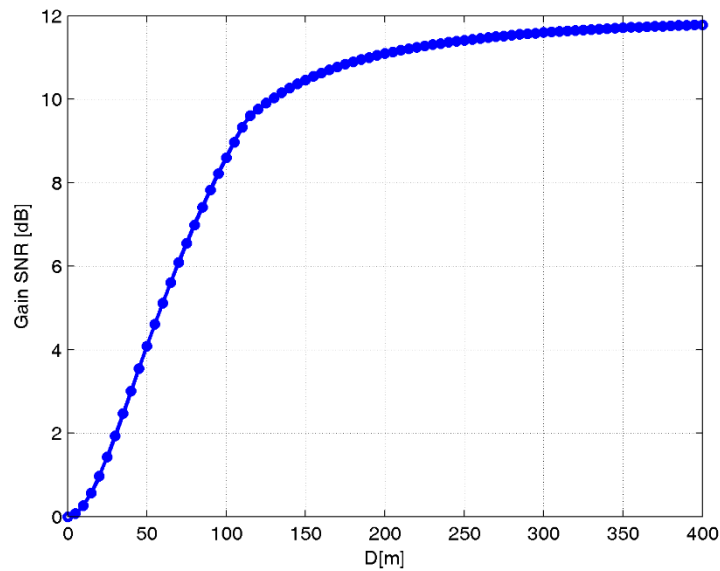


Figure 47. SNR gain of the forward receiver as a function of the length  $D$  of the region to be monitored in the case of Free Space Model.

Therefore, the results in Figure 47 shows that the forward geometry yields a higher target SNR than the monostatic configuration in the worst point of the region to be monitored. This means, for example, that the forward receiver can detect targets with smaller RCS otherwise difficult to be detected using the conventional monostatic radar; moreover by considering the same RCS, the FS radar is characterized by a greater spatial coverage (as a consequence, fewer sensors are necessary to ensure the surveillance of a specific area) or less transmitted power needs to be radiated.

## 8.2. DETECTION PERFORMANCE COMPARISON

Aiming at understanding the performance of the monostatic and forward receivers for applications of vehicles monitoring, a dedicated acquisition campaign has been performed as illustrated in Section 7.

With reference to Figure 40, given the symmetry of the geometry, if a target crosses the baseline  $D$  in the middle, the monostatic and the forward receivers are characterized by the same target to receiver distance [see eq. (51)]. Consequently, the same SNR [see eq. (49)] is obtained for both receivers if we hypothesize that  $G_{TX}$ ,  $G_{RX}$ ,  $P_n$ ,  $\lambda$  and  $P_{TX}$  are the same for the monostatic and forward receivers. Therefore, under these assumptions, the two geometries are fully comparable. For these reasons, in order to evaluate only the effect of the target RCS and effectively verify that the forward geometry yields an enhancement of the RCS compared with the conventional geometries, different tests were performed using more vehicular targets (each one characterized by its own RCS) moving in the surveyed region on a trajectory  $y$  equal to half of the baseline as described in sub-section 7.2.

Also, notice that, aiming at estimating accurately the RCS of each target, each single component of the receiving system has been appropriately selected and optimized in order to guarantee a high SNR. As an example, directional antennas, low noise amplifier with high gain and a maximum power of the transmitter have been used.

### 8.2.1. METHODOLOGY

From Figure 40, we observe that the target moves on a trajectory  $AB$  longer than the baseline. Depending on the target position in the reference plane, we can define three regions as illustrated in Figure 48. Specifically, when  $\beta \approx 180^\circ$ , namely when the target crosses the baseline, it blocks (shadows) part of the direct signal travelling from the transmitting antenna toward the receiving antenna; thus, a reduction in signal strength is registered by the receiver and it represents the target signature (see Figure 41 and Figure 42). The region where is observed a reduction of the direct signal represents the *forward scatter region* (FS region). Then we define *Near-forward scatter region* (NFS region) as the situation in which the target and direct signal are in the same range resolution cell. Namely is verified that the target bistatic range  $R_B$  is less than the direct signal range  $R_D$  (with  $R_D$  equal to the baseline  $D = 40$  m) plus one range resolution cell  $\Delta r$  (in our case, by exploiting a DSSS modulation,  $\Delta r \approx 27$  m). Thus:

$$R_B < D + \Delta r \quad (58)$$

The bistatic range  $R_B$  is the sum of the distance between the transmitter of opportunity and the target,  $R_{TX}$ , and between the target and the forward receiver,  $R_{RX}$ , namely  $R_B = R_{TX} + R_{RX}$ . In our case, given the symmetry of the geometry,  $R_{TX} = R_{RX} = R$  (see Figure 49). Therefore,  $R_B = 2R$ . With reference to Figure 49, assuming  $W_{NFS}$  as the width of the NFS region, we have that

$$R_B = 2R = 2 \sqrt{\left(\frac{D}{2}\right)^2 + \left(\frac{W_{NFS}}{2}\right)^2} \quad (59)$$

Substituting eq. (59) in (58), we obtain that  $W_{NFS} \approx 54$  m.

Finally, the other locations of the target in the plane correspond to the *High-bistatic angles region*.

Aiming at exploiting the advantages of the forward scatter operation mode observed at very high bistatic angles ( $\beta \approx 140^\circ$ - $180^\circ$ ), in this work we are interested to compare monostatic and forward configurations

especially in NFS region. However, for a complete analysis we will consider also the high-bistatic angles region. Therefore, the FS region will be excluded from our analysis. In fact, with reference to the WiFi processing scheme in Figure 1, the reduction of the direct signal in the forward receiver when the target crosses the baseline might prevent the correct estimation of the cancellation filter weights. Consequently, the target might be included in the cancellation filter notch yielding to a partial cancellation of the target return and consequently to a limitation in detection.

Thus, for a fair comparison between the two configurations, the FS region will not be considered. However, as it was shown in the following, its temporal and spatial extension is smaller than the other regions. Moreover, it is worth to note that there are ad-hoc techniques that can be used for target detection in this region.

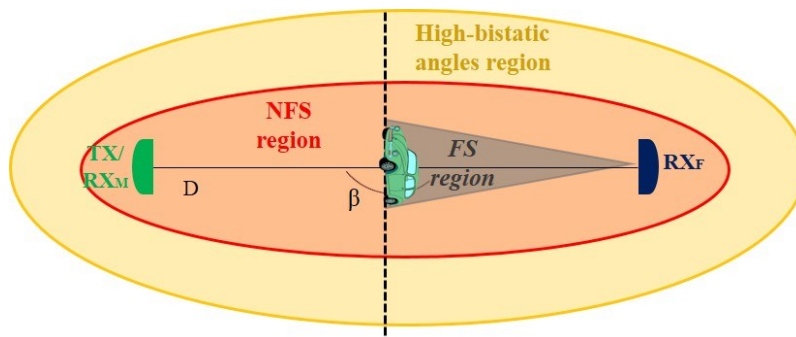


Figure 48. Regions defined by the forward receiver during the target trajectory.

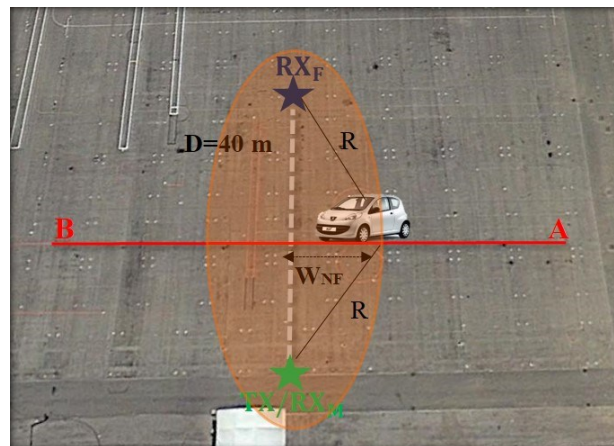


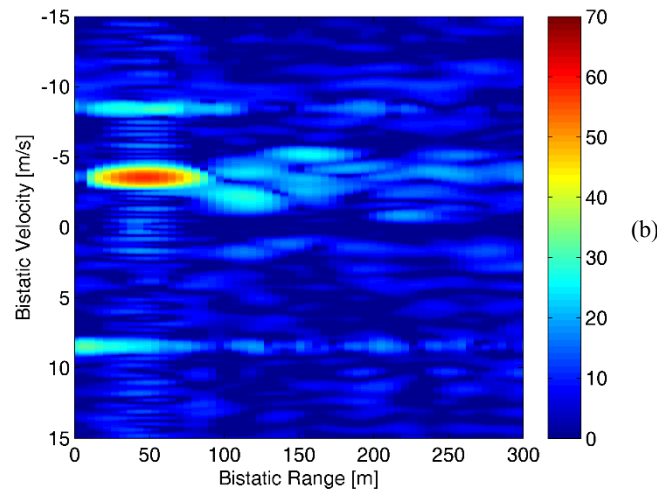
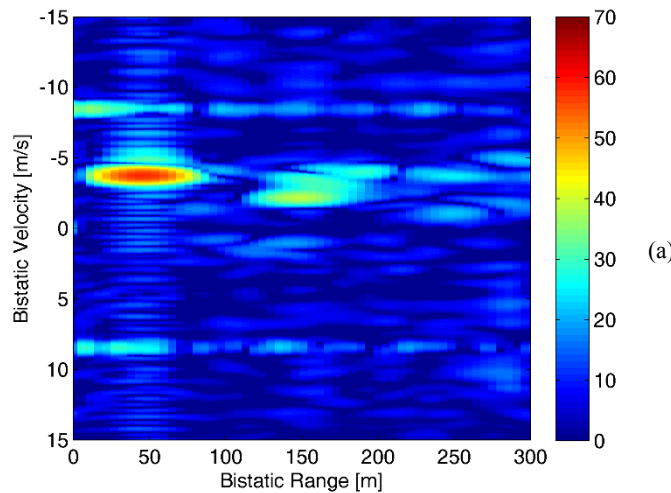
Figure 49. Concept of Near-Forward region.

### 8.2.2. RCS ENHANCEMENT ANALYSIS

The optimized WiFi-based passive radar processing scheme for target detection depicted in Figure 1 has been applied against the collected surveillance signals separately at each receiving channel. In particular, the same processing parameters applied against the forward receiver (shown in sub-section 7.2) have been used. Therefore, the cancellation stage has been performed by adopting the ECA-S over a range of 500 m

(i.e.  $K = 36$  taps @  $f_s = 22\text{MHz}$ ) with  $T_B = 0.1\text{ s}$  and  $T_s = 3\text{ ms}$ . Then a CPI of  $0.1\text{ s}$  is used to evaluate the bistatic range-velocity maps.

As an example, Figure 50 shows the range-velocity maps obtained after disturbance cancellation and sidelobe control for the same tests considered in Figure 41 and Figure 42. All the reported maps have been normalized to thermal noise power level so that the value at each map location represents the estimated SNR. Specially, Figure 50(a)-(b) report the range-velocity maps for the monostatic and forward receivers, respectively, for a test with the Fiat Punto Evo as target. As it is apparent, in both cases the target has been detected (because we are in high SNR condition); moreover, by considering the symmetric configuration between monostatic and forward antennas (as shown in Figure 40), in both cases the target appears as a strong peak at about  $43\text{ m}$  and  $-3.7\text{ m/s}$ . In addition, further peaks are also visible caused by the double bounce reflection of the target echo over the metallic fence delimiting the parking area. Figure 50(c)-(d) shows the case of a test with the Peugeot 107 as moving target for the monostatic and forward receivers for a different position of the target along its trajectory with respect to Figure 50(a)-(b). We notice as also in this case the target has been detected in both receivers and its peak appears at about  $48\text{ m}$  and  $4.5\text{ m/s}$ . Notice that, in such geometry, the target describes a parabolic trajectory on the bistatic range-velocity plane; so it appears at positive velocity location when it moves approaching the point  $(0,0)$ , while it appears at negative velocity location when it moves away from  $(0,0)$ .



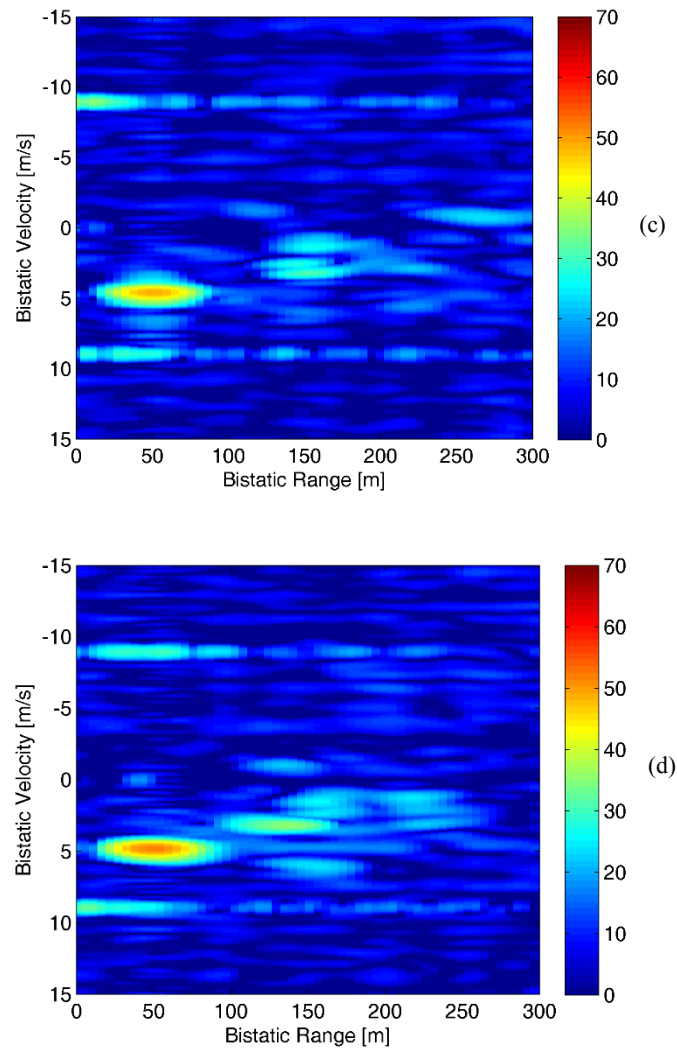


Figure 50. Range-Velocity maps for the same tests of Figure 41. (a)-(b) Fiat Punto Evo for monostatic and forward receiver, respectively. (c)-(d) Peugeot 107 for monostatic and forward receiver, respectively.

According to the processing scheme sketched in Figure 1, the detection stage follows the evaluation of the range-velocity map. Also in this case, the same detection parameters adopted in Section 7 have been used. Thus, a CPI of 0.1 s is used to evaluate the bistatic range-velocity map over consecutive portions of the acquired signals (frames) with a fixed displacement of 0.1 s (10 frames per second are thus obtained); finally, target detection is performed by resorting to a standard cell-average CFAR threshold with a probability of false alarm  $P_{fa}$  equal to  $10^{-4}$ . Notice that this value of  $P_{fa}$  has been chosen aiming to target detection and its RCS estimation on both receivers.

As an example, Figure 51 shows all the plots collected over the whole acquisition time for the two tests reported in Figure 50. Figure 51(a)-(c) show the detection of the monostatic receiver for the Fiat Punto Evo and Peugeot 107, respectively, while Figure 51(b)-(d) the detection of the forward sensor for the same tests. Notice that, Figure 51(b)-(d) correspond to Figure 43. As it is apparent, in both receivers, we have not only target detection but also false alarms and multipath effects. We also note that the symmetric configurations produce very similar target detection in both receivers. For illustration purposes, the red line in Figure 51 defines the NFS region.

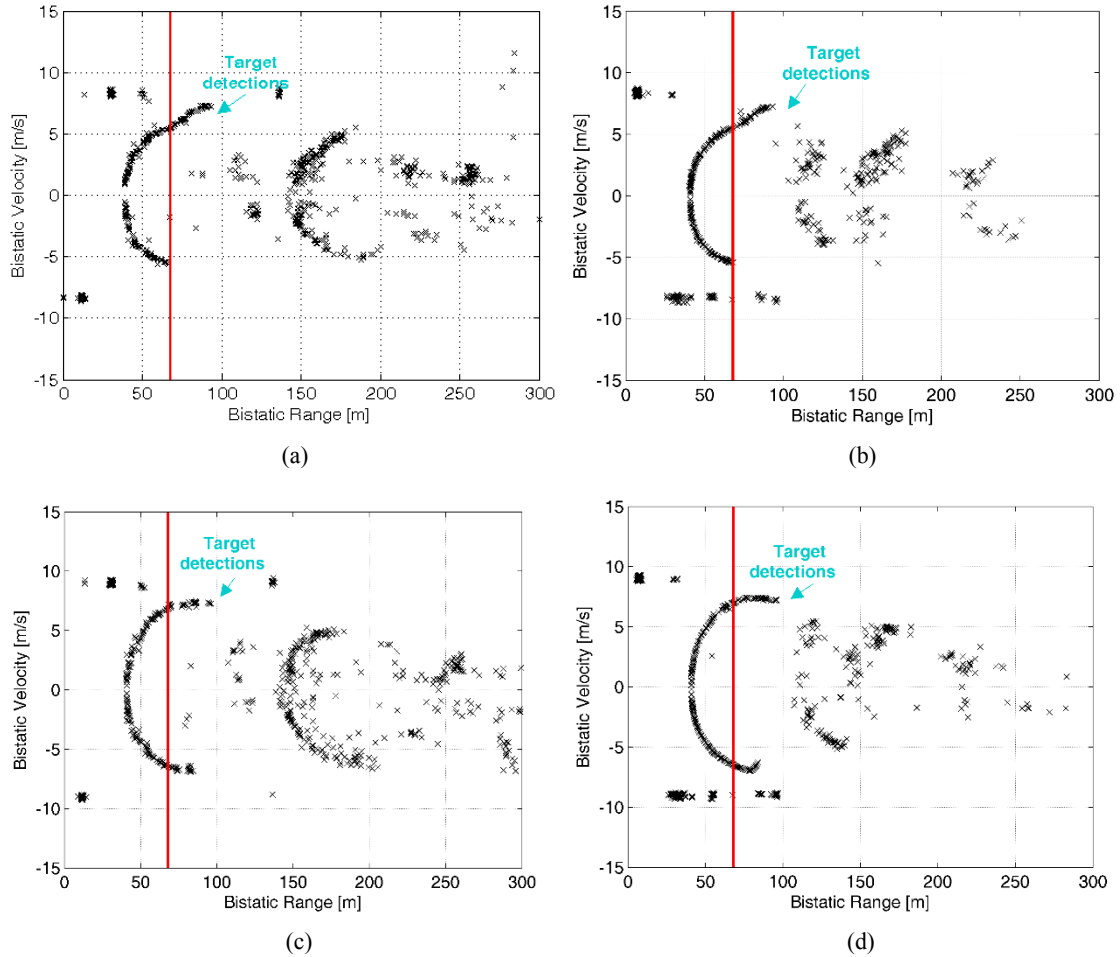
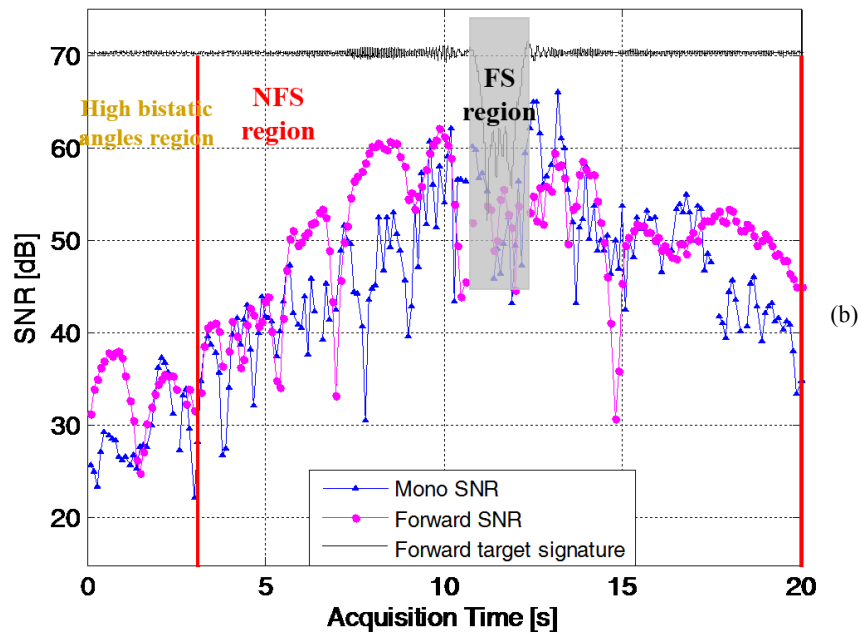
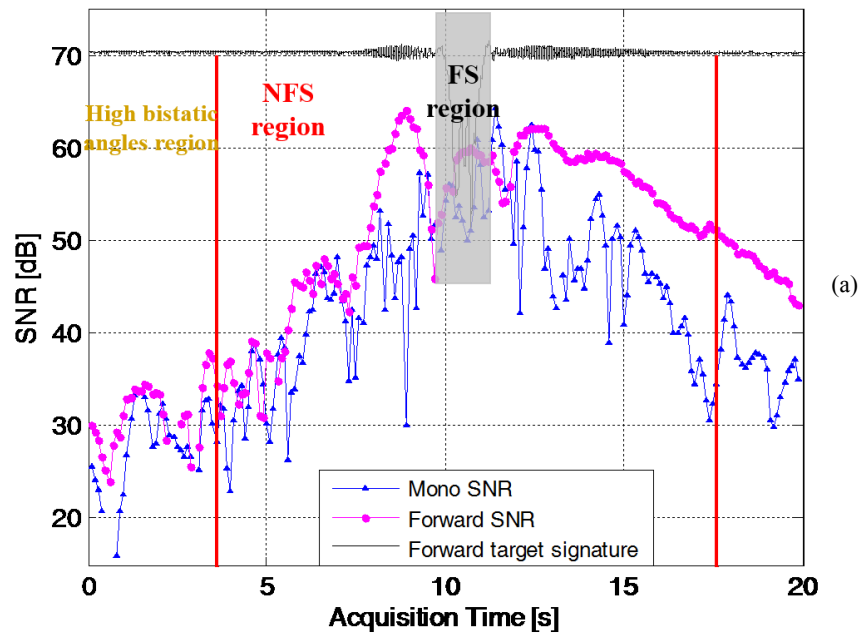


Figure 51. Detections over the range-velocity plane for the same tests in Figure 50. (a)-(b) Monostatic and forward receiver, respectively, for the test with a Fiat Punto Evo. (c)-(d) Monostatic and forward receiver, respectively, for the test with a Peugeot 107.

Aiming at estimate the target RCS on both configurations, for each performed test, at each frame we store the SNR value of the detected plots along the whole acquisition time (from 15 s to 20 s depending on the test). As an example, Figure 52 shows in blue and magenta curves the monostatic and forward SNR trends along the acquisition time of four different tests each one referring to different car model. In addition, the time intervals corresponding to NFS and High-bistatic angles regions have been highlighted. Then, the forward target signature is reported in black in order to identify the FS region; we observe as the forward region extension is significantly smaller than the other regions.

We notice in Figure 52 that the forward receiver yields an increase of the average SNR not only in the NFS region but also in the High-bistatic angles region; this is visible for all the tests reported. Similar results could be also shown for all the other experiments. Since it has been experimentally verified that the two receivers are characterized by a comparable noise power, the results in Figure 52 show as effectively the forward geometry produces an enhancement of the target SNR, namely, an enhancement of the target RCS compared to monostatic radar.





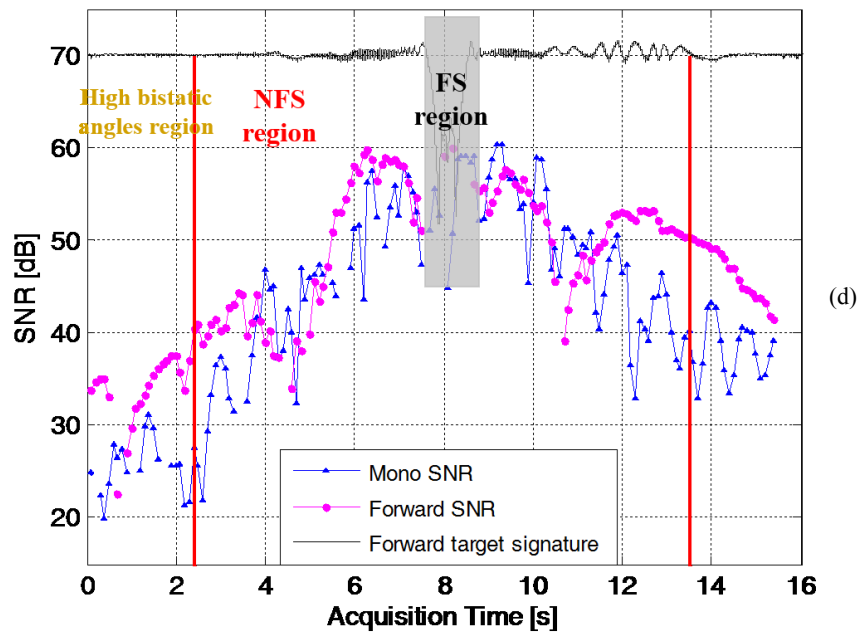
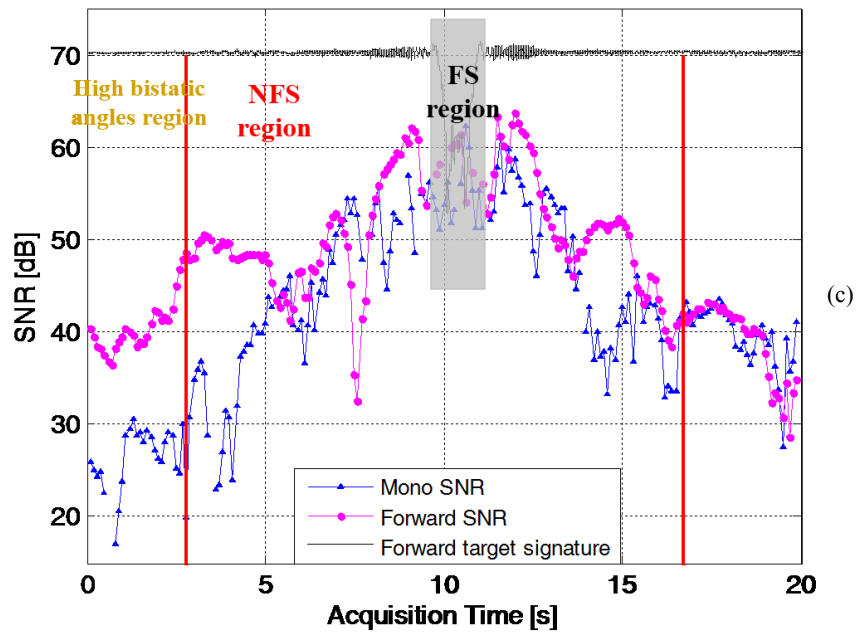


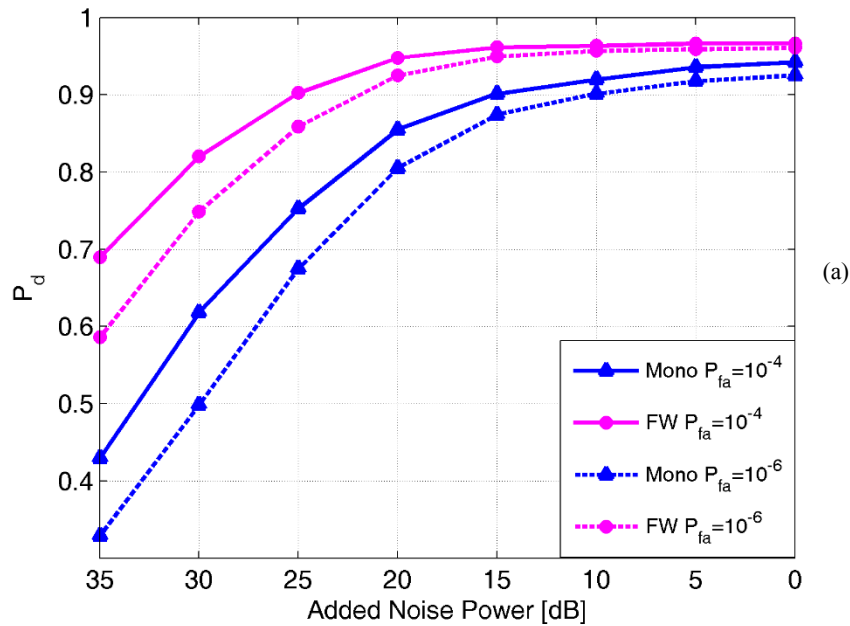
Figure 52. SNR trends of the different vehicles used in the acquisition campaign: (a) Peugeot 107; (b) Fiat Punto Evo; (c) Citroen C3; (d) Volkswagen Polo.

### 8.2.3. TARGET DETECTION CAPABILITY ANALYSIS

In this sub-section, both receivers are compared in target detection capability. The adopted criteria has been to sum the detections of all available tests and calculate a mean value of probability of detection  $P_d$ .

Due to the fact that we are in high SNR condition, the number of detections obtained with the monostatic receiver and the forward receiver are comparable (see Figure 53). For these reasons, we have added zero mean complex Gaussian white noises to the original data in order to be in low SNR conditions. Specifically, different values of added noise power  $P_{n_{add}}$  have been considered.

Figure 53 shows the  $P_d$  of both receivers as a function of the added noise power for  $P_{fa} = 10^{-4}$  and  $P_{fa} = 10^{-6}$ . Specifically Figure 53 (a) refers to the detections of the only NFW region whereas Figure 53(b) to the detections of the NFW region plus High-bistatic angles; in both cases, we remember that the detections of FS region have not be considered. The case  $P_{n_{add}} = 0 \text{ dB}$  corresponds to the case of high SNR conditions: we observe that the forward receiver provides very similar detection performance with respect to monostatic receiver. In contrast, remarkable probability of detection of the forward geometry can be obtained in the case of low SNR condition. As an example, in the case of  $P_{n_{add}} = 35 \text{ dB}$  and  $P_{fa} = 10^{-4}$ , the forward detection probability of the NFW region is about 0.7 [see Figure 53(a)] against 0.43 of the monostatic receiver. Obviously, the detection enhancement of the forward configuration derives by the enhancement of the target RCS compared to monostatic radar.



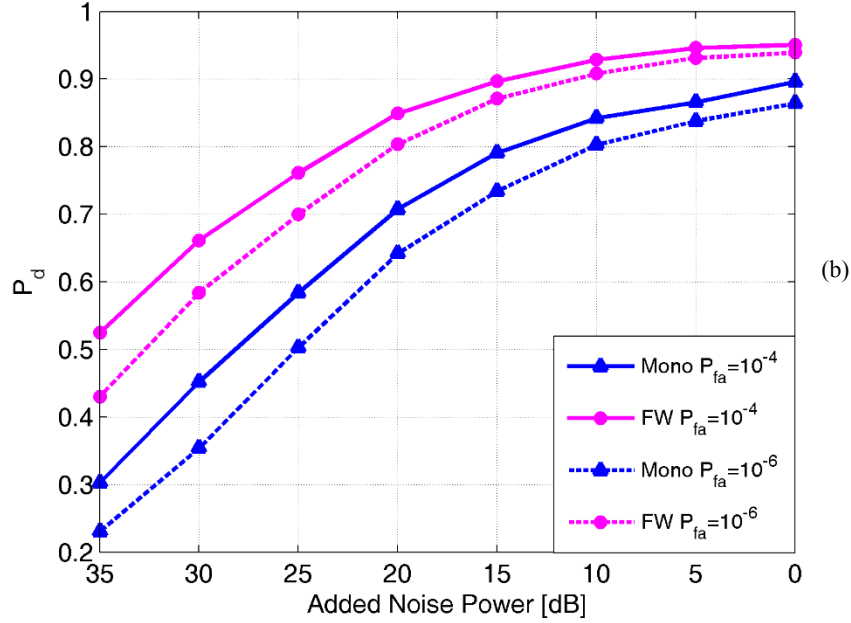


Figure 53. Probability of detection  $P_d$  (obtained as sum of all the acquisitions) as a function of the added noise power for  $P_{fa} = 10^{-4}$  and  $P_{fa} = 10^{-6}$ . (a) Detection of the Near Forward region; (b) Detection of the Near Forward region plus High Bistatic angles region.

### 8.3. CONSIDERATIONS ABOUT THE COMPUTATIONAL LOAD SAVING AND SYSTEM COMPLEXITY REDUCTION IN FW GEOMETRY

In this sub-section, considerations about the computational load saving and system complexity reduction in FW geometry are taken in account.

#### 8.3.1. ANALYSIS ON THE REGION EXTENSION OF THE SURVEYED AREA

Whilst so far the analysis has been performed using the same range-velocity map extension, aiming at the coverage of a specific area as defined in Figure 46, the forward configuration potentially allows a reduction of the maximum bistatic range to be included in the observed range-Doppler map as illustrated in the following.

After the target detection stage, the PBR sensor provides an estimation of the target velocity and range. In particular, the bistatic range  $R_B$  is the sum of the distance between the transmitter of opportunity and target,  $R_{TX}$ , and between the target and receiver,  $R_{RX}$ , namely  $R_B = R_{TX} + R_{RX}$ . In our case

$$R_{BM} = R_{TX} + R_{RXM} \quad ; \quad R_{BF} = R_{TX} + R_{RXF} \quad (60)$$

represent the bistatic ranges for the monostatic and forward receivers, respectively. Substituting eq. (53) into (60), the bistatic ranges become:



$$\begin{aligned}
 R_{BM} &= 2 \sqrt{x^2 + \left(y + \frac{D}{2}\right)^2 + \Delta z^2} \\
 R_{BF} &= \sqrt{x^2 + \left(y + \frac{D}{2}\right)^2 + \Delta z^2} + \sqrt{x^2 + \left(y - \frac{D}{2}\right)^2 + \Delta z^2}
 \end{aligned} \tag{61}$$

Consequently, with reference to Figure 46, the minimum and maximum bistatic range in both configurations are:

$$\text{Monostatic case: } \begin{cases} \min_{(x,y)} R_{BM} = 2 \Delta z & \text{in } (x, y) = \left(0, -\frac{D}{2}\right) \\ \max_{(x,y)} R_{BM} = 2 \sqrt{\left(\frac{W}{2}\right)^2 + D^2 + \Delta z^2} & \text{in } (|x|, y) = \left(\frac{W}{2}, \frac{D}{2}\right) \end{cases} \tag{62}$$

$$\text{Forward case: } \begin{cases} \min_{(x,y)} R_{BF} = 2 \sqrt{\left(\frac{D}{2}\right)^2 + \Delta z^2} & \text{in } (x, y) = (0, 0) \\ \max_{(x,y)} R_{BF} = \sqrt{\left(\frac{W}{2}\right)^2 + D^2 + \Delta z^2} + \sqrt{\left(\frac{W}{2}\right)^2 + \Delta z^2} & \text{in } (|x|, y) = \left(\frac{W}{2}, \frac{D}{2}\right) \end{cases} \tag{63}$$

Specifically, it is interesting to evaluate the range extension  $\Delta R$  defined as  $\Delta R = R_{B_{max}} - R_{B_{min}}$ . For both receivers, we obtain:

$$\Delta R_M = \max_{(x,y)} R_{BM} - \min_{(x,y)} R_{BM} = 2 \sqrt{\left(\frac{W}{2}\right)^2 + D^2 + \Delta z^2} - 2 \Delta z \tag{64}$$

$$\Delta R_F = \max_{(x,y)} R_{BF} - \min_{(x,y)} R_{BF} = \sqrt{\left(\frac{W}{2}\right)^2 + D^2 + \Delta z^2} + \sqrt{\left(\frac{W}{2}\right)^2 + \Delta z^2} - 2 \sqrt{\left(\frac{D}{2}\right)^2 + \Delta z^2} \tag{65}$$

As done before, the parameter  $G_{range} = \frac{\Delta R_M}{\Delta R_F}$  can be introduced that represents the gain in bistatic range extension of the monitored region using the forward receiver in comparison with the monostatic geometry. Substituting (64) and (65):

$$\begin{aligned}
 G_{range} &= \frac{\Delta R_M}{\Delta R_F} = \frac{2 \sqrt{\left(\frac{W}{2}\right)^2 + D^2 + \Delta z^2} - 2 \Delta z}{\sqrt{\left(\frac{W}{2}\right)^2 + D^2 + \Delta z^2} + \sqrt{\left(\frac{W}{2}\right)^2 + \Delta z^2} - 2 \sqrt{\left(\frac{D}{2}\right)^2 + \Delta z^2}} = \\
 &= \frac{2 \left[ \sqrt{\left(\frac{W}{2\Delta z}\right)^2 + \left(\frac{D}{\Delta z}\right)^2 + 1} - 1 \right]}{\sqrt{\left(\frac{W}{2\Delta z}\right)^2 + \left(\frac{D}{\Delta z}\right)^2 + 1} + \sqrt{\left(\frac{W}{2\Delta z}\right)^2 + 1} - 2 \sqrt{\left(\frac{D}{2\Delta z}\right)^2 + 1}}
 \end{aligned} \tag{66}$$

As done for  $G_{SNR}$  in (57), supposing  $W = 80$  m,  $z_{TGT} = 0.9$  m and  $z_0 = 1.25$  m, Figure 54 reported the trend of  $G_{range}$  as a function of the length of the baseline  $D$ . We note that  $G_{range}$  is also always positive, this means that the forward configuration allows to reducing the range extension of the specific area to be surveilled. As an example, the case  $W = D = 80$  m yields a forward range extension reduction by a factor 3.6 with respect to the monostatic case. Notice that the reduction of the forward range extension implies a minor amount of data to be managed; therefore, it might enable a corresponding reduction in the computational load of the processing. Obviously, the two configurations become comparable when  $W \gg D$ , in this case we obtain an unitary gain.

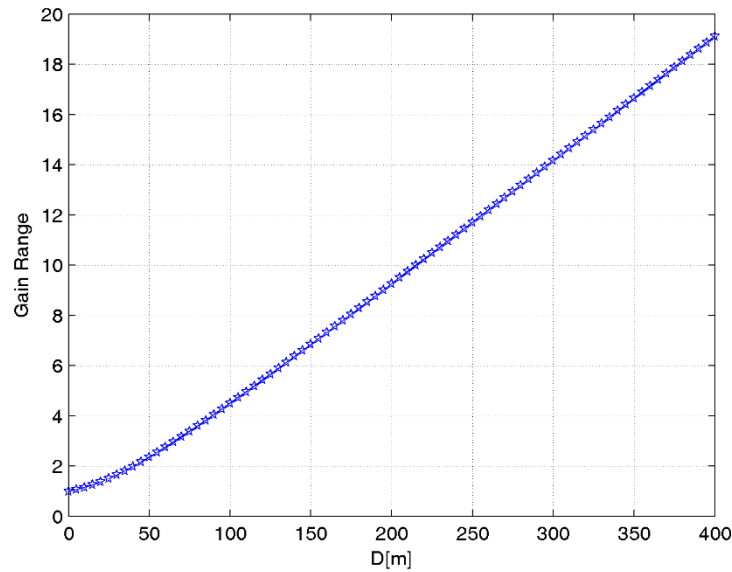


Figure 54. Bistatic range gain as a function of the length  $D$  of the region to be monitored.

### 8.3.2. ANALYSIS ON THE NUMBER OF TAPS OF THE CANCELLATION STAGE

The number of taps highly affects the complexity of the cancellation stage as it sets the dimension of the matrix to be estimated and inverted, as well as the dimension of the filter to be evaluated and applied [see eq. (23)].

In forward configuration, the direct signal transmitted by the transmitting antenna appears at a bistatic range equal to the baseline (as an example, see Figure 41) differently from the monostatic receiver where the direct signal bistatic range is 0 m. Therefore, the number of taps could be potentially reduced in the forward receiver if a small detection loss can be accepted. As an example, Figure 55 reports the  $P_d$  of both receivers as a function of the number of taps of the cancellation stage for  $P_{fa} = 10^{-4}$  and  $P_{fa} = 10^{-6}$ . Specifically, Figure 55(a) refers to the detections of the only NFW region whereas Figure 55(b) to the detections of the NFW region plus High-bistatic angles. Following the same criteria adopted before, the detections of all available tests have been sum in order to obtain a mean value of  $P_d$ .

Based on the reported results, we observe that in FW configuration a smaller number of taps are needed to obtain approximately the same  $P_d$  of the monostatic receiver. Obviously, reducing the number of taps yields a corresponding computational load reduction.

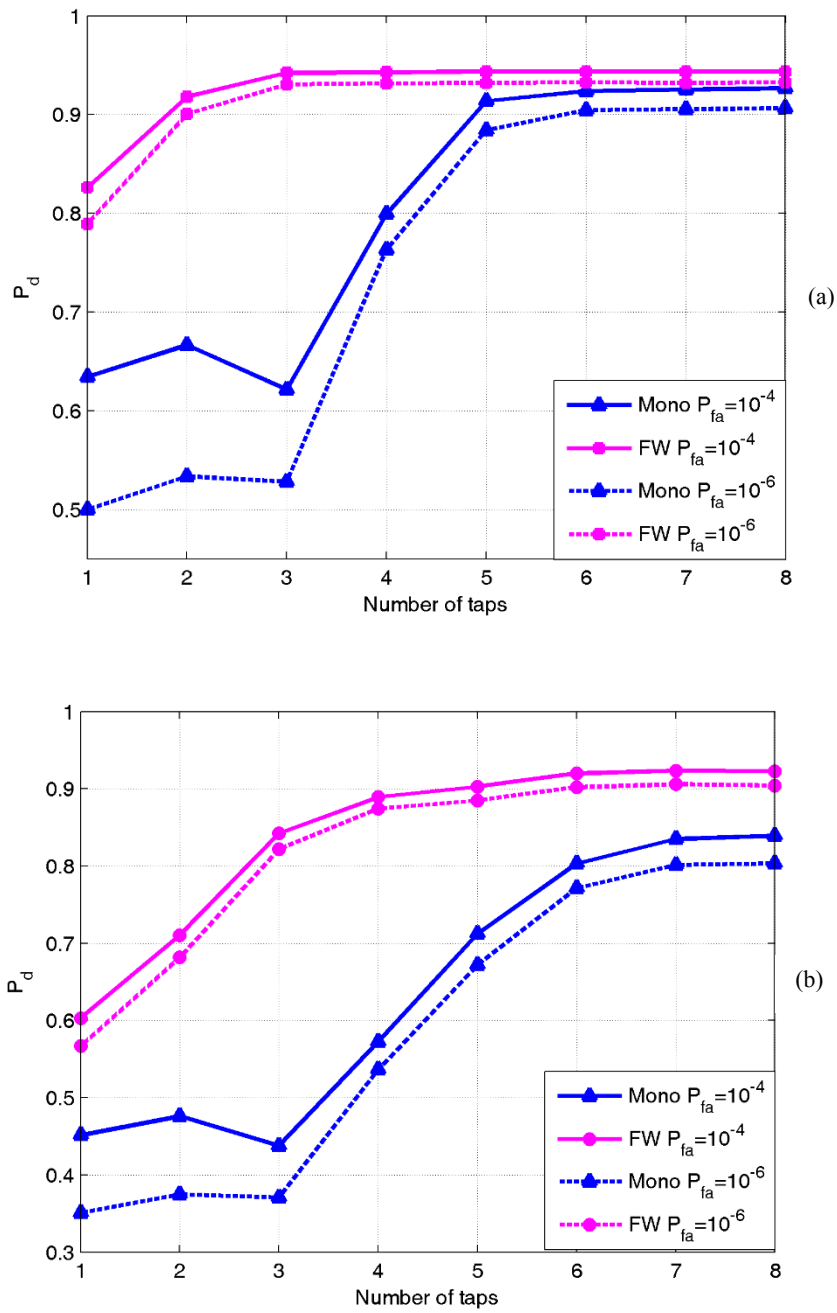


Figure 55. Probability of detection  $P_d$  (obtained as sum of all the acquisitions) as a function of the number of taps of the cancellation stage for  $P_{fa} = 10^{-4}$  and  $P_{fa} = 10^{-6}$ . (a) Detection of the Near Forward region; (b) Detection of the Near Forward region plus High Bistatic angles region.





## 9. CONCLUSIONS

The results reported in this work provide a demonstration of the wide potentialities of a WiFi-based passive radar. Specifically, this work concerned the design of proper processing strategies able to overcome the limitations of the existing WiFi-based PBR and to provide the sensor of new advanced potentialities in order to extend the range of possible applications.

First of all, in this work it has been shown that the existing disturbance cancellation technique, known as ECA-B, might yield some limitations when employed against highly time disturbance scenarios in the presence of slowly moving targets. In fact, unwanted structures could appear on the target echo in the Doppler dimension at the output of the cancellation stage and they can be responsible of useful dynamic range reduction or masking effect over weak targets. Aiming at counteracting these limitations, an enhanced version of the disturbance cancellation technique (ECA-S) has been presented. The experimental results show that the ECA-S approach allows a better trade-off between disturbance cancellation and the capability to preserve low-Doppler target echoes thus improving the detection performance of the resulting PBR system.

Although an optimization of the disturbance cancellation technique has been proposed, however all ECA versions distort the target spectrum at very low Doppler frequency by inserting a cancellation notch. Thus, the background removal can have a non negligible effect on the target signal in input to the ISAR processing thus it might reduce the quality of the ISAR products. Therefore, in this work, an enhanced ISAR profiling technique has been proposed suitable for the simultaneous rejection of the background disturbance (stationary scene, multipath, etc etc) and profiling of the target. By using this technique, reliable and stable profiles of moving man-made objects are achieved with a cross-range resolution up to about 10 cm. This has been shown in this work with reference to an experimental test including two identical cars (i.e. Fiat Punto Evo). This allowed us to preliminary verify that these profiles could be exploited for classification purposes.

In order to extend the range of applications, the potentialities of a WiFi-based passive radar have been investigated for indoor area monitoring. It has been shown that human targets moving in indoor environment can be detected and accurately localized by exploiting proper multistatic geometries with few receiving antennas. Additionally, in order to improve the resolution capabilities of the proposed system, suitable ISAR techniques have been introduced to allow the achievement of high resolution cross-range profiles of the detected targets. The application of ISAR techniques against the echoes from human targets moving indoor clearly show the improved resolution capabilities which could enable the separation of closely spaced targets, otherwise not separable. The obtained results are also important for the research activities carried out within the European project SOS. In fact the increase of the passive radar resolution allows a significant improvement in the quality of the passive radar localization thus demonstrating that the WiFi-based PBR sensor can be successfully employed (with other active and passive sensors) for detecting and tracking suspicious people within the terminal area of the airport.

Therefore, the proposed sensor could be successfully employed as an automatic, low-cost, compact, and non-intrusive sensor to improve safety and security in different scenarios with limited impact on its users. This is also confirmed by the results shown in this work where the suitability of the WiFi-based PBR has been investigated for a civil application related to small airfield monitoring. The tests performed in a real scenario have proven the capability of the passive sensor to detect and accurately track typical users of the airfield, there including small or ultralight aircrafts, ground vehicles, and people.

Finally, the feasibility of non-conventional geometries has been investigated. In particular, the impact of the Forward geometry on a WiFi-based PBR has been experimentally evaluated for the first time. The

results proves that the Forward configuration yields an enhancement in target SNR (which allows a gain in target detection) compared with the monostatic geometry. Moreover, the possibility to employ a WiFi passive radar in forward scatter configuration for vehicle classification has been investigated. Preliminary results against the collected data set shown that different targets yield quite different vehicular signatures. This suggested us to exploit these signatures in a classification stage where a minimum Euclidean distance criteria has been adopted to evaluate the similarity among different car models. The results shown very good capability of the proposed system to correctly associate a vehicle signature to its car model. Therefore, the proposed system can be employed for applications of vehicle monitoring.

In conclusion, the results shown in this work support the practical applicability of the WiFi-based passive radar concept in solving real world problems. In particular, the possibility to provide passive radar surveillance by exploiting such a ubiquitous and easily accessible source of opportunity, offers major opportunities to improve interior and exterior security for all types of buildings and to identify and track goods and people.



## PUBLICATIONS

### INTERNATIONAL JOURNALS

- J1. F. Colone, T. Martelli, C. Bongioanni, D. Pastina, and P. Lombardo, "WiFi-based PCL for monitoring private airfields", *IEEE Aerospace and Electronic Systems Magazine*, [accepted with minor revision].
- J2. F. Colone, C. Palmarini, T. Martelli, and E. Tilli, "Sliding Extensive Cancellation Algorithm (ECA-S) for disturbance removal in passive radar," *IEEE Transactions on Aerospace and Electronic Systems*, [in print].
- J3. D. Pastina, F. Colone, T. Martelli, and P. Falcone, "Parasitic exploitation of WiFi signals for indoor radar surveillance," *IEEE Transaction on Vehicular Technology*, vol.64, no.4, pp.1401,1415, April 2015.

### CONFERENCE PROCEEDINGS

- C1. T. Martelli, F. Colone, C. Bongioanni, D. Pastina, and P. Lombardo, "Short-range passive radar for small private airports surveillance", accepted in *European Radar Conference (EURAD) 2016, London, UK, 2016*.
- C2. T. Martelli, C. Bongioanni, F. Colone, P. Lombardo, L. Testa, and A. Meta, "Security enhancement in small private airports through active and passive sensors," accepted in *International Radar Symposium (IRS) 2016, Krakow, Poland, May 2016*.
- C3. T. Martelli, F. Colone, and P. Lombardo, "First experimental results for a WiFi-based Passive Forward Scatter Radar," accepted in *IEEE Radar Conference (RadarCon)2016, Philadelphia, USA, May 2016*.
- C4. C. Palmarini, T. Martelli, F. Colone, and P. Lombardo, "Disturbance removal in passive radar via Sliding Extensive Cancellation Algorithm (ECA-S)," *South African Radar Conference 2015, Johannesburg, South Africa, October 2015*.
- C5. T. Martelli, D. Pastina, F. Colone, and P. Lombardo, "Enhanced WiFi-based passive ISAR for indoor and outdoor surveillance," *IEEE Radar Conference (RadarCon) 2015, Washington, USA, May 2015*.
- C6. A. Macera, C. Bongioanni, F. Colone, C. Palmarini, T. Martelli, D. Pastina, and P. Lombardo, "FM-based Passive Bistatic Radar in ARGUS 3D: Experimental Results," *GTTi 2013 - Riunione Annuale, Ancona, Italy, 24-26 Giugno 2013*.

## TECHNICAL REPORTS

- T1. Deliverable D5.1 of the SOS (Sensors system for detection and tracking Of dangerous materials in order to increase the airport Security in the indoor landside area) European project co-funded by the European Commission within the FP7, Grant agreement no. 286105. Mid-Term report, December 2013.

## REFERENCES

- [1] A. Hac, *Wireless sensor network design*, John Wiley & Sons, 2003.
- [2] A. Chen, S. Kumar, and T.H. Lai, "Local Barrier Coverage in Wireless Sensor Networks," in *IEEE Transactions on Mobile Computing*, vol.9, no.4, pp.491-504, April 2010.
- [3] H. Liu, H. Darabi, P. Banerjee, and L. Jing, "Survey of Wireless Indoor Positioning Techniques and Systems," *IEEE Transactions on Systems, Man, and Cybernetics, Part C: Applications and Reviews*, vol.37, no.6, pp.1067–1080, Nov. 2007.
- [4] M. Antoniou, V. Sizov, Hu Cheng; P. Jancovic, R. Abdullah, N.E.A. Rashid, and M. Cherniakov, "The concept of a forward scattering micro-sensors radar network for situational awareness," in *International Conference on Radar, 2008*, vol., no., pp.171-176, 2-5 Sept. 2008.
- [5] T. Sanpechuda and L. Kovavisaruch, "A review of RFID localization: Applications and techniques," in *Proc. IEEE Int. Conf. Electr.Eng./Electron. Comput. Telecommun. Inf. Technol.*, May 2008, pp. 769–772.
- [6] D. Dardari, R. D'Errico, C. Roblin, A. Sibille, and M.Z. Win, "Ultrawide Bandwidth RFID: The Next Generation?," in *Proc. IEEE*, vol.98, no.9, Sept. 2010.
- [7] P. Howland, "Special Issue on Passive Radar Systems," *IEE Proceedings on Radar, Sonar and Navigation*, Vol. 152, Issue 3, June 2005.
- [8] A. Farina and H. Kuschel, Special Issue on Passive Radar (Part I&II) – *IEEE Aerospace and Electronic Systems Magazine*, vol. 27, no. 10-11, 2012
- [9] P. Lombardo and F. Colone, "Advanced processing methods for passive bistatic radar systems," in *Principles of Modern Radar: Advanced Radar Techniques*, W. L. Melvin, and J. A. Scheer, Raleigh, NC: SciTech Publishing, 2012.
- [10] P.E. Howland, D. Maksimiuk, G. Reitsma, "FM radio based bistatic radar", *IEEE Proceedings on Radar, Sonar and Navigation*, Vol. 152, Issue 3, June 2005, pp. 107–115.
- [11] F. Colone, C. Bongioanni, and P. Lombardo, "Multi-Frequency Integration in FM Radio Based Passive Bistatic Radar. Part I: Target Detection," *IEEE Aerospace and Electronic Systems Magazine*, vol. 28, no. 4, 2013.
- [12] F. Colone, C. Bongioanni, and P. Lombardo, "Multi-Frequency Integration in FM Radio Based Passive Bistatic Radar. Part II: Direction of Arrival Estimation," *IEEE Aerospace and Electronic Systems Magazine*, vol. 28, no. 4, 2013.
- [13] H.D. Griffiths, N.R. Long, "Television based bistatic radar", *IEE Proc. F, Commun. Radar Sig. Proc.*, 133(7), 1986, pp. 649–657.
- [14] P.E. Howland, "Target tracking using television-based bistatic radar", *IEE Proceedings on Radar, Sonar and Navigation*, Vol. 146, Issue 3, 1999, pp. 166–174.
- [15] G. Fabrizio, F. Colone, P. Lombardo, and A. Farina, "Adaptive beam forming for high frequency over-the-horizon passive radar," *IET Radar, Sonar & Navigation*, Vol. 3, Issue 4, August 2009, pp. 384-405.

- [16] J.M. Thomas, H.D. Griffiths and C.J. Baker, “Ambiguity function analysis of digital radio mondiale signals for HF passive bistatic radar”, *Electronics Letters*, vol. 42, pp 1482-1483, Dec. 2006.
- [17] D. Poullin, “Passive detection using broadcasters (DAB, DVB) with CODFM modulation”, *IEE Proceedings on Radar, Sonar and Navigation*, Vol. 152, Issue 3, June 2005, pp. 143–152.
- [18] R. Saini and M. Cherniakov, “DTV signal ambiguity function analysis for radar application”, *IEE Proceedings on Radar, Sonar and Navigation*, Vol. 152, Issue 3, June 2005, pp. 133-142.
- [19] C. Coleman and H. Yardley, “Passive bistatic radar based on target illuminations by digital audio broadcasting,” *IET Radar, Sonar and Navigation*, vol. 2, Issue 5, Oct. 2008.
- [20] F. Colone, D. Langellotti, and P. Lombardo, "DVB-T signal ambiguity function control for passive radars," *IEEE Trans. on Aerospace and Electronic Systems*, vol.50, no.1, Jan. 2014.
- [21] H. Kuschel, M. Ummerhofer, D. O'Hagan, J. Heckenbach, "On the resolution performance of passive radar using DVB-T illuminations," in *International Radar Symposium (IRS), 2010*, vol., no., pp.1-4, 16-18 June 2010.
- [22] D. Tan, H. Sun, Y. Lu, M. Lesturgie, and H. Chan, “Passive Radar Using Global System for Mobile Communication Signal: Theory, Implementation and Measurements,” *IEE Proceedings on Radar, Sonar and Navigation*, vol. 152, no. 3, pp. 116–123, June 2005.
- [23] Sun, H., Tan, D.K.P., Yilong Lu & Lesturgie, M., "Applications of passive surveillance radar system using cell phone base station illuminators", *IEEE Aerospace and Electronic Systems Magazine*, vol. 25, no. 3, 2010, pp. 10-18.
- [24] Krysik, P., Samczynski, P., Malanowski, M., Maslikowski, L. & Kulpa, K.S., "Velocity measurement and traffic monitoring using a GSM passive radar demonstrator", *IEEE Aerospace and Electronic Systems Magazine*, vol. 27, no. 10, 2012, pp. 43-51.
- [25] R. Zemhari, U. Nickel, and W.D. Wirth, “GSM Passive Radar for Medium Range Surveillance,” in *Proceedings of European Radar Conference*, Rome, Italy, September 30–October 2, 2009.
- [26] Wang, Q., Hou, C. & Lu, Y., "An experimental study of WiMAX-based passive radar", *IEEE Trans. on Microwave Theory and Techniques*, vol. 58, no. 12 (Part 1), 2010, pp. 3502-3510.
- [27] Chetty, K., Woodbridge, K., Guo, H. & Smith, G.E., "Passive bistatic WiMAX radar for marine surveillance", *IEEE National Radar Conference 2010*, pp. 188-193, Washington D.C. (USA), May 2010, pp. 188–193.
- [28] Colone, F., Falcone, P., and Lombardo. P., “Ambiguity Function Analysis of WiMAX Transmissions for Passive Radar,” *IEEE Int. Radar Conference*, Washington, DC, May 10–14, 2010.
- [29] A.A. Salah, R.S.A.R. Abdullah, A. Ismail, F. Hashim, C.Y. Leow, M.B. Roslee, and N.E.A. Rashid, "Feasibility study of LTE signal as a new illuminators of opportunity for passive radar applications," in *IEEE International RF and Microwave Conference (RFM)*, vol., no., pp.258-262, 9-11 Dec. 2013.
- [30] Evers, A. & Jackson, J.A. 2014, "Analysis of an LTE waveform for radar applications", *IEEE National Radar Conference 2014*, pp. 200-205, 19-23 May 2014, Cincinnati (OH, USA).



- [31] M. Cherniakov, T. Zeng, and E. Plakidis, "Galileo signal-based bistatic system for avalanche prediction", in Proc. IGARSS03, Toulouse, France, July 2003, pp. 784-786.
- [32] M. Cherniakov, R. Saini, R. Zuo, M. Antoniou, "Space-surface bistatic synthetic aperture radar with global navigation satellite system transmitter of opportunity - experimental results", IET Proc. on Radar, Sonar & Navigation, Vol. 1, Issue 6, November 2007, pp. 447-458.
- [33] IEEE Standard for Information technology: "Part 11: Wireless LAN Medium Access Control (MAC) and Physical Layer (PHY) specifications" (IEEE Std 802.11™-1999) – and following Supplements and Amendments (IEEE Stds 802.11a™-1999, 802.11b™-1999, 802.11b™-1999/Cor 1-2001, and 802.11g™-2003).
- [34] F. Colone, K. Woodbridge, H. Guo, D. Mason, and C.J. Baker, "Ambiguity Function Analysis of Wireless LAN Transmissions for Passive Radar", *IEEE Transactions on Aerospace and Electronic Systems*, January 2011, 47, (1), pp. 240-264.
- [35] F. Colone, P. Falcone, C. Bongioanni, and P. Lombardo, "WiFi-Based Passive Bistatic Radar: Data Processing Schemes and Experimental Results", *IEEE Transactions on Aerospace and Electronic Systems*, April 2012, 48, (2), pp. 1061-1079.
- [36] P. Falcone, F. Colone, A. Macera, and P. Lombardo, "2D Location of Moving Targets within Local Areas using WiFi-based Multistatic Passive Radar", *IET Radar Sonar and Navigation*, vol.8, no.2, pp. 123-131, February 2014.
- [37] P. Falcone, F. Colone, and P. Lombardo, "Potentialities and challenges of WiFi-based passive radar", *IEEE Aerospace and Electronic Systems Magazine*, November 2012, 27, (11), pp. 15-26
- [38] F. Colone, D. Pastina, P. Falcone, and P. Lombardo, "WiFi-based passive ISAR for high resolution cross-range profiling of moving targets", *IEEE Transactions on Geoscience and Remote Sensing*, vol. 52, no. 6, pp. 3486-3501, June 2014.
- [39] K. Chetty, G.E. Smith, and K. Woodbridge, "Through-the-Wall Sensing of Personnel Using Passive Bistatic WiFi Radar at Standoff Distances", *IEEE Transactions on Geoscience and Remote Sensing*, April 2012, 50, (4), pp. 1218-1226.
- [40] K. Chetty, G. Smith, H. Guo and K. Woodbridge, "Target Detection in High Clutter Using Passive Bistatic WiFi Radar" , in Proc. of IEEE Radar Conference 2009 , 4-8 May 2009, pp. 1–5.
- [41] P. Falcone, F. Colone, P. Lombardo and T. Bucciarelli, "Range sidelobes reduction filters for WiFi-based passive bistatic radar," *Radar Conference, 2009. EuRAD 2009. European*, Rome, 2009, pp. 133-136.
- [42] F. Colone, P. Falcone, and P. Lombardo, "Passive Bistatic Radar based on mixed DSSS and OFDM WiFi transmissions", in *Proc. 2011 European Radar Conference*, Manchester, U.K., October 2011, pp. 154-157.
- [43] P. Falcone, F. Colone, P. Lombardo, "Doppler Frequency Sidelobes Level Control for WiFi-Based Passive Bistatic Radar", IEEE Radar Conference 2011, 23-27 May, 2011, Kansas City, Missouri (USA).
- [44] F. Colone, D.W. O'Hagan, P. Lombardo, and C.J. Baker, "A Multistage Processing Algorithm for Disturbance Removal and Target Detection in Passive Bistatic Radar", *IEEE Transactions on Aerospace and Electronic Systems*, April 2009, 45, (2), pp. 698-722.

- [45] FP7-PEOPLE-2011-IAPP: SOS - "Sensors system for detection and tracking Of dangerous materials in order to increase the airport Security in the indoor landside area", project funded by the European Union, 7th Framework Program, Marie Curie Action, Grant Agreement No.: 286105, <http://www.sos-project.eu>.
- [46] N. J. Willis, *Bistatic Radar*, Tecnology Service Corporation, 1995.
- [47] V. Cherniak, *Fundamentals of multisite Radar Systems*, Goldon and Breach Science Publishers, 1998.
- [48] M. Cherniakov (ed.), *Bistatic Radar: principles and practice*, Wiley 2007.
- [49] V. Sizov, M. Cheniakov and M. Antoniou, "Forward scattering radar power budget analysis for ground targets," *IET Radar, Sonar and Navigation*, 2007.
- [50] M. Cherniakov, R.S.A.R. Abdullah, P. Jancovic, and V. Chapursky, "Automatic ground target classification using forward scattering radar," in *IEEE Proc. –Radar Sonar Navig.*, 2006.
- [51] Hu Cheng, V. Sizov, M. Antoniou, M. Gashinova, and M. Cherniakov, "Optimal Signal Processing in Ground-Based Forward Scatter Micro Radars," in *IEEE Transactions on Aerospace and Electronic Systems*, vol.48, no.4, pp.3006-3026, October 2012.
- [52] N.F. Abdullah, N.E.A. Rashid, K.A. Othman, and I. Musirin, "Vehicles classification using Z-score and modelling neural network for forward scattering radar," in *International Radar Symposium (IRS) 2014*, June 2014.
- [53] K.H. Mohamed, M. Cherniakov, M.F.A. Rasid, R.S.A. Raja Abdullah, "Automatic target detection using wavelet technique in forward scattering radar," in *European Radar Conference (EuRAD) 2008*, Oct. 2008.
- [54] A.B. Blyakhman, A.V. Myakinkov, and A.G. Ryndyk, "Tracking algorithm for three-dimensional bistatic forward scattering radar with weighting of primary measurements," in *European Radar Conference (EuRAD) 2005*, Oct. 2005.
- [55] A.V. Myakinkov, "Optimal detection of high-velocity targets in forward scattering radar," *5th International Conference on Antenna Theory and Techniques 2005*, May 2005.
- [56] H. Kabakchiev, D. Kabakchieva, M. Cherniakov, M. Gashinova, V. Behar, and I. Garvanov, "Maritime target detection, estimation and classification in Bistatic ultra wideband forward scattering radar," in *International Radar Symposium (IRS) 2011*, Sept. 2011.
- [57] C. Kabakchiev, I. Garvanov, V. Behar, A. Kabakchiev, and D. Kabakchieva, "Forward scatter radar detection and estimation of marine targets," in *International Radar Symposium (IRS) 2012*, May 2012.
- [58] M. Gashinova, L. Daniel, E. Hoare, V. Sizov, K. Kabakchiev, and M. Cherniakov, "Signal characterisation and processing in the forward scatter mode of bistatic passive coherent location systems," *EURASIP Journal on Advances in Signal Processing*, 2013.
- [59] I. Suberviola, I. Mayordomo, and J. Mendizabal, "Experimental Results of Air Target Detection With a GPS Forward-Scattering Radar," in *IEEE Geoscience and Remote Sensing Letters*, 2012, vol.9, no.1, pp.47-51, Jan. 2012.
- [60] P. Krysik, K. Kulpa, and P. Samczynski, "GSM based passive receiver using forward scatter radar geometry," in *International Radar Symposium (IRS) 2013*, June 2013.
- [61] C. Kabakchiev, V. Behar, I. Garvanov, D. Kabakchieva, and H. Rohling, "Detection, parametric imaging and classification of very small marine targets

emerged in heavy sea clutter utilizing GPS-based Forward Scattering Radar," in *IEEE International Conference on Acoustics, Speech and Signal Processing (ICASSP) 2014*, May 2014.

- [62] C. Clemente, and J.J.Soraghan, "GNSS-Based Passive Bistatic Radar for Micro-Doppler Analysis of Helicopter Rotor Blades," in *IEEE Transactions on Aerospace and Electronic Systems*, vol.50, no.1, pp.491-500, January 2014.
- [63] M. Marra, A. De Luca, S. Hristov, L. Daniel, M. Gashinova and M. Cherniakov, "New algorithm for signal detection in passive FSR," 2015 IEEE Radar Conference, Johannesburg, 2015.
- [64] D.R. Wehner, *High-Resolution Radar*, 2nd edition, Boston, MA, USA: Artech House, 1995, Ch. 7, pp.341-364.
- [65] Li Xi, Liu Guosui, Jinlin Ni, "Autofocusing of ISAR images based on entropy minimization", *IEEE Trans. on AES*, vol.35, no.4, pp.1240-1252, Oct 1999.
- [66] C. Zhou, J. D. Sahr, M. G. Meyer, and D. M. Gidner, "Ground clutter subtraction algorithm for VHF passive radar observation of the upper atmosphere," *URSI 2002*, Maastricht, Aug. 2002.
- [67] A. Guner, M.A. Temple, and R.J. Claypoole, Jr., "Direct-path filtering of DAB waveform from PCL receiver target channel," *Electronic Letters*, vol. 39, no. 1, 2003.
- [68] S.R.J. Axelsson, "Improved clutter suppression in random noise radar," *URSI 2005 Commission F Symposium on Microwave Remote Sensing of the Earth, Oceans, Ice, and Atmosphere*, April 2005.
- [69] K. Kulpa and Z. Czekala, "Masking effect and its removal in PCL radar," *IEE Proc. on Radar, Sonar and Navigation*, vol. 152, no. 3, June 2005.
- [70] D.W. O'Hagan, C.J. Baker, and H.D. Griffiths, "Signal and Interference Analysis: Proposed Analogue Signal Suppression Techniques for PCL Radar," *3rd European Radar Conference, EuRAD 2006*, Sept. 2006.
- [71] Wan Hong, Li Shentang, and Wang Zhigang, "Direct Path Interference Cancellation in FM Radio-Based Passive Radar," *8th Int. Conf. on Signal Processing*, vol.1, 2006.
- [72] J.E. Palmer and S.J. Searle, "Evaluation of adaptive filter algorithms for clutter cancellation in Passive Bistatic Radar," *IEEE Radar Conference 2012*, Atlanta, May 2012.
- [73] Z. Zhao, X. Wan, Q. Shao, Z. Gong, and F. Cheng, "Multipath clutter rejection for digital radio mondiale-based HF passive bistatic radar with OFDM waveform," *IET Radar, Sonar & Navigation*, vol. 6, no. 9, Dec. 2012.
- [74] M. John, M. Inggs, and D. Petri, "Real time processing of networked passive coherent location radar system," *International Journal of Electronics and Telecommunications*, vol. 57, no. 3, 2011.
- [75] M.R. Inggs and C.A. Tong, "Commensal radar using separated reference and surveillance channel configuration", *Electronics Letters*, vol. 48, no. 18, 2012.
- [76] H.-W. Li and J. Wang, "Particle filter for manoeuvring target tracking via passive radar measurements with glint noise," *IET Radar, Sonar and Navigation*, vol. 6, no. 3, 2012.
- [77] D.K.P. Tan, M. Lesturgie, H. Sun, and Y. Lu, "Space-time interference analysis and suppression for airborne passive radar using transmissions of opportunity," *IET Radar, Sonar & Navigation*, vol. 8, no. 2, Feb. 2014.

- [78] H. Kuschel, M. Ummenhofer, P. Lombardo, F. Colone, and C. Bongioanni, "Passive radar components of ARGUS 3D," *IEEE Aerospace and Electronic Systems Magazine*, vol. 29, no. 3, March 2014.
- [79] T. Jenho and B.D. Steiberg, "Reduction of sidelobe and speckle artifacts in microwave imaging: the CLEAN technique", *IEEE Transactions on Antennas and Propagation*, Vol. 36, Issue 4, 1988, pp.543-556.
- [80] K. S. Kulpa and Z. Czekala, "Masking effect and its removal in PBR radar," *Proc. Inst. Elect. Eng.—Radar, Sonar Navig.*, vol. 152, no. 3, pp. 174–178, Jun. 2005.
- [81] A. Macera, C. Bongioanni, F. Colone, and P. Lombardo, "Receiver architecture for multi-standard based Passive Bistatic Radar," in *Proc. 2013 IEEE Radar Conference*, Ottawa, Ontario, Canada, 29 April-3 May 2013.
- [82] <http://www.metasensing.com/wp/index.php/products/fastgbsar>.
- [83] <http://www.floridaairportshomes.com>.
- [84] <http://www.aviogestioni.it>.
- [85] T. Rappaport, *Wireless communications: principles and practice*, Prentice-Hall PTR, 1996.
- [86] J. D. Parsons, *The mobile radio propagation channel*, John Wiley & Sons, 2000, 2<sup>nd</sup> edn.